Experimental and Numerical Studies of Laminar Counter-flow Diffusion Flames Using Biomass-based Gaseous Fuels

vorgelegt von

Dipl.-Ing.
Marie-Theres Scharl

an der Fakultät III - Prozesswissenschaften
der Technischen Universität Berlin
zur Erlangung des akademischen Grades

Doktorin der Ingenieurswissenschaften
– Dr.-Ing. –

genehmigte Dissertation

Promotionsausschuss:

Vorsitzender: Prof. Dr.-Ing. Dietmar Auhl
Gutachter: Prof. Dr. rer. nat. Frank Behrendt
Gutachter: Prof. Dr. rer. nat. Volker Sick

Tag der wissenschaftlichen Aussprache: 26. August 2021

Berlin 2022

Ich erkläre hiermit, dass ich die vorliegende Arbeit selbständig verfasst und keine anderen als die angegebenen Quellen und Hilfsmittel verwendet habe.

Berlin, den 26. Dezember 2021

Acknowledgements

My gratitude and thankfulness go out to many people regarding the completion of this thesis.

I wish to thank my supervisors and mentors, Prof. Dr. Frank Behrendt, Prof. Dr. Douglas Greenhalgh, and Prof. Dr. Alba Dieguez Alonso, for their support and challenges in the years at EVUR. Furthermore, a big thank you is directed at Prof. Dr. Volker Sick for reviewing this work and Prof. Dr. Dietmar Auhl for taking the time to serve as the chairman of the dissertation committee.

My work would not have been possible without the heart and soul of the EVUR chair Uwe Röhr, Susanne Hoffmann, and Ines Preschel; a warm thank you also goes to Birgit Packeiser and Michaela Riese.

Omid Elhami, Thomas Mouton, Jenny Rieck, Lina Taube, Hernán Almuiña Villar, Maximilian Mehnert, and many other colleagues of EVUR have enriched the time of my thesis with support, laughter, discussions, and memories for a lifetime, which I will never forget.

Carsten Waechtler, Fabian Schmid, Arndt Kobusinski, Robin Reinking, Oliver Löschke, Mohamad Hussein, and Madeleine Lange, you were all somehow „my students“ during the summer schools, household tasks, and my thesis - thank you for being part of this journey.

The support at Technische Universität Berlin goes beyond our faculty III when help is needed. A big thanks goes to many colleagues and friends from all the years at TUB, you know who you are.

Finally, I would like to thank my friends and, foremost, my family for the endless love, encouragement, and support.

Mama, Papa, Curt, Max, Ferdi, Mone, Leo, Linchen - this thesis is dedicated to you.

Ivo Schneider, you will never be forgotten.

Abstract

Thermochemical conversion processes are regarded as promising alternatives for decentralized energetic utilization of biomass. Pyrolysis and gasification of (woody) biomasses present a possibility to produce a fuel gas to be used, among other applications, in internal combustion engines or turbines as part of combined heat and power generation (CHP).

This thesis aims to gain a deeper understanding of the utilization of biomass-based gaseous model fuels in combustion systems. This is investigated in the present thesis, combining both experimental studies and numerical simulations of laminar non-premixed flames in a counter-flow burner set-up.

To this end, a counter-flow burner system was designed and built as the central part of a spectroscopic measuring system to validate an in-house time-dependent implicit Fortran code for diffusion flames named DIFFLA. This was foremost achieved by spectroscopic laser-induced fluorescence measurements of formaldehyde and Rayleigh scattering experiments, deducing temperature fields in flames. Furthermore, CH* chemiluminescence experiments were performed. These diagnostic tools were all utilized to analyze flame behavior and flame structure by providing an accurate understanding via temperature distributions, the tracking of intermediate species, and by localizing the flame front.

This study focuses on synthetic gas mixtures consisting of multiple components, resembling, to different extents, typical compositions of the product gas obtained in biomass gasification or pyrolysis processes. Diluted methane as reference fuels and further fuels composed of N_2, H_2, CO, CO_2, and CH_4 were investigated, partially adding O_2 to fuel or oxidizer. In all cases, the oxidizer was air, and a wide range of air-fuel ratios was considered. Furthermore, the presented system comprised a range of flames combusting at strain rates starting at around $60\,s^{-1}$ leading up to circa $250\,s^{-1}$. Therefore, incorporating the boundary condition at very low fuel- and oxidizer velocities for combustion, though not including the other limiting condition, at strain out.

The influence of the product gas composition on the flame behavior and flame structure, with respect to the changes of the species profiles and peak temperatures with changing flow velocities, was investigated. All in all, illuminating the combustion mechanisms of these hydrocarbon mixtures from multiple perspectives and providing valuable information about the operations with different synthetic biomass-based gaseous model fuels.

Zusammenfassung

Thermochemische Konversionsverfahren werden als vielversprechende Alternativen zur dezentralen energetischen Nutzung von Biomasse gehandelt. Pyrolyse und Vergasung von (holzigen) Biomassen stellen Möglichkeiten dar ein Brenngas zu erzeugen, das, unter anderem, in Verbrennungsmotoren oder Turbinen im Rahmen der Kraft-Wärme-Kopplung (KWK) eingesetzt werden kann.

Ziel dieser Arbeit ist es, ein tieferes Verständnis für die Verbrennung von gasförmigen Brennstoffen, die aus thermochemischen Konversionsverfahren gewonnen wurden, zu erlangen. Dies wird durch die Gegenüberstellung von experimentellen Untersuchungen zu numerischen Simulationen verschiedener laminarer, nicht vorgemischter Flammen in einem Gegenstrombrenner erreicht.

Zu diesem Zweck wurde ein Gegenstrombrennersystem als zentraler Teil eines spektroskopischen Messsystems entworfen und gebaut, um den hauseigenen zeitabhängigen und impliziten Fortran-Code für Diffusionsflammen namens DIFFLA zu validieren. Dies geschah in erster Linie durch spektroskopische laserinduzierte Fluoreszenzmessungen von Formaldehyd und durch Rayleigh Streuungsexperimente, die auf Temperaturfelder in den Flammen schließen lassen. Des Weiteren wurden Messungen von CH*-Chemilumineszenz durchgeführt. Diese Diagnosewerkzeuge wurden alle genutzt, um das Flammenverhalten und die Flammenstruktur zu analysieren, indem sie einen genauen Zusammenhang über Temperaturverteilungen, die Verläufe der Zwischenspezies und die Lokalisierung der Flammenfront herstellen.

Diese Studie befasst sich mit synthetischen Gasgemischen, welche, in unterschiedlichem Maße, den typischen Zusammensetzungen der Produktgase ähneln, die bei Vergasungs- oder Pyrolyseprozessen von Biomasse entstehen. Untersucht wurde verdünntes Methan als Referenz und Brennstoffe, welche zusammengesetzt waren aus N_2, H_2, CO, CO_2 und CH_4. Zusätzlich wurde dem Brennstoff oder Oxidator teilweise O_2 zugegeben. In allen Fällen war der Oxidator Luft und es wurde ein breiter Bereich von Luft-Kraftstoff-Verhältnissen berücksichtigt. In dieser Studie wurden Flammen die bei der Dehnungsgeschwindigkeiten von ca. $60\,s^{-1}$ bis hin zu ca. $250\,s^{-1}$ verbrannten in Betracht gezogen. Damit ist die Randbedingung sehr niedriger Brennstoff- und Oxidationsströmungsgeschwindigkeiten beachtet worden, weniger die mögliche andere Randbedingung des sogenannten „strain-out“.

Untersucht wurde der Einfluss der Produktgaszusammensetzung auf das Flammenverhalten und die Flammenstruktur im Hinblick auf die Änderungen der Speziesprofile und Spitzentemperaturen bei wechselnden Strömungsgeschwindigkeiten.
Insgesamt werden die Verbrennungsmechanismen dieser Kohlenwasserstoffgemische

aus mehreren Blickwinkeln beleuchtet und liefern somit wertvolle Informationen für die Nutzung verschiedener gasförmiger Brennstoffe auf Basis von holziger Biomasse.

Contents

List of Figures

List of Tables

Abbreviations

ADC	analog-to-digital converter
BDG	biomass-derived gases
CCD	charge-coupled device
CHP	combined heat and power
Da	Damköhler number
DME	dimethyl ether
FHG	fourth-harmonic generation
ICCD	intensified charge-coupled device
L/D	ratio of nozzle separation distance to nozzle diameter
Le	Lewis number
LFA	laminar flamelet assumption
LES	large eddy simulations
LHV	lower heating value
LIF	laser-induced fluorescence
PLIF	planar laser-induced fluorescence
Ka	Karlovitz number
MC	mixing chamber
MFC	mass flow controller
MCP	microchannel plate
NO_x	nitrogen oxides
PAH	polycyclic aromatic hydrocarbons
PIV	particle image velocimetry
PCI	peripheral component interconnect
Pr	Prandtl number
PTU	programmable timing unit
RANS	Reynolds-averaged Navier-Stokes equations
Re	Reynolds number
RME	rape methyl ester
Sc	Schmidt number
SHG	second-harmonic generation
STP	standard temperature and pressure
THG	third-harmonic generation

Symbols

Roman letters

Sign	Description
A	Surface area
a	Strain rate
A_{21}	Einstein coefficient
A_f	Conical surface area
$a(\lambda)$	Mean molecular volume polarizability
A_N	Avogadro constant
A_r	Collision factor
A_t	Cross-sectional area of a tube
b_r	Temperature exponent
f	Mass flux through a wave
C	Reaction progress variable
c_p	Specific heat capacity
d	Diameter
${D_i}^m$	Modified binary diffusion coefficient
${D_i}^T$	Thermodiffusion
$D_{i,j}$	Mixture-averaged diffusion coefficient
D_{mdc}	Mean diffusion coefficient
E	Energy of a photon
e_i'	represents the vibrational levels
E_a^r	Activation energy
$E_{electronic}$	Electronic energy of a photon
$E_{rotational}$	Rotational energy of a photon
$E_{vibrational}$	Vibrational energy of a photon
f_1, f_2	Focal lengths
$F_k(\lambda)$	King correction factor
G	Function representing a scalar field
G_0	Flame front position in G
$G_{r,f}^0$	Free enthalpy
$h = H_F$	Flame height
h_P	Planck's constant
$h_i(T)$	Absolute enthalpies
h_u, h_b	Enthalpy upstream and downstream of a wave
I	Incident laser intensity
j_i	Diffusive mass flux

Roman letters

Sign	Description
K	Flame stretch
K_{em}	Constant for the detector efficiency and the solid collection angle
k_i	Thermal diffusion ratio
K_q	Stern-Volmer quenching constant
k_r	Reaction rate coefficients
K_r^c	Equilibrium constant
k_x	Rate constants
L	Burner separation distance
$l_{distance}$	Distance between lenses
l_k	Kolmogorov turbulent length scale
l_t	Turbulent length scale
M_i	Molar mass
M_j	Mean molar mass of the mixture
n	Amount of substance
N	Number density
$N*$	Number density of excited species
$n(\lambda)$	Refractive index
p, p_u, p_b	Pressure
Q	Quencher
R	Universal gas constant
r	Radius
r_d	Mass scale chemical rate of formation
r_i	Specific rate of formation
R_L	Molar refractivity
S	Total Rayleigh scattering signal
S_0	Ground state
S_1, S_2	Electronic states
S_{em}	Chemiluminescence signal
$s_i(T)$	Absolute entropies
S_L	Propagation speed
T, T_u, T_b	Temperature
T_1	Excited triplet state
u	Velocity
u'	Turbulent intensity
u_k	Kolmogorov turbulent intensity
u_u, u_b	Velocity upstream and downstream of a combustion wave
V	Volume
V_e	Axial velocity
V_{em}	Volume of a pixel
V_f	Velocity of fuel
V_o	Velocity of oxidizer
V_R	Observation volume
$v'_{r,i}$, $v''_{r,i}$	Stoichiometric coefficients
V_t	Average flow velocity of a tube
x_f	Flame front location in G
y_u, y_b	Fuel concentration in an unburned and burned region
Z	Mixture fraction
$Z_{stagnation}$	Distance of the stagnation plane to the bottom nozzle

Greek letters

Sign	Description	Unit
δ_l	Thickness	
α_h	Thermal diffusivity	
χ_{air}	Air mole fraction	
χ_{fuel}	Fuel mole fraction	
δ_D	Preheat zone	
δ_R	Finite reaction zone	
$\Delta\Omega$	Solid angle of the collection optics	
$(\delta\sigma/\delta\sigma)_{mix}$	Differential scattering cross section	
η	Optical collection efficiency	
$\gamma(\lambda)$	Mean molecular volume anisotropy	
λ	Wavelength	
λ_b	Heat conductivity	
λ_{er}	Fuel equivalence ratio	
λ_{tc}	Thermal conductivity	
μ	Dynamic viscosity	
ν	Kinematic viscosity	
ν_i	Absorption frequency	
ν_{mf}	Number of moles for a complete reaction	
Φ_{er}	Air equivalence ratio	
Φ_f	Fluorescence quantum yield	
Ψ	Reactive scalars	
ρ	Density	
$\rho_0(\lambda)$	Depolarization ratio	
ρ_b	Mass density of a fluid downstream of a combustion wave	
ρ_f	Density of fuel	
$\rho_h(\lambda)$	Horizontally polarized light	
ρ_o	Density of oxidizer	
ρ_u	Mass density of a fluid upstream of a combustion wave	
$\rho_v(\lambda)$	Vertically polarized light	
τ	Detectors exposure time	
τ_c	Chemical reaction time-scale	
τ_f	Flow time-scale	
τ_k	Kolmogorov time-scale	
τ_t	Turbulent flow time-scale	
σ	Total Rayleigh cross section	

Chapter 1

Introduction

One of the greatest challenges of our time is global warming and the ongoing climate change. The use of limited fossil fuels needs to be re-thought, and the utilization of renewable and sustainable energy systems finally needs to gain further importance.

In 2014, the leaders of the European Union agreed to achieve a reduction of greenhouse gas emissions by more than 40 % by 2030, in comparison to the level in the year 1990. At the beginning of 2015, an energy union strategy for the European Union was published by the Juncker commission, basing the provisioning on secure, sustainable, competitive, and affordable measures. These should be established with the help of a plan split into five dimensions: ensuring energy security, improving energy efficiency, supporting research and innovation in clean technologies, integrating an internal energy market, and decreasing the use of fossil fuels [35].

The energy system needs to be revolutionized holistically, not only focusing on the electricity sector but also concentrating on other sectors such as agriculture, transportation, industrial applications, and heating and cooling. From this point forward, the main targets should be based on sector coupling, and furthermore, a carbon reduction plan for all situations and phases of our society.

Efforts are in progress to overcome the disadvantages of the utilization of renewable energy sources. Such may be, i.e., the specialization of countries in assorted technologies. These can be chosen based on local and geographical circumstances, therefore touching economic and environmental areas of expertise. Also, overcoming cost detriments in comparison to traditional fuels like nuclear power, coal, lignite, and/or gas, which have to be carried by the European Union and by its member states [36]. Furthermore, spatial and temporal availability issues need to be overcome, also having an influence on provisioning energy exclusively on the basis of renewable sources by combining more than one source [4].

Biomass as a key renewable energy resource could be recognized as the answer to many concerns and dependencies previously presented. To act as a source for any of the possible conversion processes, some requirements need to be met regarding up-scaling: an increased conversion efficiency, a dependable and stable source of feedstock production, and a profitable but also sustained agricultural land management [4].

Furthermore, for the ever-increasing request for energy, combustion has been and will remain a simple key technology to utilize. The world's energy demand has been met by 90 % by the combustion of fossil and biofuels. Though this increasing demand has been escalating the three major problems of: decreasing fossil fuel resources, steady global warming, and increased air pollution [37]. To govern these major problems, combustion technologies need to be substantially advanced.

Technical and industrial combustion applications, such as engines and gas turbines, are dominated by turbulent, rather than laminar, combustion processes. Heat releases and mixing processes accelerate flow instabilities and, therefore, turbulent flow fields [38]. To advance a gain in knowledge in this field, initially, numerical modelling of turbulent combustion is necessary. Multiple approaches are used to numerically simulate such processes, such as laminar flamelet models. Here laminar, one-dimensional, and time-dependent thin layers, namely flamelets, are covering and can present a turbulent combustion regime [39]. Finally, these models need to be validated by experimental solutions.

The needs for biomass as a renewable energy source and further improvements in combustion technologies motivated this investigation of synthetic model fuels with biomass-based compositions. Since combustion can be more efficient with syngas from biomass gasification or pyrolysis processes, rather than combusting the feedstock directly. This is based on higher temperatures or the possibility of utilizing other technical applications [40].

This work focuses on the experimental validation of a laminar model simulating one-dimensional counter-flow diffusion flames named DIFFLA using multiple biomass-based synthetic fuels and, furthermore, the flames behavior during combustion, with and without oxygen enhancement. Chapter 2 will present an overview of biomass as a source of energy and the conversion processes leading to the investigated fuels. This is followed by an outline of the varying combustion techniques of gaseous fuels in Chapter 3. Chapter 4 presents the applied experimental spectroscopic techniques Rayleigh scattering, laser-induced fluorescence of formaldehyde,

and CH* chemiluminescence used for validating the model DIFFLA, which is furthermore introduced in Chapter 6. To preliminarily verify the in-house designed and built counter-flow burner set-up described in Chapter 5, diluted methane combustion was conducted experimentally and confirmed numerically. The results and conclusions are presented extensively in Chapters 7 and 8.

Chapter 2

Biomass as a source of energy

One of the major appeals of biomass as a source of energy or green chemicals is the wide availability and its possibility to be quickly renewed. In contrast to fossil fuels, biomass is formed from living species that are alive now or were briefly ago, and it does not take several million years to be replenished. Atmospheric CO_2 is metabolized by plants via sunlight using photosynthesis, instigating their growth [28, 29]. Commonly only about 1 % of the sunlight is used by photosynthesis. The origin of the biomass can be treated as organic material that accumulates solar energy in the form of chemical bonds. When these bonds are broken, for example, by thermochemical conversion processes, the materials release their chemical energy. As part of this process, the deduced carbon material is oxidized to again produce CO_2 and water. Therefore it is regarded as a cycle when being available to create new biomass [41].

In the sense of conversion, a wide range of biomass, like small grasses to immense trees, can be useful and generally be classified in lignocellulosic material [42], sugar, starch [28], oilseeds [41], and agricultural, forest, municipal or industrial waste [1]. Biofuels can also be further subclassified in first- (1G) and second-generation (2G) biofuels. Grains, sugar cane, vegetable oils, i.e., are either food crops themselves or mainly produced from food crops. 1G biofuels can therefore be linked to increasing food prices. This promoted the development of 2G fuels from non-food biomass, residues from agriculture or forestry, or co-products from production processes to confine the „food vs. fuel“ conflicts [43, 44].

Lignocellulosic biomass is dominantly composed of the aromatic polymer lignin and the carbohydrate polymers cellulose and hemicellulose, which basically constitute the cell walls in biomass. Humans can not digest lignocellulose; hence it is not part of the human food chain and not ominous for food supplying processes [28, 42].

The structure of lignin is a highly complex phenylpropenyl formation, which is randomly branched and transforms based on the biomass's origin. The phenypropenyl macromolecule is, amongst others, made of syringols and guaiacols and joined by carbon-oxygen or carbon-carbon bonds [42]. Cellulose is a crystalline structured long-chain polymer made up of many glucose molecules. It can be represented by the generic formula $(C_6H_{10}O_5)_n$ and is highly polymerized, with a massive molecular weight [28]. Hemicellulose is, unlike cellulose, of a weak, random, and amorphous structure, which is not resistant to hydrolysis and can be presented by the generic formula $(C_5H_8O_4)_n$ [29]. It is made of a big group of carbohydrates, a typical hemicellulose molecule being xylan, and is of a lower degree of polymerization. Furthermore, lignocellulosic biomass includes extractives and small amounts of inorganic components such as iron, calcium, phosphorus, and/or sodium [28].

For lignocellulosic biomass, some pretreatment can be necessary due to the enclosing of the lignin and hemicellulose around the cellulose. Pretreatment techniques therefore not only liberate the cellulose from other surrounding components of biomass but also lower the cellulosic crystallinity [42]. The output depends on a criterion named the „severity factor“, which is the joined effect of the duration, temperature, and acidity of the process [45]. Torrefaction can be used as a pretreatment for thermochemical conversion processes by improving multiple properties of the lignocellulosic biomass [46]. Pretreatment techniques should be utilized on low operational and capital costs, preparations of the biomass before the pretreatment should be kept to a minimum, and lastly, it should run on a low energy demand, or it shall be possible for the energy to be reused, i.e., for secondary heating [45].

Biomass-based fuels, as presented in 3.4.2, based on thermochemical conversion processes such as gasification and pyrolysis, represent carbon-neutral alternative fuels for combustion processes. In comparison to fossil fuels, their energy density is lower; therefore, their combustion behavior has to be investigated thoroughly to exploit their full potential. Furthermore, due to the difference in energy efficiency, typical applications for fossil fuels would have to be modified geometrically, or co-firing would have to be applied. Finally, a systematic overview of biomass-derived gases (BDG) has not been achieved yet, due to the extreme diversity of compositions due to numerous dependencies on process and application parameters [47].

2.1 Conversion processes of biomass

The conversion of biomass to energy incorporates various decisions, mainly which type of energy is required for which purpose and also what type of biomass will be utilized. Which conversion pathway will be pursued, what kind of infrastructure is available or needed, and lastly, what application will be prosecuted [3].

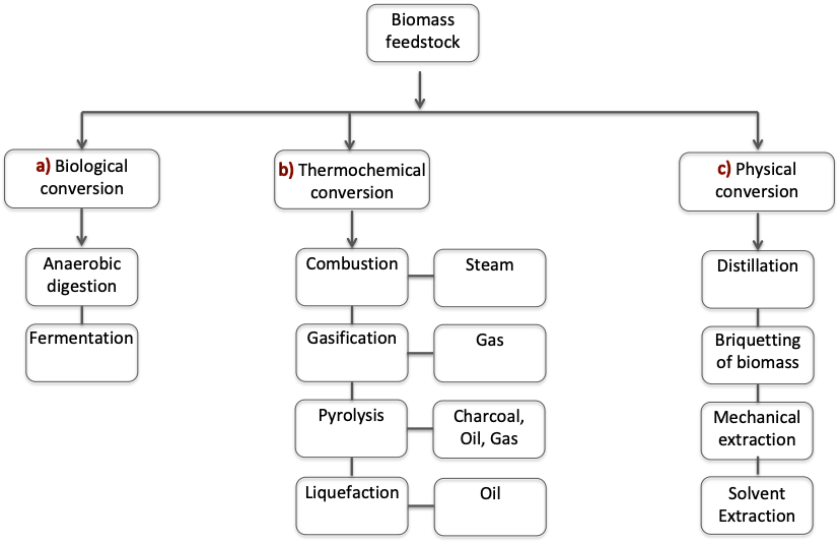

Figure 2.1: *Schematic illustration of the conversion routes of biomass based on [1–4]*

The different conversion paths for a.) biological, b.) thermochemical, and c.) physical conversion processes are represented in Figure 2.1. The routes a.), and c.) will be presented briefly, as the focus of this study was on product gas of the thermochemical conversion processes gasification and pyrolysis.

Biological processes can be subdivided into the methods of anaerobic digestion by bacteria or fermentation with the use of enzymatic conversion. Anaerobic digestion can be applied to convert organic material by bacteria into biogas, which consists mainly of methane and carbon dioxide (and other gases in small fractions like hydrogen sulphide). This biogas can be utilized directly in gas turbines and gas engines and can furthermore be upgraded by removing carbon dioxide. Ethanol can be produced from sugar and starch crops via fermentation [3]. The use of enzymes is resorted to when converting macromolecular starch. This type of starch can not be fermented by conventional technologies; therefore, it is ground up, mixed with water, heated, and treated with enzyme preparations to produce ethanol or amino acid [1].

Physical conversion techniques include distillation, briquetting of biomass, and mechanical or solvent extraction. To extract essential oils, the method of distillation

is frequently used. Biomass is steam distilled, the oils are vaporized, and the more volatile fractions of a composition can be separated from the non-volatiles [1]. Especially biomass waste as agricultural or forest residues are frequently tricky to handle due to their uneven and burdensome characteristics. By briquetting or pelletisation, this waste can be formed into a densified and homogeneous product for reuse [48, 49]. Extraction as a mechanical conversion process yields oil from seeds of various biomass crops, to be processed in further steps to obtain bio-diesel or rape methyl ester (RME). A residual solid or „cake“ emerges herewith as a byproduct that can be disposed as animal food. Finally, primary and secondary metabolites can be extracted from biomass using solvents [1, 3].

Finally, the thermochemical conversion processes pyrolysis, gasification, combustion, and liquefaction of biomass, especially lignocellulosic materials, will be presented. These are key technologies for the production of industrial or domestic heat and electricity or the production of fuel for a combined heat and power (CHP) cogeneration [50]. As biomass is heated at varying temperatures and under sufficient or insufficient oxygen conditions, thermal degradation and chemical reformation lead to gaseous, liquid, and/or solid outputs. Compared to other conversion techniques, the advantage of thermochemical processing is the possibility of transforming all the organic components of the biomass [1].

Pyrolysis is the thermochemical decomposition of biomass in the absence of externally provided oxygen, leading to liquid bio-oils, gases, and solid products like charcoal. The produced char can be utilized as „green coal“, while the bio-oil can either be upgraded to be possibly used as renewable diesel or jet fuel or applied directly in power plants, furnaces, or boilers [51,52]. Lastly, a noncondensable primary gas mixture made of carbon dioxide, carbon monoxide, water, methane, ethane, ethylene, and other components is produced [28]. During gasification, biomass is converted into a combustible gas mixture, typically by partial or complete oxidation, depending on the gasifying agent. The biomass feedstock is heated in a medium like air, oxygen, or steam, commonly with an insufficient supply of oxygen. The produced fuel can either be burned directly in gas engines or gas turbines or used as syngas for the manufacturing of chemicals or liquid fuels [31,51]. Combustion or burning is the direct exothermic chemical reaction between a fuel and an oxidizer, commonly air, releasing carbon dioxide and water and leading to heat and therefore, i.e., mechanical energy or electricity. Stoves, furnaces, boilers are based on this process [3].

Finally, during the thermochemical process liquefaction, a liquid is obtained using low temperatures, high pressure, and a catalyst, also commonly with hydrogen present [51].

2.1.1 Pyrolysis

Pyrolysis is the thermochemical degradation of materials in the absence of oxygen up to around 500 °C, which not only results in the production of gases but also solid (charcoal) and liquid (bio-oil water) outputs [3]. The general chemical equation is shown as follows [28]:

$$(\mathrm{C}_n\mathrm{H}_m\mathrm{O}_p) + \mathrm{Heat} \longrightarrow \sum{}_{\mathrm{liquid}}\, \mathrm{C}_a\mathrm{H}_b\mathrm{O}_c + \sum{}_{\mathrm{gas}}\, \mathrm{C}_x\mathrm{H}_y\mathrm{O}_z + \sum{}_{\mathrm{solid}}\, \mathrm{C} \tag{2.1}$$

This is the fundamental chemical process, making it the precursor both of the gasification and the combustion processes. The products depend on the feedstock, the heating rate, and the final temperature of the procedure. Furthermore, as the typical lignocellulosic feedstocks are poor heat conductors, the size of the particles needs to be on a small-scale [42].

The reaction kinetics during pyrolysis of cellulose have been studied intensely, and abundant mechanisms have been proposed. The model of Broid-Shafizadeh, as displayed in Figure 2.2, is broadly known.

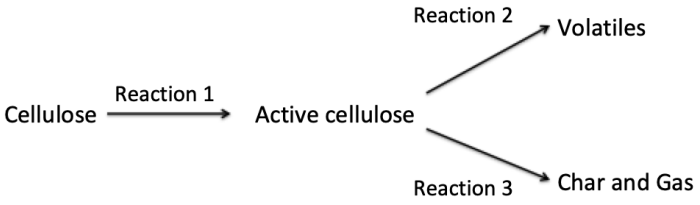

Figure 2.2: *Model for cellulosic pyrolysis mechanism by Broid-Shafizadeh based on [5]*

Based on this model, the mechanism includes three steps: first, activation of the cellulose, second, the transformation of this active cellulose into volatiles, and third the conversion of this active cellulose into char and gas. The thermal degradation of cellulose starts at 52 °C; at these low temperatures, the degree of polymerization starts to decrease, and charring occurs. At higher temperatures, volatilization takes place rapidly [53]. The determination of a mechanism for hemicellulose is complex due to the varying and inconstant branched structures in the material when comparing woody biomass amongst each other. The most abundant polysaccharide is

xylan, this is also the part of the hemicellulose that is the least thermally stable. The degradation process starts at 200 °C-260 °C. Lignins are also highly branched and complex in the form of mononuclear aromatic polymers, often bound to bordering cellulose fibers. The pyrolysis of lignin has been investigated intensively, leading to the assumption that the primary pyrolysis products are guaiacol and pyrogallol dimethyl ether. The degradation reaction of lignin has maxima between 225 °C-450 °C, depending on the gasifying agent [5]. The overall pyrolysis reactions for woody lignocellulose are arranged schematically in Figure 2.3 [6].

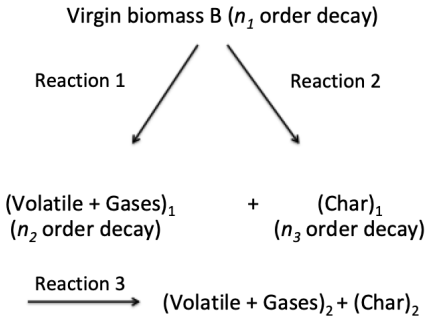

Figure 2.3: *Model for lignocellulosic biomass pyrolysis, commonly known from [6], based on [5]*

This model insinuates that lignocellulosic biomass degrades in a competitive reaction mechanism to volatiles, gases, and char in a primary pyrolysis. Furthermore, the produced volatiles and gases react again with char to modified kinds of volatiles, gases, and char in secondary interactions. [5]. Based on the heating rate, overall temperature, feedstock residence time, and particle size of the solid feedstock, the pyrolysis process is classically subdivided into slow pyrolysis, fast pyrolysis, and flash pyrolysis [5, 53].

The slowest type of pyrolysis process is carbonization. The biomass is heated slowly, even for days, at very low heating rates, up to a temperature of 400 °C, with charcoal production as a primary goal. The typical slow pyrolysis has a medium heating rate, a residence time of minutes to hours, as opposed to days, and produces all types of pyrolysis products previously mentioned at a maximum temperature of 600 °C [28]. The vapor residence time is considerably longer during slow pyrolysis, as in any other form of this thermochemical conversion, hence giving the vapor additional time to react while the char and oils are being formed. Otherwise, vapors can also be removed constantly while being produced [54]. From a thermal perspective, the process of pyrolysis can be separated in the stages listed in Table 2.1, lacking sharp boundaries.

By increasing heating rates, the yield of char decreases. In turn, a higher output of liquid products can be achieved via the form of conversion named fast pyrolysis [51]. Bio-oils are formed by rapidly depolymerizing and fragmenting cellulose, hemicellulose, and lignin, and finally quenching intermediate products that would react further, with longer residence times, during high temperatures [54].

Table 2.1: *Thermal stages of the pyrolysis process based on [5, 28–30]*

Temperature	**Processes**	**Products**
Drying (~100 °C)	Free moisture and mildly bound water evaporates, while this heat is absorbed into the biomass. Melting of lignic fraction at high humidty.	-
Initial stage (~100 °C-~300 °C)	Exothermic dehydration of the feedstock, hence water elimination. Depolymerization and free radical formation.	Carbonyls, carboxyls, CO, CO_2, charred residue.
Intermediate stage (>~200 °C)	Primary pyrolysis takes place from ~200 °C-~600 °C, producing most of the bio-oil.	Primary char, condensable gases, noncondensable gases.
Intermediate stage (~300 °C-~450 °C)	Breaking of glycosidic bonds and linkages of polysaccharides. The secondary cracking of volatiles into noncondesables and char, and therefore the final stage begins. Hydrocarbon evolution. Exothermic peaks from lignin decomposition appear at around ~280 °C-~390 and ~420 °C.	Tar in form of levoglucosan, anhydrides, and oligosaccharides (important parts of bio-oil).
Final stage (>~450 °C)	Dehydration, displacement, and decomposition of sugar units.	Forming of carbonyl products such as glyoxal, acrolein, and acetaldehyde.
Final stage (>~600 °C)	A higher production of H_2 is favored, with a further increase of the yield above ~900 °C.	H_2 and a mixture of all the previously mentioned compounds.

The produced bio-oil is a homogeneous liquid, exhibiting half the heating value of conventional fuel oil. To obtain this output, the biomass feedstock should be $< 3\,\text{mm}$, have vapor residence times of $< 2\,\text{s}$, at best $< 10\,\%$ moisture in the biomass feed and sustain rapid cooling of the vapors. Furthermore, the ash content of the biomass and the char separation influence the catalytic effect on the vapor cracking and hence the liquid yields [52].

Bio-oils need to be upgraded before most applications due to their low pH (leading to corrosion), high viscosity (predicament to transport in pipes), alkali metals content (damage or sedimentation), thermal instability (decomposition), and so forth. This enhancement can be achieved by filtration, hydrogenation, or catalytic cracking of the liquid product [7].

One of the biggest challenges during fast pyrolysis is the heat transfer to the vessel. A considerable amount of thermal input is needed to heat the biomass feedstock to a reaction temperature in this endothermic process. Possible solutions represent multiple heat transfer surfaces, heating the fluidization gas, or heating the bed material (if included) [52].

During flash pyrolysis, the feedstock is heated to a moderate temperature of 450 °C-650 °C, but in an extremely short period of time of 30-1500 ms. During this process, the liquid yield can be increased even further than during fast pyrolysis, up to 70-75 %, due to rapid quenching. High heating rates favor gaseous products at the expense of bio-oil due to gas-phase cracking reactions [28, 55]. Flash pyrolysis can be achieved when involving a heat carrier solid. This ensures a high heat transfer while the solid undergoes a rapidly fast mixing process with the biomass feedstock. The peak liquid yields are reached at around 650 °C, and gaseous products can be maximized close to 1000 °C [28].

Pyrolysis processes can occur in reactor types that will be presented thoroughly in Section 2.1.2. The principal designs that are utilized are: fixed- or moving-bed, bubbling fluidized-bed, circulating fluidized-bed (will be presented in the following section), entrained flow, rotating cone, ultra-rapid, ablative, and vacuum reactors [28, 56]. The rotating-cone reactor works as a transport-bed reactor, with the movement realized by centrifugal forces [52]. In an ultra-rapid pyrolyzer, both the inerting agent and heat-carrier solids are heated externally and blasted on a biomass feedstock stream. Such forces result in a heating rate of a few milliseconds. The ablative technique is substantially different compared to the other pyrolysis processes presented. A decrease in heat transfer limitation is established by pressing biomass against the reactor's wall at high pressure mechanically or via centrifugal forces. The liquid rather melts out of the biomass, while the liquid film that develops on the walls vaporates. Reaction rates are not limited by the heating rates any longer; larger sizes of feedstock can be utilized [28, 52]. Lastly, vacuum pyrolysis with numerous stacked and heated circular plates at different temperatures, where the biomass falls through with the help of knife scrapers, can be employed [28].

2.1.2 Gasification

During the process of gasification, biomass is converted to gases, vapors, and char/ash, achieving high yields of combustible gases like hydrogen, carbon monoxide and methane [56], and diluents like nitrogen and carbon dioxide, with the final composition depending on the process conditions. Furthermore, tars and char are byproducts of this process. To enhance the production of gaseous products, [57] gasification is carried out at temperatures >800 °C [31], typically at partial oxidation or partial combustion. [57] Coal gasification was used since the early 1800s for illumination reasons (town gas) and utilized for multiple other applications until the mid-1900s. The conversion from coal to gas was also regarded as an opportunity to minimize the dependency on petroleum from uncertain sources. Biomass as a feedstock for gasification offers an opportunity to use wastes and residues and simultaneously lower carbon emissions [7]. The produced gas is very versatile to be utilized in gas turbines or power gas engines and can be further processed into liquid fuels [31].

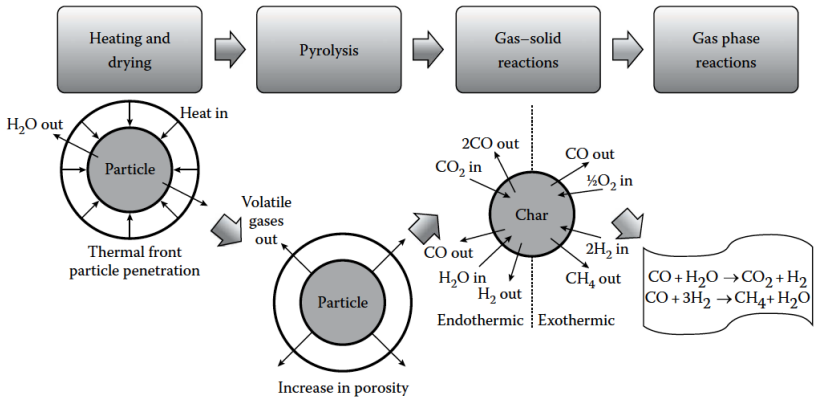

Figure 2.4: *Steps of biomass gasification in a gasifier [7], reprinted with permission*

The gasification of solid biomass also includes multiple steps: heating and drying, pyrolysis, gasification, and oxidation (in case air or oxygen is used). All of these reactions occur both in solid- and gas-phase, as pictured in detail schematically in Figure 2.4.

The phase of heating and drying is essential to remove the moisture from the solid biomass at around 100 °C. During this time, no chemical reaction takes place [7]. The time required for this step depends primarily on the moisture degree, which is highly variable in biomass, and secondly on the temperature, the particle size, and density of the feedstock [7, 8].

After the drying process, the temperature of the biomass particle rises until the chemical decomposition in the absence of oxygen, namely, pyrolysis, starts. First, the hemicellulose breaks down around 225 °C-325 °C, then cellulose at around 300 °C-400 °C. Lastly, the highly complex and robust lignin decomposes at temperatures up to 500 °C, though the process can also begin at cooler temperatures. Lignin is the component that produces the greatest quantity of solid products. This will be the determining factor for the char production in the next steps of the mechanism. A gaseous stream consisting of hydrogen, carbon monoxide, carbon dioxide, methane, light hydrocarbons, and high molecular weight hydrocarbons are formed during the pyrolysis step. The hydrocarbons with a high molecular weight are either combusted in a later step or contribute to the tar fraction. Furthermore, the pyrolysis leads to a stream of volatiles and a solid charcoal product, their yield depending on heating rates, particle size, the interaction of temperatures, effects of catalysts, the nature of the feedstock, and the existence of non-combustible components [7, 56].

During the latter steps, the char reacts primarily with water and carbon dioxide during gas-solid reactions. Furthermore, homogeneous gas-phase reactions take place [7, 58].

Table 2.2: *Basic chemical reactions during gasification based on [7] [31]*

Reaction	
$C + \frac{1}{2} O_2 \longleftrightarrow CO$	Partial oxidation
$C + O_2 \longleftrightarrow CO_2$	Complete oxidation
$C + 2\,H_2 \longleftrightarrow CH_4$	Hydrogenation
$C + CO_2 \longleftrightarrow 2\,CO$	Boudouard Reaction
$C + H_2O \longleftrightarrow CO + H_2$	Water gas reaction
$CO + H_2O \longleftrightarrow CO_2 + H_2$	Water gas shift reaction
$CO + 3\,H_2 \longleftrightarrow CH_4 + H_2O$	Methane formation

The first five reactions in Table 2.2 show heterogeneous gas-solid reactions, converting solid carbon into carbon monoxide, carbon dioxide, methane, and hydrogen. The heat release is largest from the complete oxidation, while partial oxidation only generates 65 % ([31]) of this heat in comparison. The last two reactions show further development of carbon monoxide and hydrogen and, furthermore, a higher yield of methane and carbon dioxide in the produced fuel gas via gas-phase reactions. The last two reactions depend very much on the conditions, shifting in any direction.

Overall, the final gas composition will be determined by the residence time, temperature, and pressure within the gasifier, by the fuel composition and amount, by the heat distribution within the gasifier, and the type and amount of gasifying agent that is utilized, all influencing the calorific value of the product gas. A low calorific gas is produced when using air as a gasifying agent, which is used directly in combustion or as an engine fuel. A product gas with a medium calorific value is produced when utilizing oxygen or pure steam as a gasifying agent, which serves as a feedstock for a conversion into chemicals like methane or methanol. Lastly, a product gas with the highest calorific value is achieved when using hydrogen as a gasifying agent or during hydrogenation [7, 31, 57]. At usual gasification conditions, though, hydrogen is not an optimal gasifying agent due to more complex reaction mechanisms than, i.e., with steam. During carbon conversion in chars and coals with hydrogen, the reactivity can fluctuate greatly [59].

To achieve the conversion of biomass via gasification, multiple gasifier types subdivide primarily into fixed-bed, fluidized-bed, and entrained flow gasifiers, utilized as continuous processes, as exemplified in Figures 2.5 and 2.6 [8]. They differ in how fuel and gas get in contact, the heating mode, and the flow patterns between the biomass and gas [7]. The choice of gasifier depends, amongst others, on the quantity of produced gas, the utilization [52], and primarily on the power-to-be-installed and the available biomass.

For small and medium-scaled applications, the most traditional fixed-bed gasifier systems are most suitable, generally leading to low calorific product gases and operating at around 1000 °C. Depending on the direction of flow of the gasifying agent, these technologies can be classified as updraft (Figure 2.5, left), downdraft (Figure 2.5, right) or with a cross-flow [31, 42].

In an updraft gasifier, the biomass feedstock is introduced gastight at the top and the oxidizer at the bottom of the gasifying unit. This is considered to be the simplest technique. The feedstock and oxidizer move in an opposing direction, the biomass going through the stages of drying, devolatilization (pyrolysis), reduction (gasification), and combustion. Some of the char settles on the grate in the combustion zone, or „hearth zone“ state, ashes fall through the grate at the bottom. The gasifying agent enters the combustion zone, reacting with the char at temperatures as high as 1200 °C, leading to carbon monoxide, carbon dioxide, and steam. This hot gas supplies the energy for the other process steps and gets cooled while it moves upwards. In the pyrolysis zone, considerable amounts of volatiles lead to large quantities of tar in the product gas, making the exit pipes prone for plugging. Due to the up-

draft, the tar does not have the opportunity to pass through the hot temperature zone for further reactions. On the other hand, a product gas with a low amount of particulates is produced due to the filtering effect of the feed. The gas exits the gasifier at around 80 °C-100 °C, leading to a high overall energy efficiency for this process [8, 31, 42].

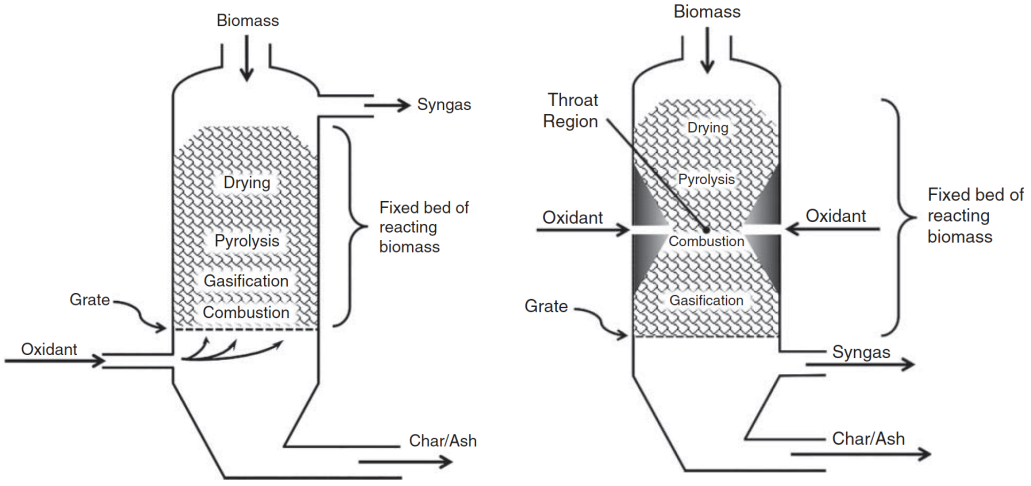

Figure 2.5: *Fixed-bed updraft (left) and downdraft (right) gasifiers [8], reprinted with permission*

In a downdraft gasifier (Figure 2.5, right), the gasifying agent is introduced in the middle or at the top of the reactor in a throat region, as opposed to the bottom in the updraft system. This leads to a coinciding flow of the solid biomass feedstock and the produced gas, which now exits the vessel at the bottom. Furthermore, the order of the hearth and reduction zones are reversed. This change in the configuration of the gasification zones dramatically reduces the tar content in the syngas when compared to the products from the updraft technique. The tar-rich volatiles now pass through a high-temperatured (800 °C-1200 °C) combustion zone after the pyrolysis. The tar can therefore efficiently be cracked, leading to high conversion rates. To achieve this, the introduced biomass feedstock must have a moisture content of less than 20 % to reach sufficiently high temperatures [8, 42]. When using the cross-flow technique, the feed of the biomass is descended, while the oxidizer is moreover introduced from one side and the product gas is eliminated on the other side. The combustion and reduction zones develop around the access point of the gasifying agent, the pyrolysis and drying zones are positioned higher in the reactor. A low efficiency due to product gas temperatures of up to 900 °C and high tar contents are achieved during this process [31].

Fluidized-bed reactors can be subclassified in bubbling (Figure 2.6, left) and circulating (Figure 2.6, right) gasifiers and are generally known for their homogeneous mixing and temperature distributions. The biomass feedstock, in combination with the gasifying agent and the material bed, is brought into a quasi-suspended „fluidized“ state.

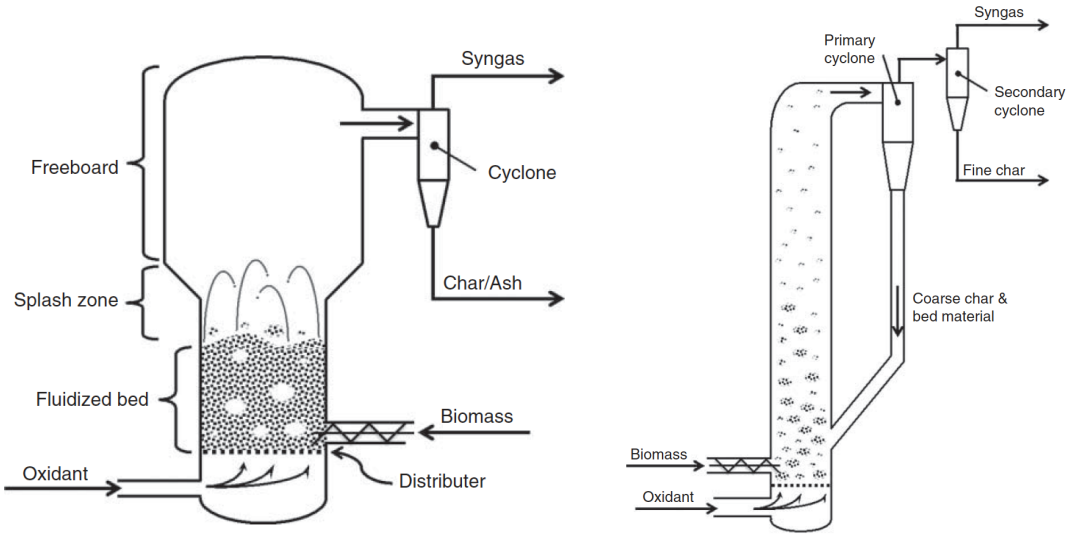

Figure 2.6: *Fluidized-bed bubbling (left) and circulating (right) gasifiers [8], reprinted with permission*

The bubbling gasifier was developed by Winkler in 1921 and is, therefore, the oldest commercially used fluidized-bed reactor. Primarily utilized for the gasification of coal then, it is now a popular choice for the gasification of biomass, especially due to its insensitivity to the quality of the feedstock and applicability for medium-sized units of $<25\,\mathrm{MWth}$ [28]. While the gasifying agent flows upwards through the bed, the material emerges into an emulsion of particles and gas bubbles, physically resembling a boiling fluid. The bed commonly consists of sand, dolomite, or alumina and can typically be fluidized by the agents air, oxygen, or steam. To maintain the fluidization in the bed, the volumetric flow has to be controlled, to finally be decreased in the freeboard by enlargement of the cross-sectional area. This lowers the velocity to return the particles to the material bed and increases the residence time of the gas-phase, prompting gas-solid and gas-tar reactions [8]. Alongside the uniformity of the temperature and mixing in the reactor, advantages of a bubbling bed include a yield of homogeneous product gas and high heat transfer. Downsides include large bubbles in the bed and hence some gas bypassing [7], a limit of the operating temperature due to ash slagging, and a high tar and fines content in the produced

gas [31]. Circulating fluidized-bed systems operate on the principle of evading the void of the material bed during the gasification process and are additionally useful when coping with high capacity throughputs. As the velocity of the gas increases, also the load of solids in the freeboard extends, resulting in a deficiency of particles in the bed material. This is avoided by including cyclones in the reactor, returning bed material and char via a downcomer to the reaction vessel, and to remove ash. Advantages of this process are the possibility to operate with rapid reactions, and, furthermore, achieve high heat transfer rates and high conversion rates. Disadvantages appear to be temperature gradients and a heat exchange, which is limited in comparison to the bubbling fluidized-bed gasification process [7, 8, 31].

For the sake of completeness, entrained-flow gasification is be presented shortly. This technique is favorable and widely used for large-scale coal, coke, and refinery residue processes, utilizing top-fed or side-fed gasifiers. Due to the need for finely ground feedstock material <0.1-0.4 mm, this process is not suitable for fibrous materials like biomass. Such pulverization is hardly possible, and the very short residence times in these reactors are therefore unfit for gasification of lignocellulosic material. This limits the use of entrained-flow processes for biomass feedstock strongly on a commercial scale [28, 31].

2.1.3 Combustion

One of the oldest thermochemical conversion process known to humankind is the combustion or burning of biomass. Until the early 1900s, a broad spectrum such as heating, cooking, the generation of steam, mechanical and electrical power, and the chemical and charcoal production was met by this technique. The basic stoichiometric formula for the burning of wood bases on the formula of cellulose $(C_6H_{10}O_5)_n$ [29]:

$$(\mathrm{C_6H_{10}O_5})_n + 6\,\mathrm{nO_2} \longrightarrow 6\,\mathrm{nCO_2} + 5\,\mathrm{nH_2O} \tag{2.2}$$

The understanding, the science, the knowledge of the chemical mechanisms, the thermal efficiencies, and emission rates of woody combustion have significantly developed since complex feedstocks and furthermore, waste feedstocks are being utilized in combustion or co-combustion systems [29].

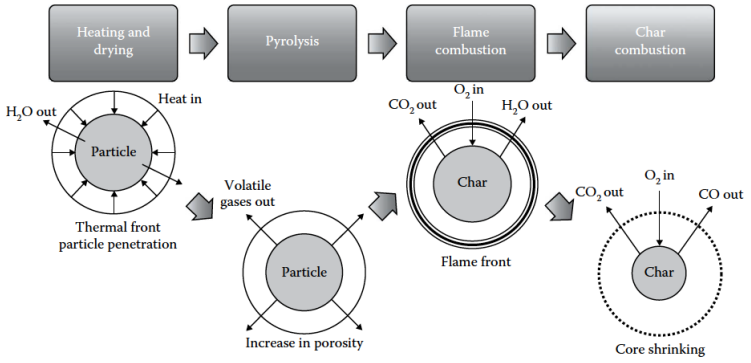

Figure 2.7: *The four steps of biomass combustion in a boiler [7], reprinted with permission*

This technique is based on the three Ts: high **t**emperatures for the ignition process, enough **t**urbulence for a complete mixture during the gas-phase combustion of the fuel and oxidizer, and a sufficient amount of **t**ime for the oxidation to occur. This is achieved during the four steps of heating and drying, pyrolysis, flame- and finally char combustion, as can be seen in Figure 2.7.

The steps of heating and drying and pyrolysis have been thoroughly discussed in section 2.1.2. Because these are both globally endothermic steps, they require an external energy supply to take place. This is achieved by providing an external source of heat or by the addition of air for partial oxidation [7, 58].

To complete the thermochemical processes during combustion, the volatile gases act around the solid fuel. Additionally, an adequate amount of oxygen needs to be present for the final two steps. If this is not the case, incomplete combustion can result in the formation of polycyclic aromatic hydrocarbons (PAH), soot, and other organic compounds in the resulting flue gas. The charcoal, mainly consisting of carbon, continues to react to carbon monoxide and carbon dioxide, being controlled by the transfer of oxygen to the surface of the char. The reaction of the char takes place on the surface or inside of its pores [7, 56].

The scale of combustion plants ranges from primitive, small-scale traditional cooking stoves to furnaces used for CHP or power generation applications, ranging from kilowatt to multi-megawatt sizing [3, 8]. Three classic types of combustion systems are fixed-bed, fluidized-bed, and entrained flow reactors. The smallest fixed-bed combustors are simply made of one combustion chamber and a grate, with primary and secondary air supply above and below this grate, to ensure the combustion of volatiles and char, respectively [56]. Further applications are found using manually-fed systems, spreader-stoker systems, underscrew systems, throughscrew

systems or static and inclined grates. In comparison to the fixed-bed technology, fluidized systems seem more sufficient in large scale applications and exhibit greater combustion efficiencies due to a homogeneous distribution of the temperature in the reactor, operating at slightly lower temperatures from 700 °C-1000 °C. Silica sand, limestone, dolomite, or other non-combustibles are utilized as the bed for the biomass and act as the heat transfer medium by high-pressured air flowing from the bottom up. Based on the velocity of the air, this technique can be subdivided into bubbling or circulating fluidized-bed systems [42, 56]. Lastly, combustion can be conducted in an entrained flow by transporting the feed into an externally heated tube by a cooled injector. The feed consists of fuel particles and air, and it is ignited by a burner at the access to the reactor [42].

2.1.4 Liquefaction

The final thermochemical conversion process to be presented is the biomass liquefaction. This process was introduced at the beginning of the 20th century, peaking in 1914 when Bergius introduced his procedure of coal conversion in the presence of hydrogen. [8] The feedstock is converted into oxygenated hydrocarbons in high pressured hydrogen environment at low temperatures [3]. The lignocellulosic macro-molecules are broken down with a catalyst present, leading to fragments of light molecules. These unstable and reactive fragments continue to repolymerize into oily liquids. The primary goal is liquids of higher quality than those attained during the pyrolysis process, in the sense of lower oxygen content or higher heating values, to avoid extensive upgrading due to hydrogen [5].

The main objective of the liquefaction process is the increase of the H/C ratio, with a necessary decrease of the O/C ratio, from the biomass to the product. Hence, adding hydrogen or carbon monoxide as reducing gas is essential. The removal of oxygen is chemically feasible by producing water or carbon dioxide; the latter process leads to a product with a higher H/C ratio and, therefore, a higher lower heating value (LHV) [5]. The utilization of catalysts is especially critical in this thermochemical conversion process to reduce the reaction temperature, increase the yield of desired liquids, enhance reaction kinetics, and decrease the formation of residues [56]. Typical catalysts are acids and alkalis. Furthermore, the consistency of the feedstock slurry in the employed solvent (water or other) is crucial [5].

Chapter 3

Combustion of gaseous fuels

A deeper understanding of the diverse laminar and turbulent combustion processes can be gained with this chapter. The basics of non-dimensional numbers or burning effects for premixed and non-premixed techniques are investigated. Finally, the focus is on counter-flow combustion, which is the main interest of these numerical and experimental investigations. Furthermore, biomass-based and methane fuels are presented in reference to properties like gasifying agents and oxygen enhancement.

3.1 Laminar and turbulent combustion

In this chapter, the fundamental differences between laminar and turbulent combustion will be discussed. Combustion regimes will be defined, also by further characterizing non-dimensional numbers. The concept of laminar flamelets as thin layers embedded in turbulent combustion flow fields is also presented [39].

Combustion processes are based on the mixing and burning of fuel and oxidizer. This procedure can be further categorized by mixing fuel and oxidizer and then burning it subsequently (premixed) or by mixing and burning fuel and oxidizer simultaneously (non-premixed). These processes can again be subdivided based on laminar or turbulent flow types of fuel and oxidizer [32].

In basic terms, a laminar flow can be identified as a regular, steady, and smooth flow of fluids when they are highly viscous or slowly moving. When these characteristics change, by regarding fluids with a lower viscosity or by increasing the velocity, the movement of the flow gradually becomes chaotic and irregular, therefore turbulent. The instabilities caused by flow perturbations induce the change from a laminar to a turbulent flow type, also passing a transitional state [60,61]. The non-dimensional

Reynolds number (Re) is used to categorize the effects of inertial and viscous forces on flow fields. Furthermore, it helps to distinguish between the laminar and turbulent flows of fluids, as well as the transitional period [61, 62].
The Reynolds number can be defined as follows [62]:

$$Re = \frac{\rho u d}{\mu} \tag{3.1}$$

With ρ as the density of the fluid, u as the velocity of the fluid, d as the diameter as a characteristic dimension, and μ as the dynamic viscosity of the fluid. Depending on disturbances, a change in flow type is usually expected around Re ~2000; this is also based on the type of reactor and further installations [62].

3.1.1 Laminar premixed combustion

The process of laminar premixed combustion can primarily be applied in industrial, residential, or commercial processes like, i.e., heating appliances, ovens, or bunsen burners. Basically, the comprehension of the laminar flame is a crucial requirement to further understand the mechanisms in turbulent flames. Similar physical processes underly both in laminar and turbulent combustion; therefore, laminar structures often establish the basis of turbulent flow theories [63]. A central task for studies of premixed and also non-premixed combustion processes is to establish the laminar flame speed, next to concentrations and temperature distributions as further points of interest. The flames burning velocity S_l can be defined as the speed at which the flame front propagates relative to the unburnt gases of the combustion process [64].

The first laminar premixed flame created for laboratory use was the Bunsen burner, developed by Bunsen in 1855 [64]. It is shown schematically in Figure 3.1.

The structure of a premixed flame includes four main parts: the preheat zone (where the reactants are being heated), the inner-layer (where the radical formation takes place), the oxidation-layer (where the remaining reactions occur), and the post-flame zone (where hot products and NO_x evolve). The oxidizer (air) is induced by numerous ports on the side of the burner and introduced into the mixing chamber. The fuel is supplied from the side (or bottom) and adjusted via an aperture („orifice“) at the bottom, entering the mixing chamber, thus being premixed with the air. Upon arrival at the top of the burner, the gases are considered well mixed and, therefore, homogeneous. Via the orifice, the flow of the fuel can be adjusted, and the mixing of the fuel and air can be optimized accordingly.

When the fuel feed is regulated and constant, the flame is anchored near the top of the burner, remaining stationary. This Bunsen flame propagates normal to itself with S_l into the unburnt fuel mixture [9, 64].

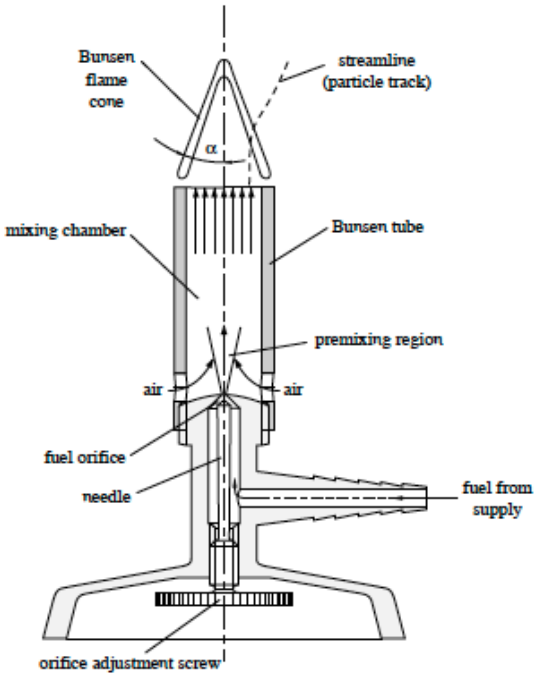

Figure 3.1: *Schematic overview of a bunsen burner [9]*

The laminar flame speed or laminar burning velocity for a premixed combustion with a Bunsen burner S_l can be presented as follows [64]:

$$S_l = V_t \frac{A_t}{A_f} \tag{3.2}$$

with V_t as the average flow velocity in the tube, A_t as the cross-sectional area of the tube, and A_f as the conical surface area of the innermost cone of the flame [64]. Chemical and physical properties like temperature and also the type and composition of the fuel type have an impact on the flame speed [11].

The combustion process of a premixed flame in a Bunsen burner is initiated when an external energy source heats reactive, combustible gases, and therefore triggers chemical reactions. This process continues without an external energy source when the heat produced during the originally initiated endothermic reaction is sufficient to further heat the unburned fraction of the reactive gases. The zone between the unburned and burned fractions is called the combustion wave. The movement of the combustion wave towards the unburned region is defined as propagation [65].

The analysis of the most basic and idealized mode of combustion wave propagation, like in a laminar premixed flame, which is based on various assumptions, is presented in Figure 3.2.

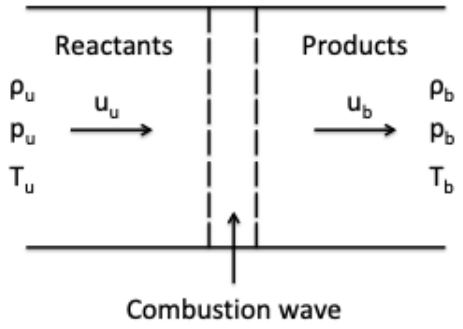

Figure 3.2: *Schematic overview of a 1-D premixed planar combustion wave based on [10]*

The subscript u indicates the conditions of the unburned gases before the wave, the subscript b the conditions of the burned gases after the wave. This wave propagation is adiabatic, steady, planar, based on ideal-gas laws, and relative to a combustible gas mixture. The flame can be described via the Rankine-Hugoniot relations, while the wave structure is ruled by the nonequilibrium processes of diffusion and reaction [10].

From the conservation equations, the following relations can be obtained [10]:

$Mass$:

$$\rho_u u_u = \rho_b u_b = f \tag{3.3}$$

$Momentum$:

$$\rho_u u_u^2 + p_u = \rho_b u_b^2 + p_b \tag{3.4}$$

$Energy$:

$$h_u + \frac{1}{2}u_u^2 = h_b + \frac{1}{2}u_b^2 \tag{3.5}$$

Where ρ_u and ρ_b are the mass densities of the fluids upstream and downstream of the wave, u_u and u_b the velocities upstream and downstream of the wave, f the mass flux through the wave, p_u and p_b are the pressures upstream and downstream of the wave and h_u and h_b the specific enthalpies in the two regions.

Because the flame propagates at a definite speed through the unburned mixture, it can be regarded as an interface to the burned mixture of an infinitesimal thickness. This flame sheet theory applies when there is a change of mixture properties from the fuel concentration in the burned region y_b=0 to the fuel concentration in the unburned region y_u and the burned gas temperature T_b to the unburned gas temperature T_u. After the flame front, the temperature of the reactants has increased to T_b, and the fuel concentration has dropped to approximately 0; the flame itself has broadened to a finite thickness. This is due to convection and diffusion processes, which will be further discussed in Section 3.1.2. Nonetheless, the chemical reaction itself takes place in a very limited region, where the maximum temperature prevails due to the high reaction rate. Towards the edge of the preheating zone δ_D, a finite reaction zone δ_R can be found, with $\delta_R \ll \delta_D$ [10, 11].

Starting with the earliest simplified analysis of laminar premixed flames by Mallard and Le Chatelier in 1883, some significant assumptions were made to explain the fundamental physical processes. This means, amongst others, to presume the non-dimensional Lewis number (Le) to be unity [11]. This is one of the non-dimensional numbers associated with basic diffusion processes, thermal and mass diffusivity, and the kinematic viscosity in laminar combustion [10].
The Lewis number Le can be defined as follows [10]:

$$Le = \frac{\alpha_h}{D_{i,j}} = \frac{\lambda_t c}{\rho c_p D_{i,j}} \tag{3.6}$$

with λ_{tc} being the thermal conductivity, α_h the thermal diffusivity, ρ the density, c_p the specific heat capacity at constant pressure, and $D_{i,j}$ the mixture-averaged diffusion coefficient (mass diffusivity) [66].
The Schmidt number (Sc) brings the momentum diffusivity in relation to the mass diffusivity [10]:

$$Sc = \frac{\nu}{D_{i,j}} = \frac{\mu}{\rho D_{i,j}} \tag{3.7}$$

also including μ as the dynamic viscosity. The measure of the relative influence of the momentum diffusivity to thermal diffusivity is considered the Prandtl number (Pr) [10]:

$$Pr = \frac{\nu}{\alpha_h} = \frac{\mu c_p}{\lambda_{tc}} \tag{3.8}$$

Le, Pr and Sc are related as follows [10]:

$$Le = \frac{Sc}{Pr} \tag{3.9}$$

Equation 3.9 shows the equality of the Lewis number to the ratio of the Schmidt number (Sc) and the Prandtl number (Pr), and therefore relevancy in a concurrent heat and mass transfer. The Lewis number also has an influence on the growth rate of the thermal and concentration boundary layers, which will concur when Le=1 [66].

The stoichiometry depends on the consumption of fuel and oxidizer by each other. A fuel-rich environment is based on a surplus of fuel, a fuel-lean environment, on the other hand, on the scarcity of fuel. Examples can be found in Table 3.1 [32].

Table 3.1: *Examples of stoichiometric, fuel-rich and fuel-lean laminar premixed combustion [32]*

Reaction	
$2\,H_2 + O_2 \longrightarrow 2\,H_2O$	stoichiometric
$3\,H_2 + O_2 \longrightarrow 2\,H_2O + H_2$	rich (H_2 left over)
$CH_4 + 3\,O_2 \longrightarrow 2\,H_2O + CO_2 + O_2$	lean (O_2 left over)

If a chemical reaction is made up of excatly 1 mol of fuel, the mole fraction of this fuel can be calculated for a stoichiometric mixture as follows [32]:

$$\chi_{fuel,stoichiometric} = \frac{1}{1 + \nu_{mf}} \tag{3.10}$$

with ν_{mf} expressing the number of moles of O_2 for a complete reaction to CO_2 and H_2O. Premixed combustion processes of fuel and air as oxidizer must take the existing N_2 into account and are therefore represented by the air equivalence ratio λ_{er}, which can be presented by the fuel equivalence ratio Φ_{er} [10, 32]:

$$\Phi_{er} = \frac{1}{\lambda_{er}} = \frac{\chi_{fuel}/\chi_{air}}{\chi_{fuel,stoichiometric}/\chi_{air,stoichiometric}} \tag{3.11}$$

Corresponding to these relations, premixed laminar combustion processes are divided into different categories, as shown in Table 3.2.

Table 3.2: *Categories in premixed combustion based on the air equivalence ratio Φ_{er} and the fuel equivalence ratio λ_{er} [32]*

rich combustion	$\Phi_{er} > 1$, $\lambda_{er} < 1$
stoichiometric combustion	$\Phi_{er} = 1$, $\lambda_{er} = 1$
lean combustion	$\Phi_{er} < 1$, $\lambda_{er} > 1$

3.1.2 Laminar non-premixed combustion

In a non-premixed combustion process, the mixing of fuel and oxidizer and the combustion itself occur simultaneously, as opposed to in a premixed environment. Applications include candles, campfires, oil lamps, and laminar counter-flow and laminar co-flow burners for research purposes. Due to the bigger range from 0 (being pure air) and ∞ (being pure fuel) in regard to the equivalence ratio Φ_{er}, a more complex chemistry develops in a non-premixed combustion process. The flame front is located where the stoichiometric composition $\Phi_{\mathrm{er}} = 1$ prevails due to the temperature distributions being surrounded by an area of rich combustion on the fuel side and lean combustion on the air side. Historically, the types of laminar flames were distinguished as premixed and diffusion flames. Since the diffusion process is part of all these flame combustions, the term non-premixed is used, giving this type of combustion a more unique notation [10, 32].
The air and fuel are moved towards each other through a convective motion and also via diffusion. During these transport processes, the temperature of fuel and air increases, and finally, they meet in the reaction zone and get mixed up rapidly [10].

Finally, in comparison to premixed flames, a laminar burning velocity can not be established for laminar non-premixed flames because of the missing propagation phenomenon. In premixed combustion, diffusive processes induce propagation. In the non-premixed laminar cases, the oxidizer and fuel diffuse to the flame front. The position of the flame front is fixed because the flame can not propagate into the oxidizer without fuel and vice versa. While oxidizer and fuel diffuse into the flame front, energy is released when converting them into products through chemical kinetics. Subsequently, the produced species and energy diffuse away into the lean air side and rich fuel side [32].

A complete reaction can not be established due to the finite rate of the reaction taking place and also the limited thickness of the reaction zone. Also, marginal amounts of fuel and air perpetually leak away from the reaction zone. An infinite reaction rate was assumed by Burke and Schumann [64], restricting the reaction zone to a reaction sheet. In this case, the air and the fuel are restrained to their particular zones, leading to marginal concentrations at the reaction sheet, preventing a leakage. If this infinite reaction rate is presumed, the stoichiometric rates of air and fuel transport control the combustion and, therefore, the rate of heat release. The limiting and controlling factor, accordingly, is the rate of diffusion, as opposed to the rate of the reaction [10].

One of the more straightforward methods to induce a laminar non-premixed flame is via a co-flow flame or jet flame, as presented in Figure 3.3. This kind of burner set-up merely includes two concentric tubes, with fuel flowing out of the center tube, while the oxidizer is supplied by the outer ring. Therefore, the adjunct co-flow. On the left image in Figure 3.3, a small divergence of the flame can be regarded at the burner rim, following a continuous divergence onto the centerline. The fuel ejects out of a vertical nozzle with a diameter of 2R and an axial velocity of V_e. The flow velocity decreases after exiting the nozzle, and the flow strays slightly. At first, the momentum of the fuel jet is preserved in the flowing field. Subsequently, as it enters the conical zone, this momentum is conveyed to the oxidizer (air), decreasing the velocity due to further reactions taking place. As the fuel jet proceeds downstream, more and more air is being dragged into the mixture.

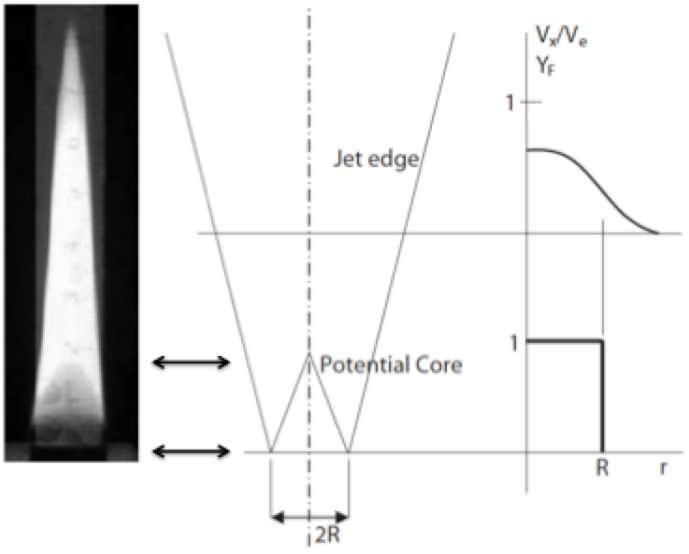

Figure 3.3: *A non-premixed co-flow flame (left) and the scheme of a non-reacting fuel jet (right) [11], reprinted with permission*

Also downstream of the flame, the jet edge (Figure 3.3, right side) expands gradually in diameter as it moves away from the conical zone („potential core“) at the nozzle. At the potential core, the velocity stays constant at V_e [11].
The height of the flame h can be approximated using the radius r, the velocity in the direction of the jet V_e, and the mean diffusion coefficient D_{mdc} in the mixture, as in the following correlation [32]:

$$h = r^2 \frac{V_e}{2} D_{mdc} \tag{3.12}$$

Two horizontal levels are included at the edge of the nozzle and around the center of the flame to examine the velocity distributions further. At the origin (nozzle), the velocity is distributed in a top hat form, while finally, the velocity and fuel concentration decrease down to zero constantly between the potential core when moving towards the jet edge. Downstream of the potential core processes like diffusion and viscous shear effects are effective all-over the area of the jet, with fuel molecules diffusing outward based on Fick´s law [11].

Because the velocity and fuel mass fraction are decreasing when moving further along the flame, the time for diffusion increases. The shape of the Burke-Schumann flame can evolve tulip-like in case of under-ventilation, or if the air supply exceeds the stoichiometric requirements and over-ventilates the flame, it forms a closed shape as pictured in Figure 3.4.

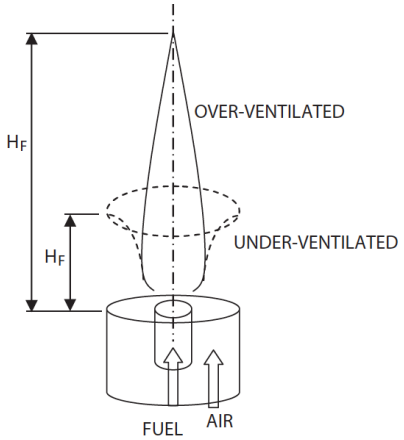

Figure 3.4: *Over- and under-ventilated Burke-Schumann flame [11], reprinted with permission*

The tulip-like shape in an under-ventilated environment forms due to the fuel diffusing outward seeking a higher amount of oxygen, resulting in an opened up shape with a smaller flame height $h = H_f$. This laminar non-premixed flame is less applicable for non-intrusive measurements due to its axisymmetric shape [11].

The Burke-Schumann flame is prone to buoyancy effects and is also impaired by the stabilization process at the rim of the nozzles. [10]. Finally, when studying laminar non-premixed combustion, counter-flow flames need to be regarded. This will be done in detail in Section 3.2.

3.1.3 Turbulent combustion

Turbulent combustion is one of the most challenging problems in science due to its increased complexity in the presence of multiphase flows and multiple and branching chemical reactions. When regarding industrial processes, combustion usually takes place in a turbulent rather than laminar manner. This is the case mainly due to heat release and mixing processes. First, flow instabilities (i.e., gas expansion and buoyancy) are induced by heat releases during combustion, leading to an increased transition to turbulence. Second, combustion is enhanced by mixing processes, which are accelerated by turbulence [38].

To gain an understanding of these kind of processes, a basic knowledge of the turbulence-chemistry interactions in reactive systems is necessary [67]. The characteristics of turbulent flames can be outlined mainly by length and time scales, non-dimensional numbers, and, furthermore, by thermal and molecular diffusivities and fluctuation intensity [68].

Turbulence induces a formation of eddies, leading to energy cascades from large-scale to small-scale eddies. This kinetic energy transfer is finally weakened by viscous dissipation, assumable only at the smallest length scale. Lengths widely agreed on in literature include [68]:

- Integral length scale (Λ_T): largest eddies in the flow, containing the most kinetic energy.
- Taylor length scale (λ_T): most active eddies in the flow, receive energy from larger eddies and dissipate to smaller ones.
- Kolmogorov length scale (η_T): smallest eddies in the flow.

Especially in numerical modelling of turbulent combustion, a determination of combustion regimes is essential. By relating characteristic turbulent and chemical scales, diffusivities, viscosities, and the previously defined length scales, non-dimensional

numbers can be used to categorize these regimes. The definition of the case-relevant time scales that control the flame is fundamental to describe a numerical system [67, 68].

The Reynolds number Re has been previously introduced as a way to categorize effects of viscous and inertial forces on flow fields.
In turbulent combustion Re is based on the integral length scale [68]:

$$Re_T = \frac{u' \Lambda_T}{\nu} \tag{3.13}$$

Defined by the turbulent intensity (u'), integral length scale (Λ_T), and additionally by the kinematic viscosity (ν) [68].

The Damköhler number (Da) is used to relate the turbulent flow time-scale to the chemical reaction time-scale (τ_T/τ_c), to define the nature of reaction and mixing in a combustion system [68].
The chemical time scale is defined by the ratio of flame thickness to the propagation speed ($\tau_c = \delta_L/S_L$). The ratio of integral length scale to turbulent intensity describes the turbulent flow time-scale ($\tau_T = \Lambda_T/u'$) [68].
Defining the Damköhler number in a turbulent environment as follows [68]:

$$Da_T = \frac{\tau_T}{\tau_c} = \frac{\Lambda_T}{u'} \frac{S_L}{\delta_L} \tag{3.14}$$

When regarding the smallest flow time-scale (Kolmogorov scale, τ_k), the Karlovitz number (Ka) is needed to describe turbulent combustion processes [68].
Defining the Karlovitz number Ka in turbulent combustion as follows [68]:

$$Ka_T = \frac{\tau_c}{\tau_k} = \frac{(\frac{u'}{S_L})^{1.5}}{(\frac{\delta_L}{\Lambda_T})^2} \tag{3.15}$$

Additional non-dimensional numbers in regard to diffusivities and viscosities were presented previously in Section 3.1.1.
Re, Da and Ka in turbulent combustion are related as follows [12]:

$$Re_T = (Da_T)^2 (Ka_T)^2 \tag{3.16}$$

Further dependencies in regard to premixed turbulent combustion processes can be found in turbulent premixed combustion regime diagrams in literature such as [68].

In comparison to premixed combustion, it is difficult to define regimes for turbulent non-premixed combustion processes. The computation of a reaction time-scale is challenging due to the non-distinctiveness of the flame velocity. Multiple flow scales, which can be spatially or temporally dependent, and additionally, further quantities like the reaction zone and the diffusion layer need to be defined [67]. Eventually, the separate introduction of fuel and oxidizer in non-premixed flames leads to an entrainment by larger-scale eddies. This prompts the formation of fuel-lean and fuel-rich cavities and also their local mixing, which can finally lead to a heat release due to quicker mixing at the molecular level than the chemical reaction. A modification of the turbulent flow occurs, enhanced by the volume expansion [69].

Three versions of the Damköhler number can be calculated regarding non-premixed flames. The differences are again based on the mixing time scales when deciding between the integral, local, or Kolmogorov scales for the computation of Da. When regarding sufficiently large or sufficiently small Damköhler numbers, two transitional versions evolve. The former, when the laminar flamelet assumption (LFA) applies leading to $\mathrm{Da_{LFA}}$, the latter, when extinction occurs introducing $\mathrm{Da_{EXT}}$ [67].

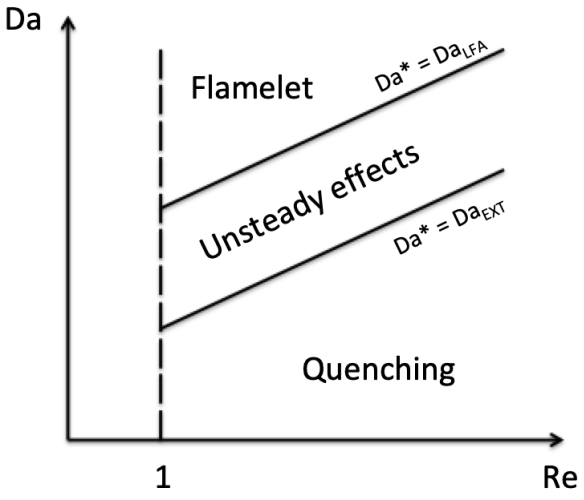

Figure 3.5: *Turbulent non-premixed combustion regime diagram based on [12]*

An attempt to characterize non-premixed combustion regimes is presented in Figure 3.5 and the following outline ([67], [69]):

- Laminar flames ($\mathrm{Re} < 1$): laminar diffusion flame, with no turbulence affecting the combustion.
- Flamelets ($\mathrm{Re} > 1$, $\mathrm{Da} \geq \mathrm{Da_{LFA}}$): steady laminar flamelets can be preserved in a turbulent regime. Reaction time scales are smaller than mixing time scales.

- Unsteady effects ($\mathrm{Re} > 1$, $\mathrm{Da}_{\mathrm{LFA}} > \mathrm{Da} > \mathrm{Da}_{\mathrm{EXT}}$): mixing time scales cause instabilities in the flame front and unsteady effects are dominant.
- Quenching ($\mathrm{Re} > 1$, $\mathrm{Da} \leq \mathrm{Da}_{\mathrm{EXT}}$): when the Damköhler number is sufficiently limited and small, the extinction of the flame occurs.

As discussed, combustion processes can generally be split into the classes of non-premixed or premixed combustion. In regard to turbulent technical procedures, prominently diesel engines or furnaces combust under non-premixed conditions, as opposed to homogeneous charge spark-ignition engines and gas turbines, which operate in a premixed mode.

The diesel internal combustion engine auto-ignites when a liquid fuel spray is injected into a cylinder with hot compressed air, therefore inducing partial mixing of the evaporated fuel and the air. This partially premixed gas is consumed quickly, and the following phase of the burnout takes place non-premixed. In gas furnaces, fuels are injected into preheated air, which might be partially mixed with exhaust gases. Following the ignition, the flame moves toward the nozzle until finally stabilizing at a certain point, resulting in the lift-off height. An area of partial premixing consequently develops between the nozzle and the lift-off height, followed by a region of non-premixed combustion further downstream [70]. Evidently, partially premixed combustion plays a role in non-premixed combustion, presenting a possibility of simultaneously reducing NO_x and soot formation, i.e., in diesel engines [71].

In a spark-ignition engine, fuel and air are premixed by turbulence and then compressed into the cylinder for an adequate amount of time before the mixture is combusted. An initial spark ignites the mixture, generating a flame that primarily grows laminar and then by turbulent flame propagation. Making the turbulent burning velocity a vital quantity in this type of combustion [70].

Details to gaseous combustion processes, in terms of oxidizer and fuel mixing, were previously discussed in Sections 3.1.1 and Section 3.1.2 on the basis of laminar combustion.

Another principle of subdividing turbulent combustion correlates to the ratio of turbulent to chemical time scales, leading to slow or fast chemistry cases. Here the focus lies on two mechanisms: autocatalytic reactions known as chain-branching and recombination reactions known as chain-breaking.
Above a certain crossover temperature, hydrocarbon oxidation occurs due to chain-branching reactions. At ambient pressure, the crossover temperature lies

between 950-1300 K, based on the reactive mixture. Below this temperature, the chain-breaking dominates the chain-branching and leads to extinction [72]. To avoid this extinction in a real-scale process, combustion operates at temperatures considerably above the crossover temperature to assure rapid chemical reactions, referred to as fast chemistry. Slow chemistry, on the other hand, is not as prone to turbulence, as it operates dependent on local temperature and pressure and also chemical composition [73].

3.2 Counter-flow combustion

The other main possibility to induce a laminar non-premixed flame, and the focus of this study is based on a counter-flow set-up. A counter-flow flame can be established by two opposed flows, one being fuel and the other oxidizer or via the *Tsuji* burner ([74]). Both can generally induce a „purer“ diffusion flame than a co-flow burner. Variations of different combustion parameters can be studied thoroughly in these kind of flames due to their one-dimensional and comparably simple behavior. This has been done for the later parts of the past century to clarify topics such as transport processes, extinction mechanisms, and complex chemical kinetics and correlations of these flat flames. Especially Smooke et al. [75–79] have investigated these types of flames in-depth experimentally and numerically [11].

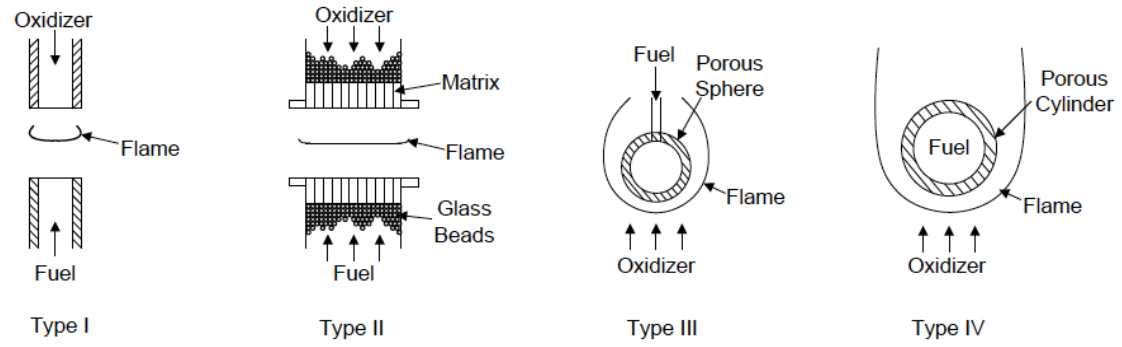

Figure 3.6: *Classification of counter-flow flames into Types I-IV from [13] commonly known from [14], reprinted with permission*

The counter-flow combustion was classified into two groups as previously established and again separated into four types by Tsuji, as can be seen in Figure 3.6. Types I and II are based on the counter-flow combustion, including two gaseous opposed jets. While type I includes rectangular nozzles or circular tubes as burners to induce flat flames, type II uses two matrix burners to eject the reactants. Burner types III

and IV are based on the forward stagnation region of a porous injector surrounded by free-streaming oxidizer, with III in a spherical or hemispherical shape and IV in a cylindrical shape [14].

When using a co-flow jet to induce a laminar non-premixed flame, a dead zone near the rim of the nozzles is established. This phenomenon is caused by heat loss close to the wall, decreasing temperatures, and therefore a decline of active radicals. Furthermore, this leads to small spaces of premixed zones at the base of the flame, effecting the structure and chemistry of this overall non-premixed flame. Accordingly, the presented burners in Figure 3.6 are thought to be more suitable to investigate certain fundamental processes of laminar diffusion combustion [14]. Moreover, experimental residence times are easier to control than with previously discussed set-ups, the flames can be stabilized by an inert co-flow, and finally, the transport of the reactants is controlled by convection, hence minimizing buoyancy effects [10, 13, 80].

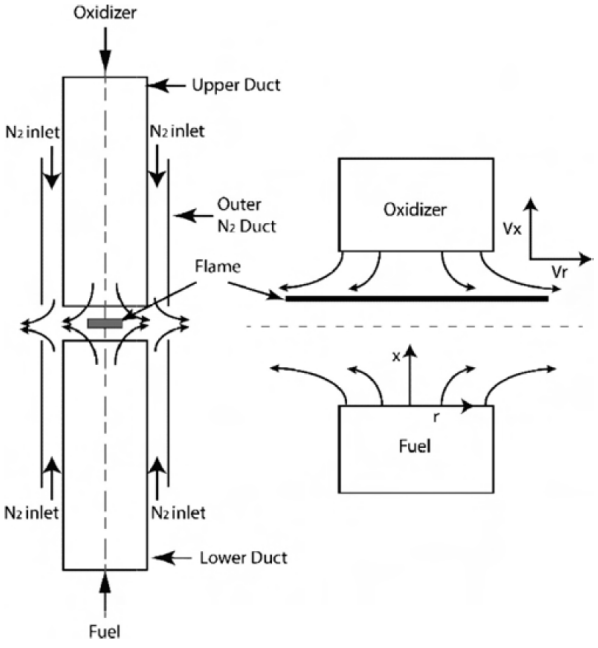

Figure 3.7: *Type I counter-flow burner set-up with a steady strained 1-D diffusion flame [11], reprinted with permission*

The structure of a diffusion flame as pictured in Figure 3.7 can be defined by the flame stretch K, which furthermore leads to the strain rate a. Despite its flat form and stationarity, aerodynamic straining leads to a stretch in counter-flow flames. Due to the symmetry in these flames, the strain rate can be related to the velocity gradient found at the centerline leading from the top to bottom nozzle; this also applies with unequal velocities of fuel and oxidizer [13, 81].

The global strain rate a can be represented by the densities of fuel and oxidizer ρ_F and ρ_O, the velocities of fuel and oxidizer V_F and V_O, and the burner separation distance L [13, 82]:

$$a = -\frac{2V_O}{L}\left[1 + \left(\frac{V_F}{V_O}\right)\left(\frac{\rho_F}{\rho_O}\right)^{1/2}\right] \tag{3.17}$$

The impact of strain on the combustion is not as well defined for non-premixed flames, as opposed to premixed flames and the non-dimensional Lewis number Le. Diffusion flames, though, are more inclined by flame extinction due to stretch. As the velocities of fuel and oxidizer, and therefore the strain rate a, increase, the residence time of the radicals decreases, leading to incomplete combustion. Ultimately, the residence time equals the chemical time; the heat release of the flame is insufficient in heating up the reactants, and the flame is blown off at this critical strain rate [13].

Following the ignition of the flame, the flow field acts aerodynamically complex. Before the flame is reached, the flow slows down, though then speeding up again when it is passed until the stagnation plane is reached. The radial acceleration is constant, while the axial velocities are fastest at the nozzle exits [83–85].

To determine the position of the flame relative to the stagnation plane, either the momentum of the streams or the volumetric flow of fuel and oxidizer and type of reactants should be established. The physical position of the diffusion flame is always located where the stoichiometric ratio is reached. The distance of the stagnation plane to the bottom nozzle $Z_{\text{stagnation}}$ can be represented by the densities of fuel and oxidizer ρ_F and ρ_O, the velocities of fuel and oxidizer V_F and V_O, and the burner separation distance L [82, 85]:

$$Z_{\text{stagnation}} = L - \left[1 + \left(\frac{V_O}{V_F}\right)\left(\frac{\rho_O}{\rho_F}\right)^{1/2}\right]^{-1} L \tag{3.18}$$

The flame front of the diffusion flame comprises the maximum temperature during the combustion process, while the temperatures decrease constantly down- and upstream in the directions of the nozzles. The fuel concentration is consumed upon reaching the flame front, while the oxidizer tries to diffuse to the fuel side persistently. The combustion products are mostly in the proximity of the flame front [14, 84]. Contrary to co-flow jet flames, do counter-flow flames seem relatively resistant to buoyancy instabilities after the positioning of the flame has taken place [80].

3.3 Laminar flamelets [in turbulent combustion]

Under certain circumstances, reactions in turbulent combustion are known to include thin sheets named flamelets that appear like narrow and steady laminar flames [86]. These flamelets are wrinkled and wrily due to the turbulent flow but seem to maintain the internal framework of a laminar flame, being physically one-dimensional and stationary in time [32, 87].

These approximations are, therefore, extensively used in large eddy simulations (LES) and Reynolds-averaged Navier-Stokes equations (RANS) for turbulent combustion process simulation. Flamelets can be steady or unsteady and non-premixed or premixed leading to several different laminar flamelet models [87].

Flamelet assumption theories presume a fast enough combustion chemistry, separating the flow into phases of burned gases and fresh gases that are parted by the so-called flamelet elements. These theories are also based on the assumption that the flamelet behaves explicitly like a laminar flame. The crucial information, though, is the structure of the flow and the narrow continuous region where the chemical reaction occurs. This region may also be thickened by limited turbulence without impairing the flamelet assumption theories [88].

Central components of all flamelet models are the definition and the effect of the flame stretch and the shape on the flame's behavior. These two properties have an extensive impact on the flames wrinkle and surface area A, as well as the local mass burning rate of the flame front [89].

The flame stretch K can therefore be defined by the surface area [88]:

$$K = \frac{1}{A}\frac{dA}{dt} \tag{3.19}$$

K changes the flame front spontaneously by increasing the flame surface via a high stretch leading to flame quenching or a small to moderate stretch causing surface production [88].

Amongst others, flamelet models either use a reaction progress variable C to describe the combustion evolution in the flamelet regime or the level-set function G as a starting point as introduced by Markstein in 1964 [32]. The G equation can be deduced from the spontaneous flame surface, with G representing a scalar field, with the flame front position located at $G = G_0$, $G > G_0$ in the burned mixture and $G < G_0$ in the unburned mixture [32, 90].

G can be described with the time t and the flame front location x_f and is presented by [90]:

$$G(x_f, t) = G_0 \tag{3.20}$$

The progress variable C is typically described by a combination of reactive scalars such as temperature, chemical species mass fractions, viscous-diffusive characteristics or chemical source terms defined by the vector ψ and can be calculated with the use of the mixture fraction Z as follows [91]:

$$\Psi = \Psi(Z, C) \tag{3.21}$$

The progress variable C has been interpreted variously, as found in [91].

3.4 Gaseous fuels

In this investigation, methane and diluted methane were considered for preliminary studies. Methane has a significant fraction in the composition of natural gas, and diluents are components in biomass-derived fuels. Furthermore, BDG, as presented in the following subsection, were considered experimentally and numerically.

3.4.1 Methane and diluted Methane

One of the main components of natural gas is methane, with a volume fraction of about $85 - 90\,\%$. An increased use of natural gas as an alternative fuel for internal combustion engines such as spark-ignition engines, or industrial power plants, leads to the need for further experimental and numerical investigation on the combustion behavior of this hydrocarbon fuel [92, 93].

A three-step mechanism, based on steady-state and partial equilibrium assumptions for the oxidation of CH_4, can be used to analyze the structure of a non-premixed counter-flow methane-air flame as presented in Table 3.3.

Table 3.3: *Three-step methane reaction mechanism [33]*

Reaction
I $CH_4 + O_2 \longrightarrow CO + H_2 + H_2O$
II $CO + H_2O \longleftrightarrow CO_2 + H_2$
III $O_2 + 2\,H_2 \longrightarrow 2\,H_2O$

The rates for these steps can be associated with the rates of the elementary reactions. Furthermore, the outer structure of this flame is based on the Burke-Schumann structure and dependent on the overall one-step reaction as follows [33]:

$$CH_4 + 2\,O_2 \longrightarrow CO_2 + 2\,H_2O \tag{3.22}$$

This mechanism is based on the four-step kinetical mechanism by K. Seshadri and N. Peters [94, 95], reducing the mechanism of hydrocarbon chemistry [96] of CH_4 to the fundamental steps, though still leading to a reasonable flame structure. These fundamental steps are connected to the rates of elementary reactions of the C_1-chain mechanism for the oxidation of methane [95, 97].

The dilution of fuels advances the progress of investigating hydrocarbon combustion processes and will therefore potentially improve technical industrial applications, such as maintaining thermal stabilization in combustors or reducing nitrogen oxides (NO_x) by exhaust gas recirculation. The reacting flow field is affected by dilution in fuel and/or oxidizer streams by altering reactions, the flame structure, flame stability, and also emissions via thermal, dilution, or chemical effects [98]. A thermal effect is induced by a change in physical properties due to an alteration of the fuel composition. Furthermore, a dilution effect alters the carbon structure of the fuel composition and the concentrations of reactive species, therefore, modifying their frequency of colliding. Lastly, a chemical effect results from the chemical participation of the diluents, leading to an increase or decrease of soot [99, 100].

Additionally, a hydrodynamic effect can impact basic combustion phenomena like mixing, entrainment, extinction due to strain, etc. A strong and diverging impact bears the choice of either diluting the fuel or the oxidizer stream [98].

3.4.2 Biomass-based fuels

In the early 1920s, the utilization of biomass gasification to supply fuel for motor vehicles evolved. Especially the government of Sweden promoted the conversion of

feedstock as fuel, establishing wood gas-fueled cars by the outbreak of World War II. After the war, the use of low-priced hydrocarbons terminated the interest in biomass-based fuels as engine fuel again [31].

Various products from gasification and pyrolysis, landfill gases, and syngas are considered to be BDG and have been reported in literature [47, 101–108].

The compositions of selected BDG from gasification and pyrolysis processes are listed in Table 3.4, where GG-X denotes products from gasification processes, and PG-X denotes product combinations from pyrolysis processes. Also, a few undefined gases with a volume fraction of $< 1\,\%$ were merged into the nitrogen fraction [47].

Table 3.4: *BDG fuel mixtures from thermochemical conversion processes, found in [47, 101–108]*

BDG	**CO**	**CO_2**	**H_2**	**CH_4**	**C_2H_4**	**N_2**	**LHV**	**Reaction agent**	**Biomass**
	$[vol.\text{-}\%]$	$[vol.\text{-}\%]$	$[vol.\text{-}\%]$	$[vol.\text{-}\%]$	$[vol.\text{-}\%]$	$[vol.\text{-}\%]$	$[MJ/kg]$		
GG-H	35.50	27.00	28.70	6.5	0	2.30	9.20	Air-Steam	Cellulose
GG-L1	27.92	30.11	35.39	4.36	0	2.22	8.60	Air	Pine wood
GG-L2	37.65	28.89	27.17	4.78	0	1.51	8.40	Oxygen-Steam	Pine wood
GG-W	20.00	12.00	18.00	2.00	0	48.00	4.60	Air	Wood
GG-S	24.00	0	21.00	0	0	55.00	5.20	Air	Biomass wastes
GG-Vä	19.00	13.20	12.00	5.80	0	50.00	4.90	Air	Wood
PG-D	56.80	4.20	21.60	10.20	5.10	2.10	15.80	-	Sylvester pine and spruce
PG-Le	51.10	25.80	8.70	8.30	2.50	3.60	8.80	-	Pressed oak and beech sawdusts
PG-Lu	26.00	61.50	1.60	8.30	0	2.60	3.90	-	Pine bark

The GG- and PG- compositions change depending on the biomass type, reactor parameters, process parameters, and gasifying agent. The main components of the gaseous fuels are N_2, H_2, CO, CO_2, and CH_4, and possibly smaller C_2-chained gases. The most commonly used reaction agents are air, oxygen, steam or a combination of these. The utilization of air as reaction agent leads to product gases with lower heating values, but also decreases the operating costs. The use of oxygen, on the other hand, leads to gaseous fuels with higher heating values to be used for the manufacturing of fuel cells and chemicals [7, 109].

To improve the use and application of BDG as an energy source, it is essential to gain a deeper insight into the combustion processes and further knowledge of flame structures, species development, temperature distribution, and such.

3.5 Combustion properties

The fuel derived from BDG, especially its quality, and the grade of the following combustion is based on many factors from the preceding thermochemical conversion process. The composition of the fuel gas and also the derived amount can be influenced by the type of gasifying agent, by the oxidizer that was utilized, a possible addition of water or steam to the process, a heat surplus or heat loss during the conversion, the development of PAH, soot and tar, biomass residence times, and such. This last section gives a short insight on these topics.

3.5.1 Gasifying agents

As previously presented, a gasification process can be classified based on flow patterns or methods of contact between biomass and gas, heating modes, type of reactor, or finally on the gasifying agent. Here generally, steam, air, oxygen, or oxygen-enriched air are utilized. When air is used as the gasification agent, the operating costs are low, but the deduced fuel gas has a relatively low LHV, as shown in table 3.4, with a high share of N_2. Furthermore, this high nitrogen content leads to a significant increase in volume of the product gas. Steam, on the other hand, leads to a product gas with a high CO_2 content. Finally, oxygen as gasification agent leads to a fuel with a higher-value, to be used in higher value utilization, such as fuel cells, but the production includes more considerable costs. In sporadic cases and during advanced gasification processes, hydrogen can be used as a gasification agent. This leads to higher yields of methane and hydrogen to carbon ratios and substantially higher heating values [7, 31, 110, 111].

For pyrolysis processes, no gasification agents are used, but next to the particle size, the inert gas flow has a big impact on the products and their yield. The inert gas can, for example, minimize volatiles, and therefore avoid secondary reactions [109].

3.5.2 Enhancement with oxygen

When generating product gas via gasification, based on the gasifying agent, produced fuels can include combustibles like CH_4, CO, and H_2, but can also contain up to 60 % or more of N_2 (or up to 30 % of CO_2), which does not combust. In these kinds of fuels, pollutant emissions can be noticeably decreased; however BDG bring about other challenges. The burning velocity and heat release are reduced by the large volume of inert gases, which finally leads to extinction or, in the worst case, lead to explosions due to H_2 or CO induced by stability issues. To improve and stabilize the processes when burning BDG, oxygen enhanced combustion is a beneficial technique. Enriched air as the oxidizer increases flammability limits and also the flame propagation velocity. This is due to the hydrogen in the syngas mixture and the increasing reactivity of the fuel, based on the increased share of oxygen in the combustion atmosphere. Furthermore, products of incomplete combustion and greenhouse gases like CO_2 can be additionally reduced [8, 112].

Also, the oxygen-enrichment of fuels can prompt the complete combustion of hydrocarbons in practical systems and reduce pollutants like soot or particulates. Stable components can be enhanced by small concentrations of oxygen to improve the previously mentioned difficulties. If used in combustion engines, an advantage of oxygen addition is the possibility to utilize fuels of inferior qualities [113, 114].

Chapter 4

Spectroscopic techniques

Spectroscopic techniques are based on the interaction of light with matter, such as, i.e., ionization, absorption, and scattering processes [18]. In the following chapter the emission of laser-induced fluorescence of formaldehyde and CH* chemiluminescence will be presented and investigated. Finally, the elastic Rayleigh scattering, to determine temperature fields in combustion, is also introduced. These are the three main spectroscopic techniques that were applied during this investigation of synthetic BDG from thermochemical conversion processes.

4.1 Laser-induced fluorescence

Atoms or molecules from a lower energy level can be elevated to an excited state of higher energy by chemical reactions, absorption of electromagnetic radiation, or electron impact. Upon spontaneous transition from the excited state to the lower energetic state, energy can be released, amongst others, in the form of luminescent radiation, most commonly experienced as fluorescence, phosphorescence, and also chemiluminescence [15, 115, 116].

As the excitation in both processes is induced by the absorption of photons, fluorescence and phosporescence can be summarized more generally as photoluminescence. These techniques differ basically in their involvement of a change in electron spin during the electronic energy transition [15]. Fluorescence is defined by a same spin multiplicity of the emitting state and the final state, commonly singlet states, [117] making them short-lived ($<< 10^{-5}$ s) [15]. A change in the electronic spin, hence an emission from a triplet excited state to a singlet ground state, leads to phosphorescence. Here, the lifetimes of the excited states can take up to seconds or minutes [15, 117].

The physicist Alexander Jablonski suggested a three-energy-level diagram to describe the process of luminescence, the more complex version established over the past decades including detailed mechanisms regarding absorption, fluorescence, and phosphorescence, i.e., is commonly known as the Jablonski diagram [15,118]. Figure 4.1 illustrates the excitation and emission photophysics that can be induced by a laser [117], elucidating the intra- and intermolecular electronic transitions [119].

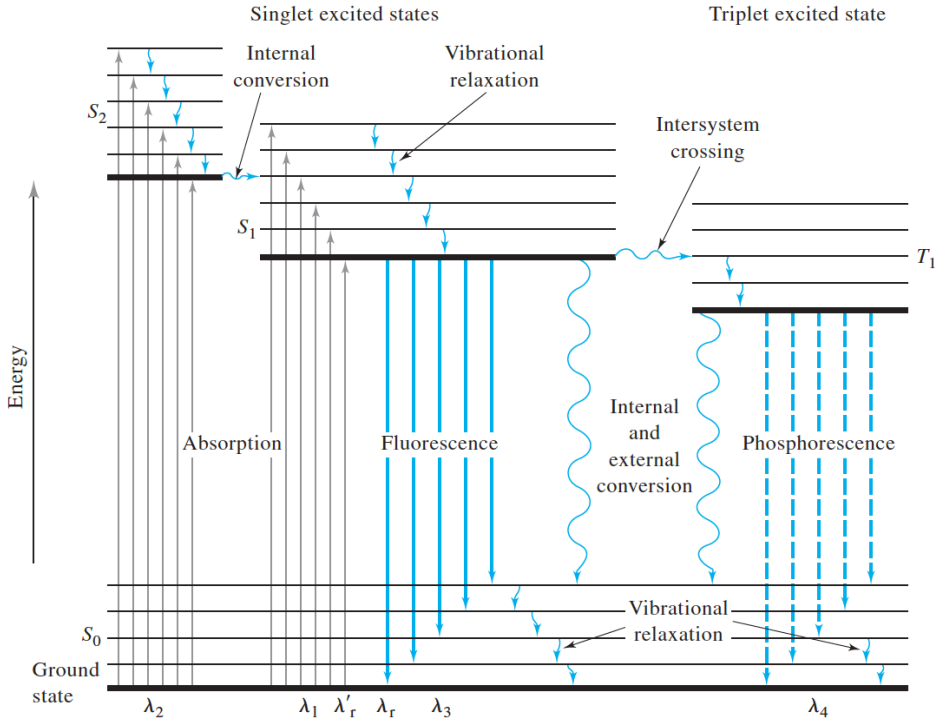

Figure 4.1: *Jablonski diagram [15], the basic version is commonly known from [16], reprinted with permission*

The initiating step when applying laser-induced fluorescence is the absorption of light by the analyzed molecule. The energy E of a photon equals to the difference between the lower and the upper energy levels [120]. The absorption spectra for polyatomic molecules are far more complex than for those of isolated atoms due to the various compositions of the rotational, vibrational, and electronic energies [15].

The energy E of a photon can hence be described as follows [15]:

$$E = E_{\text{electronic}} + E_{\text{vibrational}} + E_{\text{rotational}} \tag{4.1}$$

$E_{\text{electronic}}$ represents the energy states of the several bonding electrons (S_0, S_1, and S_2 in Figure 4.1) of a specific molecule. $E_{\text{vibrational}}$ describes the total energy of interatomic vibrations that take place in molecules. Finally, $E_{\text{rotational}}$ describes

the energy of the rotational states in a molecule. Typically a molecule has many vibrational and rotational energy levels; therefore each electronic energy state can be made of i = 1, 2, 3....n vibrational, and again each vibrational state of j = 1, 2, 3....m rotational states, leading to a magnitude of solutions for multiatomic molecules [15].

Figure 4.1 is a graphical representation of a small amount of electrons and their vibrational states. Potential absorption frequencies from the ground state S_0 to the first electronic state S_1 can be described as follows [15]:

$$\nu_i = \frac{1}{h_P}(S_1 - e'_i - S_0) \tag{4.2}$$

where ν_i stands for the absorption frequency, h_P Planck's constant, and e'_i represents the vibrational levels potentially ranging from i = 1, 2, 3....n. The energy differences between vibrational levels typically differ by a factor of 10-100. As each vibrational level includes multiple rotational levels, their differences in energy levels are much smaller [15].

The type of excitation is based on the wavelength of the induced light and, therefore, energy: electronic absorption is caused by ultra-violet or visible light, infrared light excites the vibrational levels, and microwaves, on the other hand, the rotational levels [120].

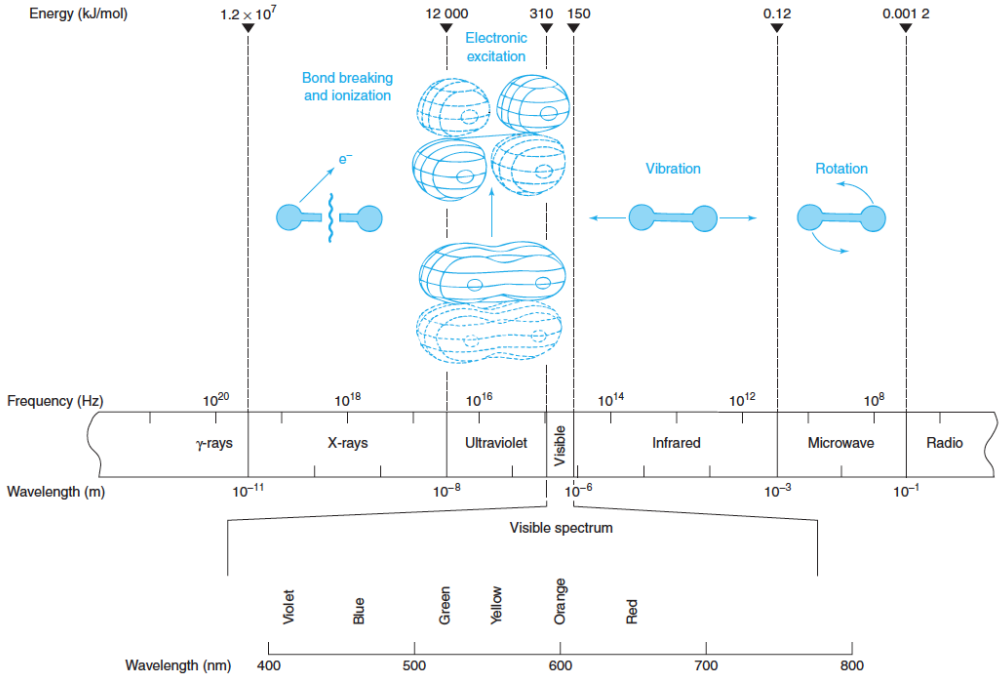

Figure 4.2: *Electromagnetic spectrum, defining the regions of electronic, vibrational and rotational absorption after light is induced [17], reprinted with permission*

Due to Formulas 4.1 and 4.2, discrete values of energy levels and frequencies can be determined. For the absorption spectra of atoms, this leads to discrete lines in the electromagnetic spectrum presented in Figure 4.2. Molecular absorption spectra, on the contrary, usually encompass a series of closely fit lines, which are only separated by fractions of nanometers, that finally create an absorption band. This is based on multiple electronic transitions and moreover on their numerous vibrational and also rotational states, ultimately leading to an absorption region [15].

Upon being excited to higher energy levels via absorption of electromagnetic radiation, atoms or molecules decay rapidly to a lower energetic level via several processes, like nonradiative relaxation or luminescence. The principles of fluorescence and phosphorescence can be explained by the blue arrows in Figure 4.1.

The fluorescence process begins after the absorption with a decay from the excited, energetic State $S_{1,2,3...x}$ to the lowest vibrational level of S_1, via internal conversion and vibrational relaxation. An internal conversion can be understood as a transition without radiation between levels of the same spin. Here, the transition of a higher energetic level to a lower energetic level within a high vibrational state occurs when both energetic states $S_{1,2,3...x}$ and S_1 have the same energy. Finally, fluorescence is emitted when a molecule relaxes from the lowest vibrational level of S_1 to the ground level S_0 and emits a photon [17, 121].

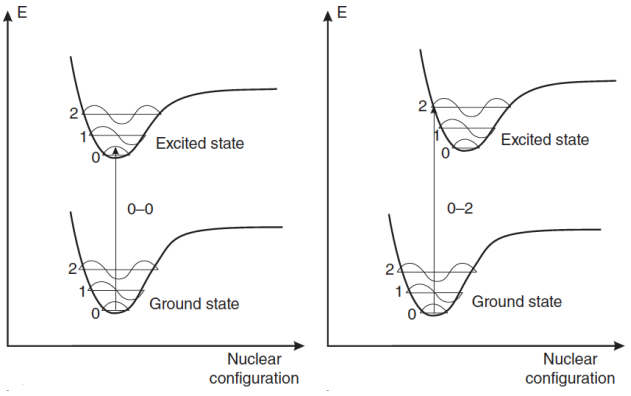

Figure 4.3: *Simultaneous electronic and vibrational change of energy levels with semi-stationary nuclei during the absorption or emission of a photon, which can be explained by the Franck-Condon principle [18], reprinted with permission*

Electrons and nuclei in molecules show considerable discrepancies when regarding their masses. On that account, electron clouds instantly adapt to changes of nuclear structures during vibrations, which can be described by the Born-Oppenheimer approximation. On the basis of this semi-stationary nuclear configuration, vibronic transitions, hence the concurrent change in electronic and vibrational energy lev-

els, can be explained with regard to Figure 4.3, using the Franck-Condon principle [18, 122].

During the vibronic transition, the nuclear positioning remains unchanged in the molecule, as the transition is much faster than the motion of the nuclei. The proceeding vertical transition (upwards or downwards) occurs from the ground vibrational state of the lower electronic level to the vibrational state in the excited electronic state that coincides best energetically. This goes along with the Franck-Condon principle of hardly changing the vibrational wavefunction and therefore retaining the state of the nuclei. A wavefunction with a peak right above the one in the ground state resembles each other most, leading to, i.e., $0:0$ or $0:2$ transitions as pictured in Figure 4.3 [18, 120, 122].

Alternatively to fluorescence, intersystem crossing of a molecule from the excited singlet state S_1 to an excited vibrational level of the excited triplet state T_1 can occur. This is a radiationless transition between states of a different total electron spin, typically favored when an atom with a high atomic number is present. The transition from T_1 to the ground level S_0 while emitting a photon is called phosphorescence. In this process, the lifetime is much longer in comparison to a fluorescence process due to the change in quantum spin numbers. This can be based on the improbability of the transition from two unpaired electrons (excited triplet state) to no unpaired electrons (ground state), which is actually a forbidden transition.

The molecule structure, possible solvents, temperature fields, and pressure have an influence on the rates of internal conversion, fluorescence, intersystem crossing, and phosphorescence [17, 18, 120]. Multiple effects can influence the intensity of emission during fluorescence or phosphorescence, also known as the quantum yield or efficiency.

The quantum yield for any luminescence is simply the ratio of luminescing molecules to those that were excited. This yield can lay between 0 and even reach an efficiency close to unity for highly fluorescing molecules like fluorescein. The deactivation processes of fluorescence and hence the extent of the fluorescence quantum yield Φ_f are determined by the rate constants k_x. Fluorescence k_f, intersystem crossing k_i, external k_{ec} and internal k_{ic} conversion, predissociation k_{pd} and dissociation k_d possibly lead to a deactivation of the lowest excited single state [15].

Φ_f can be determined as follows, permiting a qualitative analysis of the influencing factors of fluorescence [15]:

$$\Phi_f = \frac{k_f}{k_f + k_i + k_{ic} + k_{ec} + k_{pd} + k_d} \tag{4.3}$$

The chemical structure of molecules influences the dimension of k_f, k_{pd}, and k_d, while mainly the experimental environment dominates k_i, k_{ec}, and k_{ic}. Laser-induced fluorescence spectroscopy is a limited possibility of determining absolute concentrations of the quantum yield due to the limiting effects of the previously mentioned quenching processes [15, 120].

Another possibility to decrease the fluorescence intensity is dynamic or collisional quenching. This requires the contact between the excited molecule and a quenching agent Q with a high concentration having a rate constant of $k_q[Q]$ [123].
In a quenching process with one quencher Φ_f can be presented as [15]:

$$\Phi_{fq} = \frac{k_f}{k_f + k_i + k_{ic} + k_q[Q]} \tag{4.4}$$

When regarding the ratio of the quantum yields without $\Phi^0{}_{fq}$ and with Φ_{fq} a quencher, the Stern-Volmer equation is obtained, which describes the decrease in intensity during dynamic quenching [15, 123]:

$$\frac{\Phi^0_{fq}}{\Phi_{fq}} = 1 + K_q[Q] \tag{4.5}$$

where [Q] illustrates the concentration of the quencher and the K_q Stern-Volmer quenching constant defined as $K_q = k_q \,/\, k_f + k_i + k_{ic}$. Many molecules, for example, oxygen, halogens, amines, i.e., can act as quenchers [15, 123].

4.2 Rayleigh scattering

When electromagnetic radiation traverses matter, the greater fraction continues to pass in the initial direction, while a small fraction is scattered in different directions. The process can be separated into elastic Rayleigh scattering, induced by inhomogenities of the matter, elastic Mie scattering, and the inelastic Raman scattering, due to interactions with vibrational and rotational levels in the matter [18, 19, 120].

In comparison to the previously discussed luminescence processes, there is no exchange of energy between the scattering molecules and the incident light photon,

leading to an elastic Rayleigh and Mie scattering. During both of these techniques, the scattered light does not shift from its original frequency, hence wavelength. During the inelastic Raman scattering (and also fluorescence), on the other hand, photons induce a frequency-shift, as can be seen in Figure 4.4 [19].
Mie scattering occurs for molecules with larger diameters than the wavelength of the incident light $d > \lambda$, [15], while Rayleigh scattering occurs in smaller molecules with $d < \lambda$ [124].

To advance the knowledge of combustion phenomena or complex flow fields of gases, the use of laser-induced Rayleigh scattering measurements is a powerful diagnostic tool. Difficulties can arise due to a collective scattering of multiple molecules, a disturbance due to the inelastic scattering, background interference, or finally due to anisotropy [125].

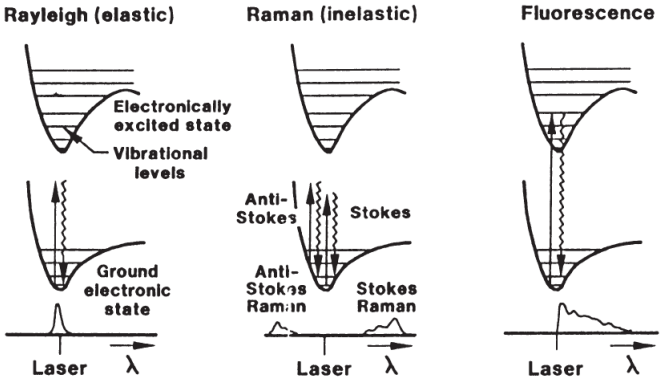

Figure 4.4: *Principle of Rayleigh scattering, Raman scattering and fluorescence [19], reprinted with permission*

As a diagnostic tool, next to flow fields and flame structures, densities, and possibly mixture fractions can be measured and, in case an ideal gas mixture can be presumed, temperatures can be derived [125].

To deduce temperatures via the number density N, the total Rayleigh scattering signal, which can be collected by a detector, is needed [34]:

$$S = \eta I N V_R \int_{\Delta\Omega} \left(\frac{\delta\sigma}{\delta\Omega}\right)_{mix} \delta\Omega \tag{4.6}$$

with η as the optical collection efficiency, I as the incident laser intensity, N the number density of the scatterers, V_R as the observation volume, $\Delta\Omega$ as the solid angle of the collection optics and $(\delta\sigma/\delta\Omega)_{\mathrm{mix}}$ as the differential scattering cross section of the gas mixture [34].

The differential scattering cross section can be represented by the sum of all species in the probe, weighed by mole fraction [34]:

$$\left(\frac{\delta\sigma}{\delta\Omega}\right)_{mix} = \sum_{n=0}\left(\frac{\delta\sigma_i}{\delta\Omega}\right)X_i \tag{4.7}$$

with X_i as the mole fraction of the i^{th} species.

The total Rayleigh cross section σ has to be depicted for a specific wavelength λ and can be presented for standard temperature and pressure (STP) as follows [34, 125]:

$$\sigma(\lambda) = \frac{24\pi^3}{\lambda^4 N^2}\left(\frac{n(\lambda)^2-1}{n(\lambda)^2+2}\right)^2 F_k(\lambda) \tag{4.8}$$

with $n(\lambda)$ as the refractive index and $F_k(\lambda)$ as the King correction factor.

The King correction factor accounts for depolarization [126] and can be represented for the depolarization ratio $\rho_0(\lambda)$ as follows [34]:

$$F_k(\lambda) = \frac{6+3\rho_0(\lambda)}{6-7\rho_0(\lambda)} \tag{4.9}$$

The depolarization rate $\rho_0(\lambda)$ has a finite value for asymmetric scatterers, but holds the value zero for spherically symmetric molecules and represents the ratio of horizontally to vertically polarized light $\rho_h(\lambda)/\rho_v(\lambda)$ [34]. (The theory regarding this topic will follow at the end of this chapter.)
With $a(\lambda)$ defined as the mean molecular volume polarizability and $\gamma(\lambda)$ the mean molecular volume anisotropy, $\rho_0(\lambda)$ can be presented as follows [34]:

$$\rho_0(\lambda) = \frac{6\gamma^2(\lambda)}{45a^2(\lambda)+7\gamma^2(\lambda)} \tag{4.10}$$

When finally introducing the molar refractivity R_L as [34]:

$$R_L = \frac{n^2(\lambda)-1}{n(\lambda)+2}\frac{N_A}{N} \tag{4.11}$$

with N_A as the Avogadro constant.

With the inclusion of 4.8, 4.9, 4.10, and 4.11, and the assumption that the incident light is polarized linearly, the solid angle is of a small finite value and the scattered radiation is viewed perpendicular to the polarization vector, [34] the differential cross section can be presented as [34]:

$$\frac{\delta\sigma(\lambda)}{\delta\Omega} = \frac{9\pi^2 R_L^2(\lambda)}{\lambda^4 N_A^2} \frac{6}{6 - 7\rho_0(\lambda)} \tag{4.12}$$

Table 4.1: *Depolarization ratio and differential scattering cross sections of major BDG gases and air [34, 127, 128] and own calculations*

Species	$R_L(\lambda)$ $(cm^3 mol^{-}1)$	$\rho_0(\lambda)$	$\delta\sigma(\lambda)$ / $\delta\Omega$ **(E-28** cm^2**)**	**References (values for calculation)**
N_2	4.484	0.02019402	6.22795	[127]
O_2	4.065	0.05447471	5.24460	[127]
CO_2	6.690	0.07525743	15.00290	[127] [128]
CO	5.034	0.01070242	7.84689	[127] [128]
CH_4	6.630	0.00000000	13.43060	[127]
H_2	2.086	0.01783944	1.34567	[127]
Air	4.393	0.02843004	6.10360	[127] [128]

For the major combustion species in BDG and air, the depolarization ratio, the molar refractivity, and the calculated differential cross sections at STP for $\lambda = 532\,\text{nm}$ are tabulated in Table 4.1.
Due to the temperature dependency of the mean molecular volume polarizability a(λ) and the mean molecular volume anisotropy $\gamma(\lambda)$, the differential Rayleigh cross sections for gases can undergo a rise of $0.4 - 2.8\,\%$ per 1000 K for a $\lambda = 532\,\text{nm}$ [34].

The determination of temperatures based on Rayleigh scattering also depends on the ideal gas law [129]:

$$pV = nRT \; or \; pV = NkT \tag{4.13}$$

the development of heat also influences the number density of the fuels. An increase of T from STP to about $T_{max} \sim 2100\,\text{K}$ (factor of about 7) in experimental combus-

tion of hydrocarbon flames as performed, deduces the Rayleigh scattering intensity to about $1/7^{\text{th}}$.

As previously mentioned, the depolarization can be defined as the ratio of horizontally to vertically polarized light or as the ratio of perpendicular to parallel light to the original beam when the laser source is polarized, as shown in Figure 4.5 in the yz plane [15].

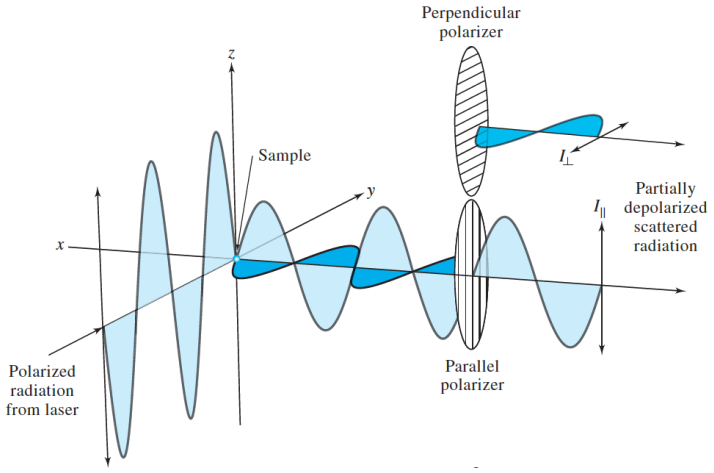

Figure 4.5: *Principle of polarization [15], reprinted with permission*

Horizontally (perpendicular) and vertically (parallel) polarized experimental images can be obtained by inserting a polarization filter between the sample (flame in between burners in the case of this work) and the ICCD camera and operating this filter at a 90° or 0° angle, respectively. The light source should previously be confirmed to be vertically polarized as described in [130]. Details in regard to these topics will be given in Section 5.1.

The Rayleigh scattering cross sections are generally a factor of 1000 larger than the corresponding Raman cross sections, commonly leading to higher spatial and temporal resolutions in Rayleigh measurements. However, due to a missing shift in frequency after the light has been scattered by the molecule, experiments are much more affected by the scattering processes of the background [124]. Finally, non-premixed combustion makes a determination of temperature fields more complicated, due to the incomplete mixing and also essentially due to the generation of new species. A numerical model can anticipate this and calculate accurate cross sections, to compare numerically and experimentally derived results. [124].

4.3 Chemiluminescence

The phenomenon of chemiluminescence has already been mentioned as a variation of luminescence in Section 4.1. An emission of light, as the relaxation of an excited molecule to its ground state, occurs. Originally identified and thought of as a „curiosity“ in research laboratories, this technique is now considered a simple and cheap but sensitive and selective measurement method. The types of luminescence can be differentiated based on their source of energy, like electromagnetic radiation leading to fluorescence or phosphorescence, heat leading to pyroluminescence, frictional forces leading to triboluminescence, electron impact leading to cathodoluminescence, crystallization leading to crystalloluminescence, and finally, chemical reactions leading to chemiluminescence [131, 132].

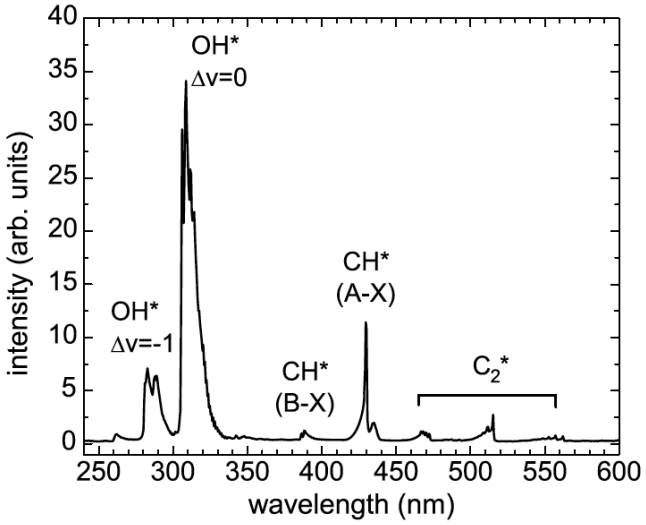

Figure 4.6: *CH*, OH* and C_2* spectra of a methane-oxygen-hydrogen flame [20], reprinted with permission*

The process of chemiluminescence in chemical reactions is limited to a small number of reactions only, therefore limiting the produced species. Most common in hydrocarbon-air flames are CH*, OH*, C_2*; their emission spectra are presented in Figure 4.6, and CO_2* in Figure 4.7 [15, 133].

The most basic type of reaction, where C* represents the excited state of species C, h_P Planck's constant, and ν_i stands for the absorption frequency, is presented as follows [15]:

$$A + B \longrightarrow C* + D \tag{4.14}$$

$$C* \longrightarrow C + \nu_i h \tag{4.15}$$

In combustion diagnostics for hydrocarbon flames, the technique of CH* chemiluminescence is frequently utilized to measure the heat release rate, to estimate the equivalence ratio, and to use the radical as a marker for the flame location. CH, as a short-lived molecule, prevails in a relatively narrow temperature and spatial area. Therefore, detailed chemical kinetic mechanisms of pollutant formation like NO_x can be advanced. The chemically excited CH* is responsible for the blue light in low-sooting flames; the essential CH* emission occurs at 314 nm, 390 nm, and 431 nm [133–136]. About 80 % of the excited CH emission occurs at 431 nm, as opposed to the residual excitation at 314 nm and 390 nm [137]. Lastly, all these characteristics make an excellent basis to validate the numerical solutions with experimentally derived results.

Previous research [138–143] has focused on the following three major reaction pathways for CH* chemiluminescence [133, 144]:

$$C_2 + OH \longrightarrow CH* + CO(R1) \tag{4.16}$$

$$C_2H + O \longrightarrow CH* + CO(R2) \tag{4.17}$$

$$C_2H + O_2 \longrightarrow CH* + CO_2(R3) \tag{4.18}$$

It must be stated, though, CH* prediction and reaction pathways are still under investigation and debate. This is mainly based on the uncertainty that remains within the C_2 and C_2H_2 chemistry [20].

With spontaneous emission of photons or destruction by collisional quenching following, as mentioned above. These pathways have been proposed [135, 145]:

$$CH* \longrightarrow CH + \nu_i h_P \tag{4.19}$$

$$CH* + N_2 \longleftrightarrow CH + N_2 \tag{4.20}$$

$$CH* + O_2 \longleftrightarrow CH + O_2 \tag{4.21}$$

$$CH* + H_2O \longleftrightarrow CH + H_2O \tag{4.22}$$

$$CH* + H_2 \longleftrightarrow CH + H_2 \tag{4.23}$$

$$CH* + CO_2 \longleftrightarrow CH + CO_2 \tag{4.24}$$

$$CH* + CO \longleftrightarrow CH + CO \tag{4.25}$$

$$CH* + CH_4 \longleftrightarrow CH + CH_4 \tag{4.26}$$

Furthermore, the CH* chemiluminescence signal S_{em} imaged onto a detector be expressed as follows [146]:

$$S_{em} = \frac{1}{4\pi} A_{21} \tau V_{em} N^* K_{em} \tag{4.27}$$

with A_{21} as the Einstein A ($= 1.86 \text{ x } 10^6\, 1/s$) coefficient, τ as the detectors exposure time, V_{em} as the volume of the pixel, N* as the number density of the excited species and K_{em} as the constant for the detector efficiency, and the solid collection angle [146].

Electronically excited species generally have a low concentration in flames because they are hardly produced, and when they are formed, they are quickly removed by quenching processes. A limitation by the formation rate is therefore presumed [133].

If background radiation like soot is present in (diffusion) flames, CH* chemiluminescence is weakened as a diagnostic tool. The incandescent soot particles can compromise luminescence measurements, even when using narrowband filters around 314 nm, 390 nm, or 431 nm, by inducing unwanted noise [144, 147].

This limited the studies when using this technique to investigate non-premixed diffusion flames due to the soot production in basic hydrocarbon-air flames. However, non-sooting diffusion flames, especially with hydrogen-mixed fuels, oxygenated fuels, or diluted fuels, can resolve this problem [147].

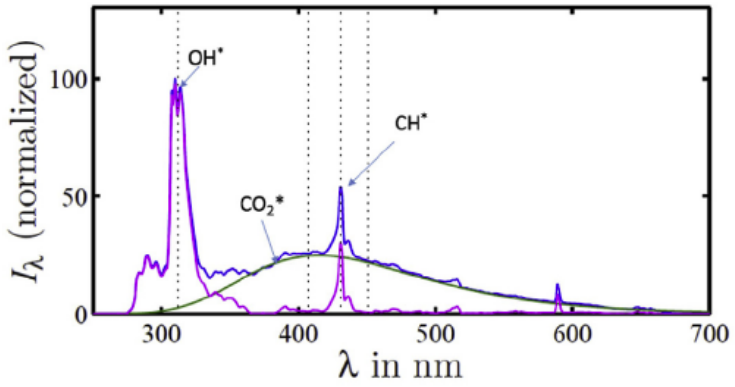

Figure 4.7: *CH*, OH* with and without CO_2* spectra in a hydrocarbon flame [21], reprinted with permission*

CH* chemiluminescence measurements can furthermore be influenced by „background“ radiation of CO_2* as pictured in Figure 4.7. Mainly between $300 - 600$ nm CO_2* chemiluminescence is present as a broadband emission in hydrocarbon flames, impacting the low concentration of CH* chemiluminescence peaks [21, 148].

4.4 Techniques

During the investigation of combustion processes, formaldehyde plays a central role, as it takes part in the oxidation of hydrocarbons, both in high and low-temperature regions [149]. Formaldehyde, being an essential intermediate species, makes it the subject of many studies, detecting, i.e., the flame front. Formed as part of the oxidation of hydrocarbon fuels, it is consumed during the ongoing combustion chemistry [150, 151].

Especially the excitation of this molecule via LIF or planar laser-induced fluorescence (PLIF), in many conditions and surroundings, has sparked an interest in many research groups. Some selected topics will be presented shortly in the following section.

The electronic transition of the $4_0{}^1$ ($A^1A_2 \leftarrow X^1A_2$) vibronic band of excited formaldehyde has been studied at elevated temperatures and pressures to investigate the sensitivity of the absorption spectra [152] and in decay rate investigations in a gas cell [153]. Furthermore, has the saturation behavior of the formyl radical been considered for flame front imaging in hydrocarbons regarding methane and dimethyl ether in the B-X band [154]. Laser-induced fluorescence was also utilized to advance the topic of scalar dissipation. By determining flame markers that enable estimates of the scalar dissipation rate at the stoichiometric surface of non-premixed flames [155], by the analysis of temperature and quenching corrections on the thickness of the layers in diffusion flames [26], and by planer LIF in a counter-flow diffusion flame with a stationary local extinction point [156]. Finally, formaldehyde PLIF in a Nd:YAG laser system was utilized to investigate and understand the origin of spectrally narrowband vs. broadband excitation in premixed and non-premixed flames [157].

More profound knowledge regarding quenching processes via excitation of formaldehyde at $\lambda = 355\,\mathrm{nm}$ were collected in a rich methane-oxygen flame for fluorescence lifetime imaging to be utilized for quenching corrections [158] and during studies of a dimethyl ether (DME)-air counter-flow diffusion flame to receive a representative formaldehyde profile, also taking signal quenching and the Boltzmann distribution into account [159]. Measurements at $\lambda = 355\,\mathrm{nm}$, utilizing an Nd:YAG laser system, were also used to identify oxygenated species of combustion in the reaction zones. A further understanding of the correlation between the presence and evolution of these species depending on the operating conditions in an ethylene-air flame of a McKenna burner was gained [160]. Lastly, also MILD combustion was monitored

via formaldehyde LIF to examine the entrainment of air effecting the flame structure when reducing the oxygen level [161]. The correlation of processes in cool flames to understand chemistry and transport phenomena in engines was also advanced using PLIF of formaldehyde. Partially premixed DME counter-flow cool flames were investigated after an addition of ozone [162] and subsequently also compared to hot flames [163], to show the increased profile and indifference of the cool flame speed to the equivalence ratio. Also, the development of formaldehyde in the pre-heat zones of methane-air premixed flames after adding ozone to the combustion were experimentally and numerically regarded [164].

Laser absorption diagnostics to sense formaldehyde in shock tube kinetic studies [165] or observe the thermal decomposition of formaldehyde behind a shock wave [166], to investigate and update mechanisms were performed.

The understanding of the formaldehyde molecule during combustion was also frequently explored directly in engine systems. The flame propagation in a spark-ignition engine was studied via LIF of formaldehyde. Fluorescence images made the tracking of the flame front possible due to the development of advanced program routines, hence deriving velocity measurements [167]. Diverse other processes were utilized to detect formaldehyde in other internal combustion engines (or exemplary systems), like obtaining approximations of a saturation intensity and possible existence of photochemical effects [150], detecting background fluorescence of PAH or other larger hydrocarbons simultaneously in a laminar counter-flow diffusion flame and in a single stroke spark-ignition engine [168] or investigating the gasdynamical and chemical processes that happen during the auto-ignition of endgas of an Otto engine [169]. Oxygenated species were identified in a pressurized flow combustor, based on a commercial diesel system [170], and low-temperature reactions during fuel composition or forming of PAH in high-temperature regions using a high-pressure cell [171], to advance the combustion processes in direct injection diesel engines, were considered.

LIF formaldehyde studies in an HCCI engine were frequently executed. Iso-octane and n-heptane were utilized to study the combustion process with formaldehyde as a marker for the first stage of ignition [172], for the spatial signal distribution at various injection timings [173], or to potentially use formaldehyde as fuel tracer in low-temperature reactions [174]. Further, to extract the formaldehyde contribution to the fluorescence spectra [175] during the ignition of diesel and n-heptane fuel sprays in an optically-accessible diesel engine for studies to be utilized in an HCCI

engine. Finally, formaldehyde PLIF was applied to study DME cool flames experimentally and numerically, playing a role in diesel engines, jet engines, spark-ignition engines, and HCCI engines, in a CARAT burner [176] or to investigate the low- and high-temperatured auto-ignition in high-pressure spray flames [177].

Furthermore, LIF techniques are extensively deployed to inspect BDG, and BDG derived from thermochemical conversion processes as, i.e., in [178–181].

Experimental and numerical investigations of heat release (maximum position, profile width, i.e.) in counter-flow flames [182, 183] and in a bunsen configuration [184] have been reported.

Though complexity is introduced by inelastic and elastic scattering induced by numerous molecules and anisotropy phenomena, laser-induced Rayleigh scattering is widely used to investigate complex flow fields and combustion [34, 124, 125].

Flow field and also flame structure, density, and mixture fraction [185, 186] can be determined by the intensity of Rayleigh scattering, furthermore temperature distributions [187]. To investigate complex flows [188] or the atmosphere [189], the spectrum of Rayleigh scattering needs to be observed.

Rayleigh scattering at 532 nm can be applied in rapid-compression machines [190], laminar and turbulent jet flames [191,192], premixed flames [193,194], for quantitaive vapor-fuel imaging [195] and comparable applications.

Furthermore, this technology can also be applied in lower wavelengths like the deep UV [196, 197].

To decouple Rayleigh scattering signals from background scattering atomic or molecular filters can be used, as presented from multiple research groups in [115]. This was applied with the use of iodine vapor or molecular filters [198–200], also in flames. Furthermore, atomic mercury filters can be used for ultraviolet filtered Rayleigh scattering measurements [201, 202].

To utilize Rayleigh scattering techniques in combustion or other applications, scattering cross sections [203], depolization ratios [128, 130], refractivities [127], polarizabilities [204] and anisotropy [205, 206] were defined.

Finally, the applications of CH chemiluminescense as a diagnostic tool in combustion are presented, while applications in other fields have been reported elsewhere [132].

Numerous research groups have evaluated CH chemiluminescence experimentally [20, 137, 144] and numerically [133, 134, 145] in low-pressure, non-premixed, premixed, i.e., flames.

Furthermore, the behavior during CH chemiluminescence in axisymmetric laminar [135], coflow diffusion [146], and counter-flow diffusion [136, 147] combustion was studied.

No research is known, where the presented techniques of laser-induced fluorescence of formaldehyde, laser-induced Rayleigh scattering, and CH chemiluminescence were investigated during counter-flow laminar diffusion combustion of the multiple synthetic biomass-based model fuels presented.

Chapter 5

Experimental set-up and conditions

As it is commonly used to induce stable, laminar diffusion flames, a counter-flow set-up was chosen for the following investigations. Preliminary experimental studies with two opposed McKenna flat flame burners [22], also used in a counter-flow set-up, have led to the need for a newly designed burner system as the centerpiece of the test rig. The spectroscopic measurement system is based around a pulsed Nd:YAG laser in combination with various optical and analytical elements and devices. Subsequently, extensive data processing procedures need to be applied. The application of experimental strategies and conclusions are presented in the following chapter.

5.1 Experimental set-up

An introduction of the considerations and developments of the in-house counter-flow burner system, as well as the Nd:YAG laser, the surrounding spectroscopic tools, and analytical devices, will be given in the following sections.

5.1.1 Counter-flow burner

The different types of counter-flow burners were already presented in Chapter 3.2. An opposed flow-induced laminar diffusion flame is initially achieved using two commercial McKenna burners of the American company Holthius & Associates (Figure 5.1, showing one burner).

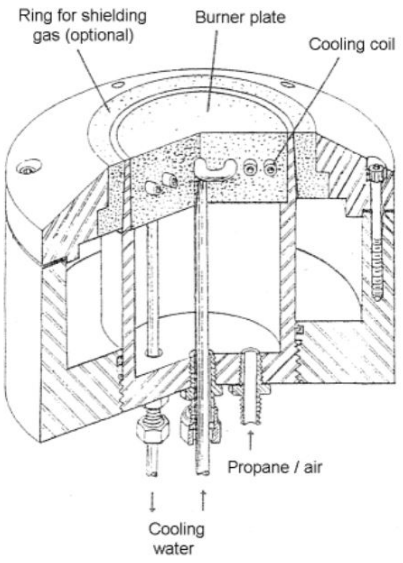

Figure 5.1: *Schematic sectional view of a McKenna flat flame burner [23]*

Via a screwed connection at the bottom of the construction, a gaseous medium can flow into the inner chamber of the burner and then stream through the porous burner plate. This plate is made of stainless steel and is, according to the manufacturering specifications, of a porosity of 54 %, with a pore size of $70 - 120\,\mu m$ [22]. Inside the plate is a cooling water coil, which is attached by two connectors at the lower end of the burner to a cold water circuit.
The inner chamber is surrounded by a shroud, which is also connected by a screw connection to the bottom of the burner. The outer chamber can be used to further insert (other) gaseous fluids into a separate area of the burner. These leave the construction over an annular, porous disc, which encloses the burner plate.

During the preliminary testing, the use of these commercial burners led to three different problems and, therefore, to the construction of an individual burner system for the experimental investigations.

First, for a laminar diffusion flame, these two opposed burners need to be in perfect opposite alignment. When having a slight misalignment of the nozzles, the flow of one nozzle bends to one side, whereas the opposed flow bends to the opposite side. Precision machining is necessary, so alignment is near perfect. Second, these burners, in an opposed flow set-up, are not constructed for high enough flow rates and, therefore, gas velocities. They are not long enough axially, so the flow does not have enough time to fully develop and smooth out radially before leaving the nozzle [13]. For the velocities and, therefore, strain rates that were to be investigated, a stable flame could not be established with this construction.

Figure 5.2: *Diffusion flames at L/D = 0.36 (left) and L/D = 0.83 (right) [23] induced by two opposed McKenna flat flame burners*

Finally, a distance between the burners of at least 18 mm needed to be reached while sustaining a stable, laminar flame for the laser sheet to be guided through the two opposed burners. The nozzle separation distance to nozzle diameter L/D needs to be aimed at ratios close to 1 [207]. Below this, the flow profile is no longer flat, making it difficult to interpret the achieved data without a flow quantification like particle image velocimetry (PIV).

The diameter of a standard McKenna burner (inner ring) is 60.5 mm. An enlargement of the separation of the two opposed burners ratio of nozzle separation distance to nozzle diameter (L/D) to 0.83 (Figure 5.2) during fundamental testing generated a transient, irregularly shaped, and sooting flame. The physical appearance of these flames indicated the cause of this being a matter of fluid dynamics, rather than chemical reaction, based on a non-uniform gas distribution in the burners, which induces irregular local strain rates [208].

The core components of the newly constructed stainless steel burner set-up are two equivalent burners (Figure 5.3), with an extended axial length of 180 mm in regard to the inner, main gas chamber. The main chamber (left (1)) is also shrouded by a hollow body (left (2)) to induce an additional gaseous flow in the form of a co-flow, as are the McKenna burners. Just above the nozzles of the main gas chambers, a filling of a honeycomb monolith made of ceramics to straighten out and distribute the incoming gas flow begins. The remainings of the inner chambers are filled to capacity with steel wool for similar reasons.

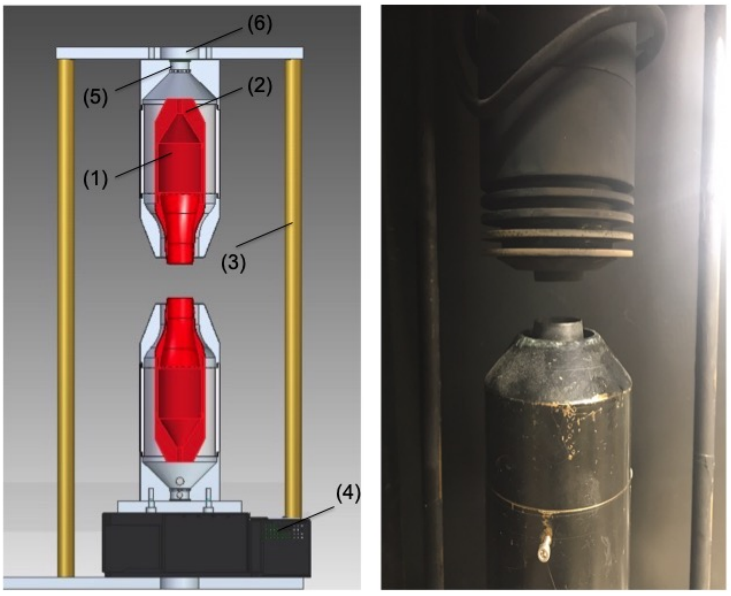

Figure 5.3: *Scheme of (left) and actual constructed (right) counter-flow burner system. (1): inner gas chamber top burner, (2): outer gas chamber top burner, (3): alignment system for top and bottom burners, (4): stage to move bottom burner, (5): gas input top burner, (6): cooling water input top burner.*

With this design of the burner system, a L/D ratio of circa 0.8 was reached during nearly all of the experimental investigations done, leading to laminar diffusion flames. A system of movable and fixed poles (3) enabled an exact axial alignment between the top and bottom burners. Furthermore, a motorized stage (4) made an adjustment to varying L/D for differing experimental conditions possible and precisely exact.

Finally, the top burner was equipped with a fresh water-cooling system (6) due to the hotter surroundings at the top of the measuring cell, where the exhaust fumes gather. A stainless steel cooling coil was wrapped around about 70 % of the top burner, constantly being fed with water at ambient temperature. With these adjustments in technical design and construction of the burner system, the difficulties in exact alignment, top-nozzle to bottom-nozzle distance, and a developed flow of gaseous fuels were overcome.

5.1.2 Nd:YAG laser

A laser (**L**ight **A**mplification by **S**timulated **E**mission of **R**adiation) is said to be just a more complicated and unique flashlight, with energy in the form of electricity entering and light exiting. That this is an understatement will be presented in the

following section [209]. Lasers emit coherent electromagnetic radiation at a defined wavelength at a low divergence. Their wavelengths span from the electromagnetic spectrum of infrared, visible, and ultraviolet up to the x-ray region; their emission yields include continuous wave to extremely large energy or peak-power pulses, ranging from very weak to terawatt power levels. This leads to a large variety of applications in scientific disciplines, material processing, and medical technology [210, 211].

Some of the lasers that are utilized extensively are excimer lasers, liquid lasers like dye lasers, gas lasers like He-Ne, argon ion, and CO_2 lasers, or solid-state lasers like ruby, Nd:glass, and Nd:YAG lasers [211]. The latter technology will be further considered due to the utilization of the spectroscopic techniques applied during this study.

The first Nd:YAG laser was built and operated at Bell Labs in 1964 and has undergone tremendous development since then. This system's flexibility and adaptability make it a widely used tool in many research labs for both fundamental and technical investigations [210]. This makes them the favored of the solid-state lasers. An yttrium aluminum garnet (short YAG) is the host medium; it is a $Y_3Al_5O_{12}$ crystal, where some of the Y^{3+} ions are substituted by Nd^{3+} ions [212].

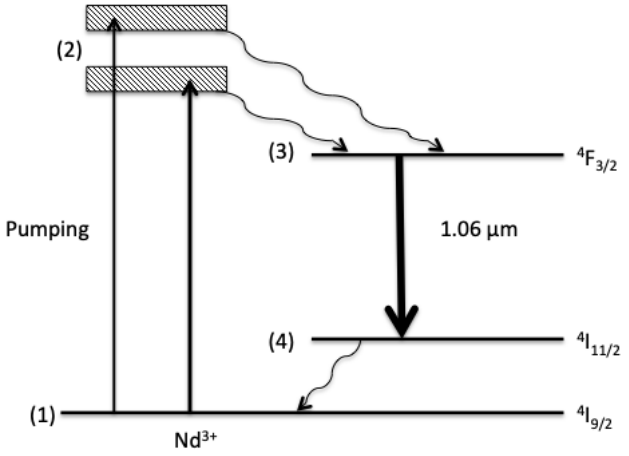

Figure 5.4: *Simplified four-level transition scheme of Nd:YAG energy levels based on [24]*

Figure 5.4 shows the simplified energy level scheme for an Nd:YAG laser arising from the three inner-shell 4f electrons of the Nd^{3+}. The pumping from the ground level (1) arrives at the two predominant absorption pump bands at (2), which lay at $\sim 730\,\text{nm}$ and $800\,\text{nm}$. A nonradiative decay to the $^4F_{3/2}$ level (3), which therefore assembles a large part of the pump power, makes this a potential candidate for the upper level for laser action. Furthermore, the decay to the lower I-levels (4) takes place [212]. The laser action typically occurs from the R_2 level of $^4F_{3/2}$ to a specific

sublevel at $^4I_{11/2}$ with a transition of $\lambda = 1.064\,\mu m$, making this the most frequently used wavelength for Nd:YAG lasers at $\lambda = 1064\,nm$ [212].

Frequency conversion by nonlinear crystals of the fundamental $\lambda = 1064\,nm$ wavelength (infrared) can produce other wavelengths to be emitted by the Nd:YAG laser. Frequency doubling leads to the second-harmonic generation (SHG) at $\lambda = 532\,nm$ (visible light) and those results can be doubled once more to create the fourth-harmonic generation (FHG) at $\lambda = 266\,nm$ (ultraviolet). These wavelengths can also be mixed with the fundamental $\lambda = 1064\,nm$, leading to the third-harmonic generation (THG) at $\lambda = 355\,nm$ (ultraviolet). Further specifications of the Lab-150 Nd:YAG that was used during these investigations can be found in Figure A.6 in appendix A.

5.1.3 Spectroscopic set-up

The central part of the spectroscopic set-up is the pulsed Lab 150-10 Hertz Nd:YAG laser from Spectra Physics (USA), as presented in Section 5.1.2.

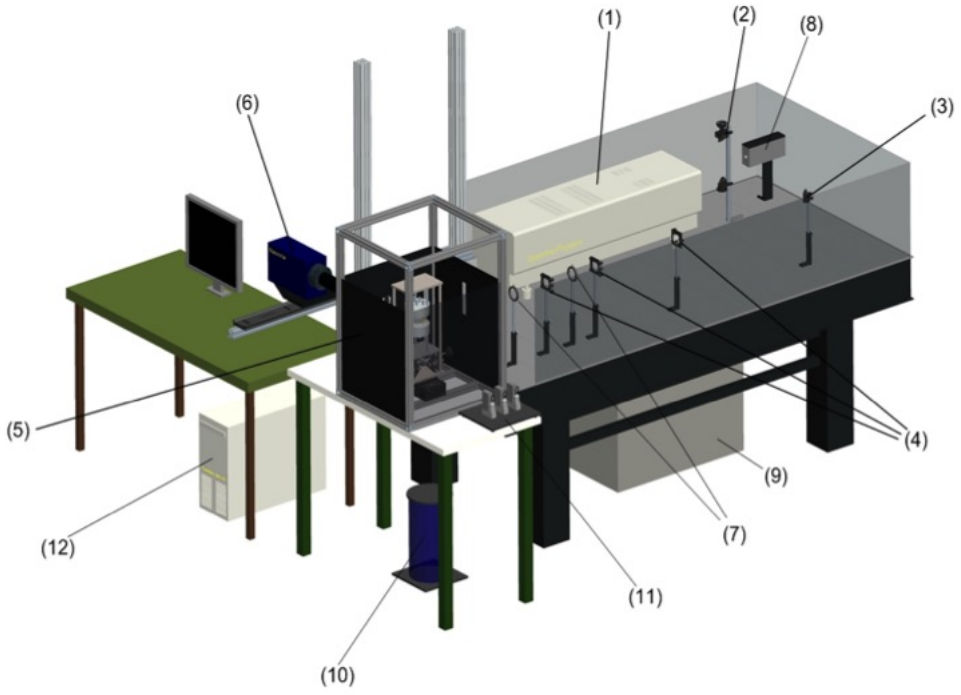

Figure 5.5: *Scheme of spectroscopic set-up. (1): Nd:YAG laser head, (2): periscope, (3): periscope, (4): beam-shaping lenses, (5): counter-flow burner, (6): ICCD camera, (7): apertures, (8): beam dump, (9): power unit Nd:YAG laser, (10): cooling water, (11): mass flow controllers, (12): PTU [23]*

These lasers are based on an oscillator-only system also featuring a pump chamber and dual rod configuration, ensuring an excellent output beam quality. At the wavelength of 1064 nm, the maximum output power that can be reached is 6.5 W, decreasing with shorter wavelengths, as presented in Figure A.6. As seen in Figure 5.5, as a result of its size, the laser head of the Lab 150 Nd:YAG (1) had to be placed on one of the longer sides of the measuring table.

The power unit (including the water cooling system) (9) was placed under the experimental set-up. The communication between the laser and additional elements of the spectroscopic systems is done via a programmable timing unit (PTU) (12) and will be further discussed in Section 5.3.

To investigate these counter-flow flames, a laser sheet was formed. Therefore, numerous optical lenses needed to be installed in a fairly outstretched manner to ultimately have their focal point precisely placed. To ensure a spatial alignment of the laser beam onto the alternate side of the measuring table, a double periscope system ((2), (3)) was installed. Periscopes are optical instruments used to direct the laser beam on a higher or lower level. Crucial herewith was the use of two periscope systems, including four mirrors. This ensured the initial vertical polarization of the emitted light by the laser at the adjusted configuration of the crystals at the measuring point. Mirrors with a degree of reflection of 99 % for the wavelength range 350 − 700 nm were used.

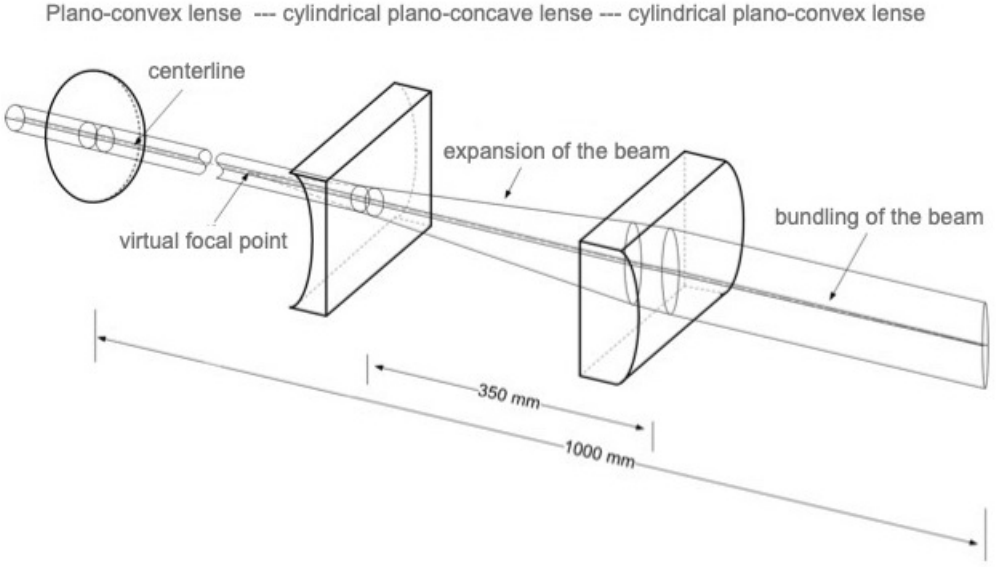

Figure 5.6: *Schematic representation of the arrangement of the optical lenses used for beam widening based on [23]*

The laser beam, now running downstream the experimental table, underwent an expansion into a laser sheet as outlined in Figure 5.6. A system of plano-convex and plano-concave lenses was used to first focus the laser beam on the centerline of the diffusion flame and second, widen it into a sheet.

Following the second periscope, the laser beam enters a round, plano-convex lens. The curved side of the optical element points in the direction of the laser source in order to minimize spherical aberrations [213]. The distance of this first lens corresponds to the focal point of the measurement and, therefore, to the focal length, in this case being 1000 mm. The beam is bundled point-shaped at the target. By transforming the beam into an elongated strip, the laser energy can be introduced into a larger area.

The beam is first widened with the aid of a cylindrical plano-concave optic, followed by a cylindrical converging lens which directs the beam path back to its original shape. Whereas the diameter of the beam going in the vertical direction is being considerably enlarged. The distance between the cylindrical lenses is determined by the focal lengths of these optical elements and their common virtual focal point; the following applies [23]:

$$l_{\text{distance}} = f_1 - |f_2| \tag{5.1}$$

where f_1 = focal length of the converging lens and f_2 = focal length of the diverging lens. For the given experimental set-up, a plano-convex cylindrical lens with a focal length of $f_1 = 500$ mm, as well as a plano-concave optic with $f_2 = -150$ mm were placed so that the distance between the two elements corresponding to equation 5.1.3 adds up to 350 mm. The laser sheet furthermore follows a Gaussian distribution profile, as does the laser beam. In addition to these main components, necessary elements like apertures (7) and beam dump (8) complete the spectroscopic set-up. Diffuse light reflections due to metal surfaces in the laser lights pathway lead to aberrations in the measured signals. This difficulty can be decreased by adding apertures and blocking the surplus, unwanted and disorderly light downstream of the lens system. Every experimental investigation using spectroscopic tools is in need of beam dumps to capture the laser light in a closed system and therefore minimize the risk of injury. Further details about the optical elements that were used during this investigation can be found in Appendix A.

5.1.4 Analytical components

The selection of a suitable camera for a functional and flexible laser diagnostic system must take all intended uses of the test bench into account. The differing spectroscopic methods mentioned in Chapter 4 have high and specific demands in regard to the camera:

- The phenomenon of fluorescence is extremely short-lived and often moves in the time range of several millionths to billionths of a second after the excitation of the species that is to be investigated [214]. Therefore, the camera that records the fluorescence reaction must have very short and highly precise reaction times and needs to be gated.
- The Rayleigh scattering signals and some of the fluorescence of specific fuel mixtures are extremely weak and accordingly difficult to detect. Therefore, the camera must exhibit a high sensitivity and is intensified.
- It must be possible to trigger the camera with the laser since the time intervals between the emission of the laser light and the moment of the camera recording must be defined clearly. This is the only way to ensure a reliable and representative measurement.

All these requirements are met by the LaVision (Germany) Nanostar intensified charge-coupled device ICCD camera. The basic structure and function of such a camera are briefly described with the schematic representation in Figure 5.7.

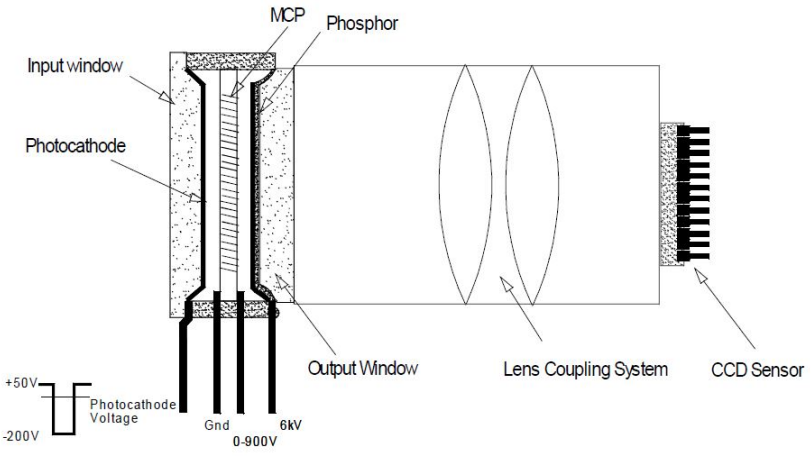

Figure 5.7: *Schematic representation of the technical operation of an ICCD camera [23]*

The captured photons reach the input window of the camera and then the photocathode, generating electrons. With the help of a subsequently attached microchannel plate (MCP), the number of electrons increases drastically, with the extent of the reinforcement, based on the type of construction of the plate and the applied voltage. The Nanostar camera reaches amplifications of up to 1000 [25] and can theoretically achieve a reinforcement of 10^6 when adding further MCP [215]. The increased number of electrons step onto a layer of phosphorus, creating new photons, which are eventually registered by the charge-coupled device (CCD) sensor. This sensor primarily acts as a light-sensitive photodiode. The photons now meet sensitive bitmaps, are absorbed, and generate charge carriers, which are integrated into pixels.

This is followed by the readout phase, in which the charges of the pixels are shifted into buffer memory and are then converted into a voltage with adjustable signal amplification so that the image information can be read out [215]. The initially analog signal is modified via an analog-to-digital converter (ADC) and sent to the PCI interface board. In the last step, the digital data is stored as an image in the buffer of the camera software and thus made accessible to the user of the test rig. The Nanostar ICCD camera is controlled by the software DaVis, which enables the reading, analysis, and processing of data and also allows external control over the laser and energy monitors. This makes it possible to precisely define the time window between a laser light pulse and the collection of photons on the CCD sensor.

Altogether, a number of parameters have to be determined in order to ensure an optimal evaluation of the differing spectroscopic investigations that are carried out, as seen in Table 5.1. In addition to these parameters, the DaVis program also offers numerous possibilities for image postprocessing and evaluation, which will be looked into further in Chapter 5.3.

Table 5.1: *Technical parameters for experimental measurements with an ICCD camera [23]*

Parameter	**Purpose**
CCD Exposure Time	Period of time in which the CCD chip is capable of converting photons into digital signals and thus into images.
Area of Interest	Size of the examination area and thus definition of the sensitive area of the CCD chip.
Delay	Delay until the opening of the amplifying part of the camera, corresponding to the time between the activation of the Q-switch of the laser and the beginning of the collection of photons in the examination area by the camera.
Gate	Period of time during which the amplifying part of the camera converts photons into electrons and amplifies them.
Gain	Adjustment of the voltage strength at the amplification part of the camera and thus determination of the level of amplification of the electrons.
Burst Count	Number of integration and readout steps during the CCD exposure time.

As pictured in Figures 5.5 and 5.8, the ICCD camera is installed behind the counter-flow burner but still attached to the measurement table. With a system of rails, the exact placement of the camera in regard to the focal point can be ensured. In this case, the laser sheet, which proceeds parallel to the camera's lens, cuts through the counter-flow disc-shaped flame. Due to the release of significant heat in the area around the burners, caused by exhaust gases, the ICCD camera and the diverging bandpass filters, etc., need to have a certain distance to the measuring area. This was established by surrounding the counter-flow burner with a metal enclosing, as confined as possible, and additionally by adding intermediate macro rings between the camera and its lens. This distance changes the close-up limit, and the potential magnification increases, making it possible to slide the camera on the rail as far away from the exhaust heat as possible with the existing camera lens.

Significant when using an ICCD camera for differing spectroscopic measurement techniques at different wavelengths are spectroscopic filters. Interference, absorption, or polarization filters, either as long-, short-, or bandpass, can transmit or block a very specified and narrow range of wavelengths. The optics used during these investigations can be found in the equipment list in Appendix A.

As an additional component for the spectroscopic investigations, an energy monitor also by LaVision (Germany) was installed. This instrument is capable of measuring the relative energy of individual laser pulses simultaneously with the light detection. A value for the relative energy is provided, therefore, for each image. With this application, the accuracy of laser imaging increases based on an absolute quantification [216]. The energy monitor can be operated with two measuring heads (4), in this investigation being placed between the aperture (7) and before the burner (5) and after the burner (5) (Figure 5.8). The laser sheet has to run through the energy monitor heads completely in height. The results will be discussed further in Chapter 5.3.

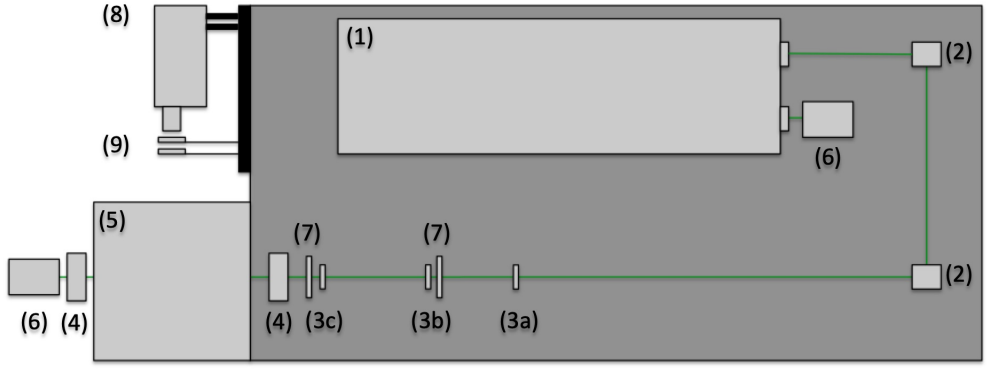

Figure 5.8: *Top view scheme of spectroscopic set-up. (1): Nd:YAG laser head, (2): periscope, (3a-c): beam-shaping lenses, (4): energy monitor, (5): counter-flow burner, (6): beam dump, (7): aperture, (8): ICCD camera, (9): interference / absorption / polarization filters*

To achieve a better overview and elaborate on the triggering process between the parts of the spectroscopic set-up, a top view scheme is presented in Figure 5.8.

A laser beam with a specific wavelength and another beam with mixed (leftover) wavelengths exit the head of the Nd:YAG laser; the positions depend on the arrangement of the nonlinear crystals. In Figure 5.8, the actual emitted beam exits at the top, while the residual radiation from other wavelengths goes straight into a beam dump (6) at the bottom of the head. After exiting, the beam is directed towards the flame with periscopes (2) and shaped into a sheet with the help of optical lenses, as presented in Figure 5.6. (3a) illustrates the plano-convex lens, (3b) the cylindrical plano-concave lens, and (3c) the cylindrical plano-convex lens. To minimize reflexions, apertures (7) are added between the lenses. Before and after passing through the flame in the counter-flow burner system, the laser sheet passes through energy monitor heads (4). An ICCD camera (8) used as a diagnostic system and interference / absorption / polarization filters (9) are also attached to the measurement

table. The attachment is crucial in case vibrations occur. The ICCD camera and Nd:YAG laser are triggered, connected, and controlled by a PTU timing unit. The Nd:YAG used emits bursts of light that are pulsed. After a specific delay, the ICCD camera is internally triggered to take an image. The gate of the camera is opened for a particular time, based on the specific spectroscopic set-up and experiment. The technical parameters for the spectroscopic techniques investigated in this study are presented in Table 5.2.

Table 5.2: *Defining technical parameters of experimental fluorescence, Rayleigh scattering, and chemiluminescence measurements*

Experiment	**Exposure time** $[\mu s]$	**Delay** $[\mu s]$	**Gate** $[\mu s]$	**Gain** $[\%]$
Fluorescence	10.00	0.18	0.30	60.00
Rayleigh scattering	10.00	0.20	0.10	60.00
Chemiluminescence	10.00	/	0.10	30.00

A challenge to be conquered amid this experimental work was the extensive need of partly dangerous gas compositions, especially when not combusted, and up to nine simultaneous inputs per streamline via individual MFC. The detailed fuel mixtures will be discussed further in the following Chapter 5.2.1, but in Figure 5.9, the technical set-up in regard to the fuel blends is outlined.

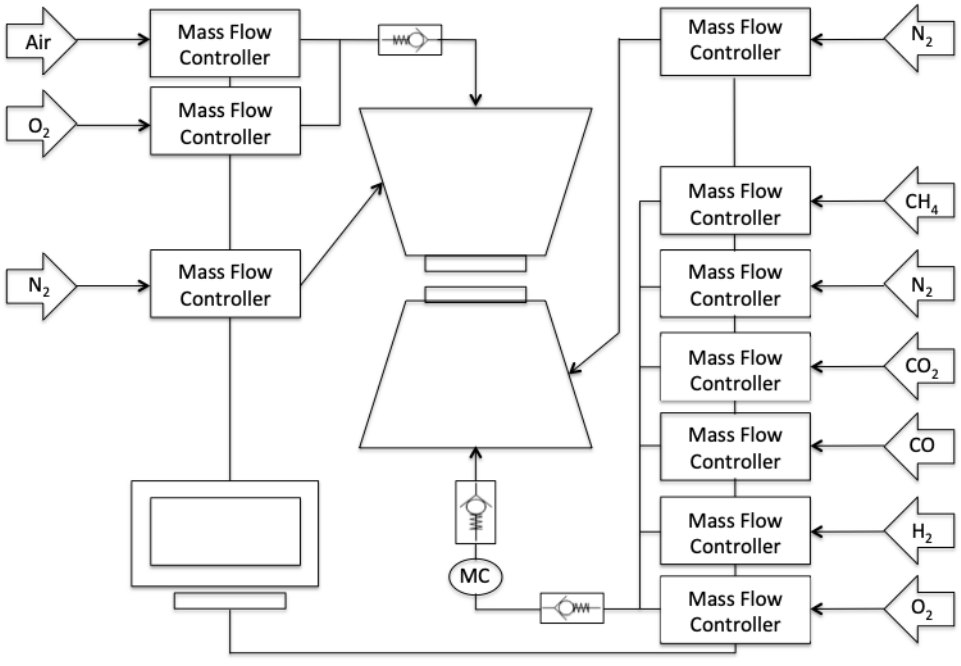

Figure 5.9: *Schematic representation of the burner set-up including gas inputs and mixing chamber (MC), details of the gases used for the experimental work can be found in Appendix A*

Both shroud flows were established by the use of nitrogen, these consistently having the same velocity as the main flows of fuel and oxidizer, to ensure a uniform flow field. To establish a homogeneity among the fuels, first, a distance between the multiple mass flow controllers and the burners had to be established, and second, a mixing chamber (MC) had to be developed. Especially oxygen and hydrogen were partly infused in small quantities; therefore a consistent distribution of the components in the fuel mixture needed to be assured. The mixing chamber measures a length of 10 cm, a diameter of 4.3 cm, and is filled with glass beads of 4 mm diameter.

For safety reasons, multiple external non-return valves were installed before the mixing chamber and before the final entry into the top burner. Every mass flow controller includes an individual internal non-return valve for additional safety. Due to the partial enrichment of the oxidizer air with varying amounts of oxygen during some experimental investigations, an external non-return valve also had to be added before the entrance into the main combustion chamber of the top burner.

All the mass flow controllers were operated by an additional computer unit using the software get red-y by HTK Hamburg (Germany), which was delivered with the MFC. Manual emergency closing valve systems were additionally installed after each individual mass flow controller, as well as behind the mixing chamber. With these fuel blends, the behavior regarding velocities, possible straining out, or dilution effects needed to be absolutely familiar beforehand for various security reasons during the experimental operations.

Not pictured for the sake of clarity are the two rotameters and further appliances and chemicals needed for the flat field imagery when applying laser-induced fluorescence, which were also part of the analytical components. For subsequent data processing, all spectroscopic techniques require flat field correction imaging before and after the combustion imagery. This procedure is standardized for the calibration of images, and the objective is to eliminate artefacts from a picture that are caused by the detector's sensitivity or fixed-pattern noise [217].

5.2 Experimental conditions

The experimental design was carefully developed to account for possible complications during the main investigations. This is based on preliminary studies with diluted methane mixtures at different velocities, with different compositions and varying set-ups. The developed test rig, especially the counter-flow burner, and its potential for unexpected heat development had to be thoroughly examined. Furthermore, spectroscopic techniques and their nuances, technical interaction, analytical synergies, etc., had to be developed and be acquainted with before using explosive and/or toxic fuel compositions. In the following chapters, the fuel mixtures and experimental conditions will be presented.

5.2.1 Fuel mixtures - PG, GGL2, GGL3

Preliminary studies in preparation for the investigations of synthetic biomass-based model fuels were done by using diluted methane mixtures as fuels and air as oxidizer for the experimental work. As diluents, nitrogen and carbon dioxide were chosen, both or at least one generally being a part of products resulting from biomass gasification or pyrolysis processes. An introduction to the use of methane as fuel and the inert gases nitrogen and carbon dioxide as considerable components in BDG has been given in Sections 3.4.1 and 3.4.2.

Especially due to the fact that the counter-flow burner system was an in-house construction, the accuracy of the induced flow fields had to be verified. An uneven or incorrect flow field would indicate incorrect input velocities and, therefore, flawed straining-out behavior when comparing experimental and numerical solutions. The specifications of all the gases used during these investigations can be found in Appendix A.

The goal of verifying not only referenced solutions but also comparing experimental solutions with their numerical counter-part led to the evolution of diluted methane fuels, as seen in Table 5.3. The fuel was replaced gradually and in small steps with either carbon dioxide or nitrogen, while finally leading to a displacement of 25 vol.-% of fuel to diluent when comparing CH4-001-X and CH4-007-X. The latter could experimentally only be achieved with nitrogen as diluent at the investigated velocity due to the straining out of methane flames with more than 68 vol.-% of carbon dioxide at a velocity of 60 cms^{-1} at the distinct burner configurations (like nozzle separation, i.e.) regarded.

Table 5.3: *Investigated diluted methane mixtures; X representing N_2 or CO_2*

	Fuel		**Oxidizer**
Name of methane mixture	**CH_4** [*vol.-%*]	**X(N_2 or CO_2)** [*vol.-%*]	**Air** [*vol.-%*]
CH4-001-X	50	50	100
CH4-002-X	40	60	100
CH4-003-X	37	63	100
CH4-004-X	34	66	100
CH4-005-X	31	69	100
CH4-006-X	28	72	100
CH4-007-X	25	75	100

The influence of oxygen enhancement of fuel or oxidizer on the combustion behavior was already briefly discussed in Section 3.5.2. The impact on these diluted methane mixtures was investigated by adding 5 vol.-% of oxygen to the fuel- and oxidizer sides, with special regard to the formaldehyde evolution in the flame and temperature distributions. These fuel and oxidizer compositions, based on Table 5.3, can be found in Tables 5.4 and 5.5.

Table 5.4: *Investigated diluted methane mixtures enriched with oxygen on the fuel side; X representing N_2 or CO_2*

	Fuel			**Oxidizer**
Name of methane mixture	**CH_4** [*vol.*-%]	**X(N_2 or CO_2)** [*vol.*-%]	**O_2** [*vol.*-%]	**Air** [*vol.*-%]
CH4-001-X-O2-F	47.50	47.50	5.00	100.00
CH4-002-X-O2-F	38.00	57.00	5.00	100.00
CH4-003-X-O2-F	35.15	59.85	5.00	100.00
CH4-004-X-O2-F	32.30	62.70	5.00	100.00
CH4-005-X-O2-F	29.45	65.55	5.00	100.00
CH4-006-X-O2-F	26.60	68.40	5.00	100.00
CH4-007-X-O2-F	23.75	71.25	5.00	100.00

Table 5.5: *Investigated diluted methane mixtures enriched with oxygen on the oxidizer side; X representing N_2 or CO_2*

	Fuel		**Oxidizer**	
Name of methane mixture	**CH_4** [*vol.*-%]	**X(N_2 or CO_2)** [*vol.*-%]	**N_2** [*vol.*-%]	**O_2** [*vol.*-%]
CH4-001-X-O2-A	50.00	50.00	75.05	24.95
CH4-002-X-O2-A	40.00	60.00	75.05	24.95
CH4-003-X-O2-A	37.00	63.00	75.05	24.95
CH4-004-X-O2-A	34.00	66.00	75.05	24.95
CH4-005-X-O2-A	31.00	69.00	75.05	24.95
CH4-006-X-O2-A	28.00	72.00	75.05	24.95
CH4-007-X-O2-A	25.00	75.00	75.05	24.95

Table 5.6: *Investigated basic fuel mixtures from thermochemical conversion processes*

	Fuel						**Oxidizer**
Name of fuel mixture	**CH_4** [*vol.*-%]	**N_2** [*vol.*-%]	**CO_2** [*vol.*-%]	**CO** [*vol.*-%]	**H_2** [*vol.*-%]	**LHV** [MJ/m^3]	**Air** [*vol.*-%]
GGL2	4.80	1.50	28.90	37.60	27.20	9.48	100.00
GGL3	1.60	61.00	7.90	24.50	5.00	4.23	100.00
PG	10.00	0	35.00	50.00	5.00	10.49	100.00

The fuel mixtures based on the thermochemical conversion processes gasification and pyrolysis can be found in Table 5.6. GGL2 is based on a gasification process with pine wood as biomass, with oxygen and steam as gasification agents. GGL3, on the other hand, is based on gasification with air as gasifying agent and PG induced via a pyrolysis process of woody biomass. For the primary investigations air has been utilized as oxidizer, being induced at the same velocity as the fuel for every experimental study.

Furthermore, as has been done during the preliminary investigations with diluted methane mixtures, oxygen was added to the fuel- and also to the air-sides respectively; leading to the compositions presented in Tables 5.7 and 5.8.

Table 5.7: *Investigated fuel-oxidizer mixtures enriched with oxygen on the fuel side*

	Fuel						**Oxidizer**
Name of fuel-oxidizer mixture	**CH_4** [*vol.*-%]	**N_2** [*vol.*-%]	**CO_2** [*vol.*-%]	**CO** [*vol.*-%]	**H_2** [*vol.*-%]	**O_2** [*vol.*-%]	**Air** [*vol.*-%]
GGL2-2.5-O2-F	4.68	1.46	28.18	36.66	26.52	2.50	100.00
GGL2-5-O2-F	4.56	1.43	27.45	35.72	25.84	5.00	100.00
GGL2-8.5-O2-F	4.39	1.37	26.44	34.41	24.89	8.50	100.00
GGL3-2.5-O2-F	1.56	59.47	7.70	23.89	4.88	2.50	100.00
GGL3-5-O2-F	1.52	57.95	7.50	23.28	4.75	5.00	100.00
GGL3-8.5-O2-F	1.46	55.81	7.23	22.42	4.58	8.50	100.00
PG-2.5-O2-F	9.75	0	34.13	48.75	4.88	2.50	100.00
PG-5-O2-F	9.50	0	33.25	47.50	4.75	5	100.00
PG-8.5-O2-F	9.15	0	32.02	45.75	4.58	8.50	100.00

Table 5.8: *Investigated fuel-oxidizer mixtures enriched with oxygen on the oxidizer side*

	Oxidizer		**Fuel**
Name of fuel-oxidizer mixture	**N_2** [*vol.*-%]	**O_2** [*vol.*-%]	Compositions as presented in Table 5.6
GGL2-2.5-O2-A, GGL3-2.5-O2-A, PG-2.5-O2-A	77.03	22.97	-
GGL2-5-O2-A, GGL3-5-O2-A, PG-5-O2-A	75.05	24.95	-
GGL2-8.5-O2-A, GGL3-8.5-O2-A, PG-8.5-O2-A	72.28	27.72	-

5.2.2 Strain rates - Velocities and straining out

For the experimental investigation the fuel and oxidizer velocities 30 cms^{-1}, 60 cms^{-1}, and 100 cms^{-1} were chosen for the BDG. For the counter-flow burner that was built, with the fuels investigated at 30 cms^{-1}, the first semi-stable flames could be induced. Velocities of 100 cms^{-1} led to very stable flames that were still far enough away from straining out for all the considered compositions.
For the dimension of the utilized burner system (Section 5.1.1), a strain out for PG would be induced at about 443 cms^{-1}, for GGL3 at 148 cms^{-1}, and for GGL2 at around 2200 cms^{-1} due to the high amount of hydrogen present. An experimental examination closer to strain out was not possible due to the laboratories technical set-up in regard to the gas supply.

All the velocities and strain rates for the regarded compositions can be found in the Appendix in Tables A.1 and A.2. The strain rates were calculated using Equation 3.17, the strain outs were determined via numerical solutions from DIFFLA.

5.3 Data processing

The processing for all of the spectroscopic data was preliminarily done with the Davis Software, which is provided by LaVision (Germany) as a product for intelligent laser imaging. This tool can be applied for imaging purposes, amongst other things, in the fields of combustion, spray applications, and fluid dynamics in combination with high-performance cameras. Being equipped with an ICCD camera and additionally an energy monitor system all from LaVision, an unrestricted use

of DaVis's possibilities can be established with the current experimental test rig. DaVis is set-up as a modular system, enabling an overall operation on a basic level or, if necessary, applying the benefits of specific spectroscopic needs when added as an upgrade package. Furthermore, the software itself can integrate most of the experimental hardware and their regulations (such as, i.e., triggering) in one analysis concept. A core functionality of DaVis is the processing work that can be done to the raw experimental images collected. Usually collected in a bundle of hundreds of unprocessed data, most prominent issues like artefacts as laser intensity gradients and background noise can be eliminated or at least diminished. The hundreds of raw experimental images are averaged to one raw data image to reduce random noise. By combining images taken at different stages or applying filters, the desired physical representation of the experimental work can be achieved and is constituted in intensity counts [216].

For the LIF and Rayleigh measurements, one experimental run-through began and ended with a flat field image as previously mentioned in Section 5.1.4. The concept of flat fielding (spectroscopic) images is a way to calibrate experimental results generated by cameras. Variations in pixel-to-pixel comparisons due to a slightly different quantum efficiency or marginally different gain can be removed by the use of flat field images by flattening the relative response for each pixel to the approaching radiation. A good and valuable flat field should be taken with the exact filters and lenses that will be needed for the experimental investigations and also illuminated by a strong light source, making it much brighter than the experimental image that will be observed. This results in a calibration image of high signal-to-noise ratio while not saturating the ICCD. The primary aspect of this projector flat field imaging is to remove the variations from pixel-to-pixel, but also to compensate optical fringes, vignetting, dust accumulation, or any other artefacts within the optical path. As usual, when producing calibration images, 500 images were taken and averaged to generate the final calibration images before and after each experimental run-through [218].

For the LIF experiments, a 37 % formaldehyde in water solution (Carl Roth, Germany) was diluted with nitrogen and pushed through a thoroughly investigated flat-fielding device while excited at 355 nm with the Nd-YAG laser. In preliminary investigations, problems of contaminated burner nozzles due to liquid droplets and condensation of formaldehyde occurred, which led to the decision of an external ap-

paratus. This device was carefully inserted sideways between the top and bottom nozzles of the burner to flood the measurement area while not disturbing the course of the laser beam and induce camera reflections. The volume flow of formaldehyde and nitrogen was kept steady at volume flows of $1.5\,\mathrm{l\,min^{-1}}$ and $2\,\mathrm{l\,min^{-1}}$, respectively, for all the experimental investigations that were conducted and regulated via rotameters.

For the Rayleigh experiments, a constant flow of air was inserted into the top nozzle and the Rayleigh scattering excited at 532 nm of the air was used for flat fielding purposes. For the CH* chemiluminescence experiments, it was abstained from flat fielding, among other things, due to the missing application of a spectroscopic excitement source.

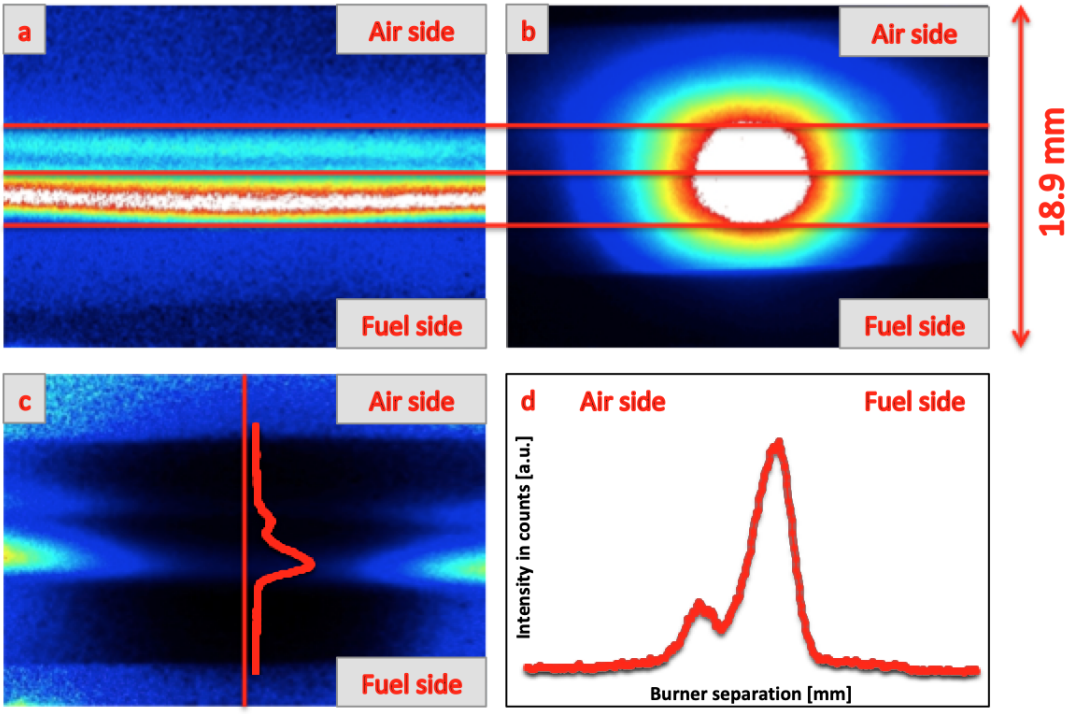

Figure 5.10: *Diffusion flame (a) excited at 355 nm with fuel (PG-5-O2-F-100) coming from the top and oxidizer (air) from the bottom nozzle at a velocity of $30\,cms^{-1}$, formaldehyde flat fielding image (b), flat fielded diffusion flame (c) with centerline from bottom to top nozzle and formaldehyde signal (d) all at a burner separation distance of 18.9 mm. An increase of intensity is represented by the color change of dark blue, to blue, to green, to yellow, to red, to white.*

In Figure 5.10, the data processing procedure for fluorescence measurements is elucidated step by step. Before and after a diffusion flame image (a), the previously discussed flat fielding images (b) are obtained and averaged. The laser sheet is Gaussian in shape, achieving the highest excitation and therefore intensities in the center between top and bottom nozzle, colored white in Figure 5.10.

It is crucial to place this peak of power in the physical position where the formaldehyde develops in the flame, as can be seen via the red lines placed within images (a) and (b). Secondly, the placement of the flat field needs to be precisely centered around the vertical centerline, this being the area of interest in comparison to the numerical data. In the next step, the two flat field images are averaged, and the diffusion flame was divided by these ((a)/(b)) leading to image (c). The intensity in counts measured alongside the centerline of the processed diffusion flame leads to the preliminarily measured formaldehyde peak plotted against the burner separation (d), this being 18.9 mm for all the cases discussed.

The laser sheet is approximately 10 mm wide, thus making the intensity curves 4.45 mm directly next to each nozzle irrelevant. All images are corrected by the use of an energy monitor, as discussed in Chapter 5.1.4.

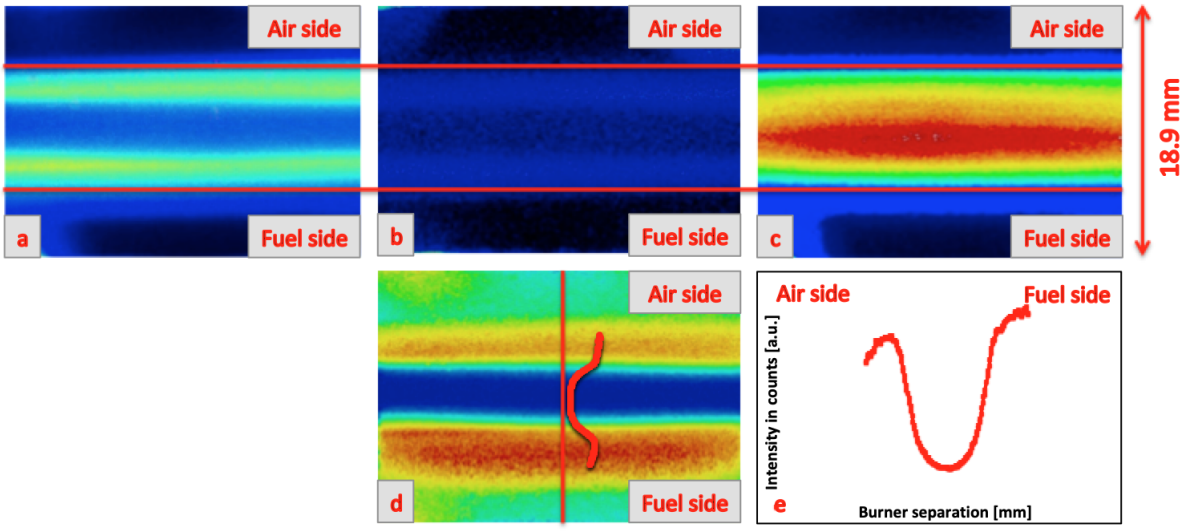

Figure 5.11: *Polarized diffusion flame (a) excited at 532 nm with fuel (GGL3-2.5-O2-F) coming from the top and oxidizer (air) from the bottom nozzle at a velocity of 60 cms^{-1}, depolarized diffusion flame (b) air flat fielding image (c), flat fielded diffusion flame (d) with centerline from bottom to top nozzle and Rayleigh signal (e) all at a burner separation distance of 18.9 mm. An increase of intensity is represented by the color change of dark blue, to blue, to green, to yellow, to red, to white.*

Accordingly, the data processing procedure for Rayleigh measurements is presented in Figure 5.11. As already introduced above, for the LIF experiments, flat field images (c) are being shot before and after the images of the diffusion flame ((a) and (b)) under investigation. Since air has a strong Rayleigh scattering signal, it can be used for flat fielding by introducing a constant flow through one of the nozzles. Due to the polarized (a) and depolarized (b) Rayleigh scattering, as presented in Section 4.2, two averaged sets of images of the diffusion flame have to be shot consecutively. The depolarized scattering (b) has to be subtracted from the polarized scattering

(a), before it is divided by the two averaged flat field (c) images from before and after. This leads to a corrected polarized Rayleigh scattering signal solely from the examined flame (d). The scattering intensity is again measured along the vertical centerline leading from the top to bottom nozzle and also plotted against the burner separation in 18.9 mm (e). Finally, all images taken were once again corrected by the use of an energy monitor.

Due to the strong temperature dependence of the formaldehyde partition function, a Boltzmann correction, as it was implemented in [26], was applied to the experimental LIF data after the previously mentioned procedure.

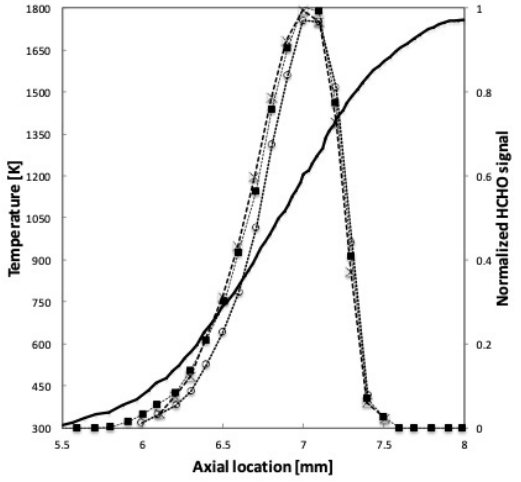

Figure 5.12: *The solid line represents the temperature distribution and normalized formaldehyde profiles in a $CH_4 - O_2$ counterflow and nitrogen diluted diffusion flame. Solid squares represent the raw, uncorrected profiles and correlate with profiles corrected with the assumption $Q_{12} \sim T^{-1}$ (represented by the cross) and the assumption $Q_{12} \sim T^{-0.5}$ (represented by the open circle). The thickness of the formaldehyde zone is characterized as FWHM (full width half maximum). Based on [26]*

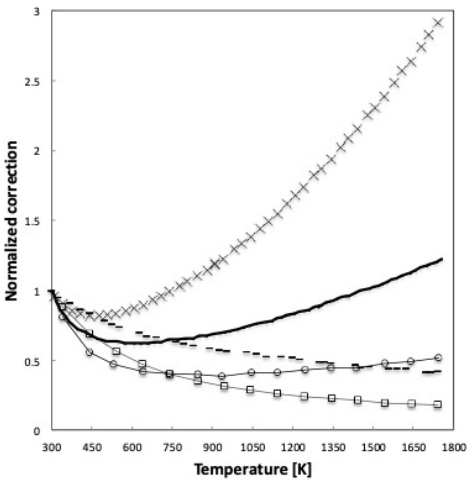

Figure 5.13: *Normalized with respect to their value at $T = 300\,K$ correction coefficients were applied as a function of T, with the cross representing a correction due to the temperature dependence of the partition function; the dashed line representing a quenching correction assuming $Q_{12} \sim T^{-0.5}$, the solid line representing a total correction assuming $Q_{12} \sim T^{-0.5}$, the open square representing a quenching correction assuming $Q_{12} \sim T^{-1}$ and the total correction assuming $Q_{12} \sim T^{-1}$. Based on [26]*

As shown in Figure 5.12, the main quantity of formaldehyde forms in the lower temperature region of the diffusion flame, as described here being between $700 - 1300$ K. At higher temperatures, 1800 K and increasing, a minimum Boltzmann correction factor of three is necessary to process the experimental data correctly. For the interpolation of the experimental data, a correction coefficient (*cross*) as a function of T normalized corresponding to their value at T = 300 K as seen in Figure 5.13 was applied [26].

Chapter 6

Numerical investigations

The numerical investigations that were performed during this study are entirely based on a model simulating one-dimensional counter-flow DIFfusion FLAmes named DIFFLA, which will be presented in the following chapter. To support the evaluation processes of the experimental solutions, further programs, namely CHFIT and RAYFIT, were developed in-house and will also be discussed shortly.

6.1 DIFFLA

The Fortran 77 code DIFFLA was first developed by Frank Behrendt and Jürgen Warnatz at the University of Heidelberg in Germany in 1989. The impact of different fuel compositions, fuel or oxidizer velocities, temperatures, and further operating conditions on stationary laminar diffusion flames can be derived from this modelling code solving the governing equations for momentum, mass fraction, and energy [219]. This code can be used to numerically describe either premixed or non-premixed combustion in counter-flow flames. The experimental work for this thesis was done for comparison and validation of the DIFFLA code, which was not adapted for these purposes.

6.1.1 Introduction to DIFFLA and comparable models

The program itself consists of two main modular parts, each composed of numerous sub-routines; these enable the handling of sub-problems in the corresponding sub-routine. Sub-programs, i.e., for analysing the reaction mechanism or for the determination of the transport variables, can therefore be taken from other program packages. This procedure reduces the number of possible sources of error [220].

The first main program provides information from various files about the system that is to be numerically represented, which is then transferred to the second main program (*integrator*) by means of a temporary file. The first program reads in the *INPUT* file, listing the species present in the system, the boundary conditions of the integration, and a set of options that control the integration file. The *MOLNEW* file provides the molecular data of the species and *THERMO* their thermochemical data. Finally, the reaction mechanism is presented in the *MECH* file. The imported data and files are checked for consistency. If inconsistencies occur, the program responds with corresponding error messages and terminates [220].

Table 6.1: *Considered species in the combustion model DIFFLA [220, 221]*

H_2/O_2/ CO/CO_2-systems	**C_1-system**	**C_2-system**	**C_3-system**	**C_4-system**	**NO-system**
H	C	C_2H	C_3H_2	C_4H_2	N
H_2	CH	C_2H_2	C_3H_3	C_4H_6	N_2
O	$^1CH_2$	C_2H_3	C_3H_4	n-C_4H_7	NH
O_2	$^3CH_2$	C_2H_4	C_3H_5	i-C_4H_7	NH_2
OH	CH_3	C_2H_5	C_3H_6	1-C_4H_8	NH_3
HO_2	CH_4	C_2H_6	n-C_3H_7	2-C_4H_8	NO
H_2O	CHO	HCCO	i-C_3H_7	c-2-C_4H_8	NO_2
H_2O_2	CH_2O	CH_2CO	C_3H_8	i-C_4H_8	N_2O
CO	CH_2OH	CH_3CO		i-C_4H_9	N_2H
CO_2	CH_3O	CH_2CHO		p-C_4H_9	CN
	CH_3OH	CH_3CHO		s-C_4H_9	C_2N_2
	CH_3O_2	C_2H_5OH		t-C_4H_9	HCN
	CH_3O_2H	C_2H_5O		C_4H_{10}	H_2CN
		CH_3CHOH		i-C_4H_{10}	HNO
		CH_2CH_2OH			HNO_2
					CNO
					HCNO
					HOCN
					HNCO
					Ar

The thermal conductivity, diffusion, and toughness of individual species, their specific heat, and enthalpies are determined from the feeding-in of coefficients and

molecular parameters. By means of an adjustment calculation, polynomials are fit to the calculated values. These values are furthermore transferred to a temporary intermediate data file. This file also includes a species-reaction-matrix regarding the species involved in a specific reaction [220].

To solve combustion simulations of these premixed or non-premixed counter-flow flames, 80 different chemical species, molecules, and radicals, are taken into account (Table 6.1).

Finally, the second main program, the *integrator*, solves the modelling process by reading in the temporary intermediate file, using these contained data to carry out the integration of the conservation equations. The information is distinct for every flame.

In cases where particle or temperature profiles from previous calculations are not yet available for specific flames, the integration starts with arbitrary but wisely chosen beginning profiles. Otherwise, previous calculations can be continued by taking their start profiles from a file named $OUTPUT$ [220].

As the integration progresses, profiles of the desired stationary flame are provided. Whether a stationary solution is reasonable depends on the behavior of some of the profiles when regarding the last 50 to 100 integration steps. Here, particular attention is given to the temperature profile and that of hydrogen atoms since both are quite sensitive to indicate the progress when achieving a stationary solution [220].

After a defined number of integration steps, the profiles obtained up to this point are stored in the $OUTPUT$ file. A continuation of the integration can be carried out using this file, as previously mentioned. This technique allows for more time-consuming integrations to be distributed over several program runs. Also, herewith it is possible to use previously run solutions for integrations of flames, which differ only slightly in their boundary conditions [220].

The development of fast and powerful personal computers and, furthermore, the increased availability of thermochemical and kinetic combustion data, lead to various numerical modelling systems. The following represent alternatives for laminar premixed and non-premixed numerical modelling [222]:

- *PREMIX*: developed at Sandia National Laboratories, a Fortran code modelling steady laminar one-dimensional premixed flames
- *RUN-1DL*: developed in Cambridge, a Fortran code modelling steady laminar one-dimensional and also quasi-one-dimensional premixed, unstrained, strained, diffusion, partially premixed, two-phase flames, i.e.
- *COSILAB*: developed from the *RUN-1DL* code, simulating multiple flames such as unstrained, premixed, diffusion, partially premixed flames, i.e.
- *FlameMaster*: developed at RWTH Aachen University, computing 0D and 1D laminar flames
- *OPPDIF*: developed at Sandia National Laboratories, a Fortran code computing counter-flow diffusion flames
- *CHEMKIN-II*: developed at Sandia National Laboratories, intended for chemical kinetics simulations, evolved from CHEMKIN-PRO

6.1.2 Governing equations

The modelling and simulation of combustion processes via numerical models offers the opportunity to study flames that are challenging to induce experimentally and also to validate simulated with experimental results and vice versa. The description of a reactive flow with the help of a simulation program requires the ability to describe the governing equations that control the process. As previously mentioned, this incorporates the following [220, 221]:

- The conservation of mass - the continuity equation
- The conservation of momentum - the motion equation
- The conservation of energy - the energy equation
- The conservation of chemical species - the conservation of chemical species equation

The flow of a fluid can be described by the conservation of mass, momentum, and additionally as an equation of state. For the counter-flow flames considered, the ideal gas law (Equation 4.13) can function as an equation of state with sufficient precision when regarding the link between temperature, pressure, and density.
Conservation equations were made in the first half of the 19^{th} century by Navier, Poisson, St. Venant, and Stokes, while all these were basically only describing isothermal flows of constant density. Finally, when investigating reactive flows, the conservation of energy and mass in the system have to be included in the numerical simulation. Especially the transition from isothermal to reactive flows can increase the complexity of the model considerably, leading to the need for approximations [220, 221].

The previously introduced conservation equations for fluids describing combustion processes, and therefore the induced numerical model, are in need of some assumptions [220, 221, 223]:

- Classical mechanics are used to describe the impacts and general movement of the atoms and molecules in the flame during the combustion process. Quantum effects can be neglected due to the low pressure and high temperatures.
- The fluid can be considered continuous due to the mean free path of the atoms and molecules being substantially smaller than the gradients of their velocity, temperature, density, and concentrations.
- Under the pressure prevailing in the system, only two but not three impacts of atoms or molecules are to be expected.
- The collisions of the atoms and molecules in the flame can be regarded as predominantly elastic, therefore conserving the kinetic energy and not changing the internal degrees of freedom.
- The bulk viscosity for gases at low pressure, electromagnetic fields, gravitation, buoyancy, energy flux due to a mass concentration gradient, the viscous dissipation term during the conservation of energy, and the heat transport due to thermal radiation are all neglected.

6.1.3 Boundary layer assumptions, equations, and conditions

To reduce the numerical simulation to one dimension and also specify the strain field, the flame structure is simplified by employing boundary layer assumptions

and by presuming an outer potential flow [224]. The approximation by Prandtl says that the flow in the proximity of an object can be subdivided into two areas, mainly influencing the viscosity of this flow. Inside the boundary layer, drag is created and the viscosity is dominant; outside of the boundary layer, the viscosity can be neglected [221]. These assumptions via the Prandtl approximation lead to the following consequences [221, 224]:

- The temperature T, density ρ, mass fractions of species i w_i, and the transport coefficients are solely functions of the radial coordinate y.
- The tangential velocity u is modified linearly with x.
- The radial velocity v is solely a function of y.
- The thermodynamic pressure p is granted constant in the flowing field.

The general boundary layer assumptions have been altered (more details in [220]) to be used for a Tsuji counter-flow configuration as presented in 3.2,

leading to the following relations [224]:

Continuity:

$$\rho v = (\rho v)_w - \int_0^y \rho G dy \tag{6.1}$$

Momentum:

$$\frac{\delta G}{\delta t} = \frac{1}{\rho}\frac{\delta}{\delta y}\left(\mu \frac{\delta G}{\delta y}\right) - \frac{\delta G}{\delta y} - G^2 - \frac{H}{\rho} \tag{6.2}$$

Temperature:

$$\begin{aligned}\frac{\delta T}{\delta t} = \frac{1}{\rho c_p}\frac{\delta}{\delta y}\left(\lambda_b \frac{\delta G}{\delta y}\right) - v\frac{\delta T}{\delta y} - \\ \frac{1}{\rho c_p}\sum_i c_{p,i} j_i \frac{\delta T}{\delta y} - \frac{1}{\rho c_p}\sum_i h_i r_{di}\end{aligned} \tag{6.3}$$

Mass of species i:

$$\begin{aligned}\frac{\delta w_i}{\delta t} = \frac{1}{\rho}\frac{\delta}{\delta y}\left({D_i}^m \frac{\delta w_i}{\delta y}\right) - v\frac{\delta w_i}{\delta y} + \\ \frac{1}{\rho}\frac{\delta}{\delta y}\left({D_i}^T \frac{\delta ln T}{\delta y}\right) + \frac{r_{di}}{\rho}\end{aligned} \tag{6.4}$$

with t as time, v as the flow velocity in y-direction, y as the cartesian space coordinates, p as pressure, H and G es eigenvalues, μ as the dynamic viscosity, c_p as the specific heat capacity, λ_b as the heat conductivity, r_{di} as the mass scale chemical rate of formation, j_i as the diffusive mass flux, D_i^m as the modified binary diffusion coefficient, D_i^T as the thermodiffusion and the index i representing the i^{th} species of the system [224].

The boundary conditions at y = 0, the cylinder surface wall, can be presented as follows [224]:

$$\rho v(0) = (\rho v)_w \tag{6.5}$$

$$G(0) = 0 \tag{6.6}$$

$$T(0) = T_w \tag{6.7}$$

$$w_i(0) = w_{i,u} - \frac{j_{i,w}}{(\rho v)_w} \tag{6.8}$$

Mass fractions for hydrogen atoms experience a recombination at the wall surface, leading to differing conditions, with w denoting the environment at the cylinder and u denoting the conditions of the unburnt gas [224]:

$$w_H(0) = 0 \; and \; w_{H_2}(0) = w_{H_{2,u}} - \frac{j_{H_{2,w}}}{(\rho v)_w} - \frac{j_{H,w}}{(\rho v)_w} \tag{6.9}$$

The boundary conditions at $y = y_e$, the outer edge of the flame, are as follows [224]:

$$\frac{\delta G}{\delta y} = 0 \tag{6.10}$$

$$T = T_e \tag{6.11}$$

$$w_i = w_{i,e} \; i = 1, 2, ..., N \tag{6.12}$$

with e denoting the up-streaming gas.

6.1.4 Transport and thermodynamic data, reaction mechanisms

To solve all the equations from Sections 6.1.2 and 6.1.3, including the species previously mentioned in Table 6.1, thermodynamic and transport data, as well as reaction mechanisms, need to be determined.
The macroscopic transport processes and properties can be traced back to microscopic, especially molecular processes, by the kinetic theory of diluted gases. Limitations that restrict or determine the intermolecular interaction lead to expressions for diffusion, coefficients of thermal conductivity, and viscosity, describing the transport processes during the combustion. Detailed derivations can be found in [220].

With the transport data listed in [221], the previously mentioned mixture diffusion coefficients $D_{i,m}$, the thermal diffusion coefficients ${D_i}^T$, the thermal conductivity λ_b, and the viscosity μ can be calculated for the i^{th} species as follows [220]:

$$D_{i,m} = \frac{1 - w_i}{\sum_{j \neq i} \frac{x_j}{D_{i,j}}} \tag{6.13}$$

$$D_i^T = k_i^T \frac{c^2 M_i M_j}{\rho} D_{i,j} \tag{6.14}$$

$$\lambda_b = \frac{1}{2}\left\{ \sum_i x_i \lambda_b i + \left(\sum_i \frac{x_i}{\lambda_b i} \right)^{-1} \right\} \tag{6.15}$$

$$\mu = \frac{1}{2}\left\{ \sum_i x_i \mu_i + \left(\sum_i \frac{x_i}{\mu_i} \right)^{-1} \right\} \tag{6.16}$$

with k_i as the thermal diffusion ratio, M_i as the molar mass of the i^{th} particle, and M_j as the mean molar mass of the mixture in which a particle with the mass M_i diffuses into.

Thermodynamic parameters like the absolute enthalpies $h_i(T)$, the absolute entropies $s_i(T)$, and specific heat capacities $c_{p,i}(T)$ at a given temperature T are in need of known reference values at a standard temperature of $T_0 = 25°C$ and a standard pressure of $p_0 = 1\,\text{bar}$ and represented as polynomial fits. These have been multiply tabulated and were in use when establishing the program code DIFFLA for a temperature range of 300 K to 5000 K [220].

They can be represented as follows [220]:

$$h_i(T) = h^0_{i,T^0} + \int_{T^0}^{T} c_{p,i}(T)dT \tag{6.17}$$

$$s_i(T,P) = s^0_{i,T^0} + \int_{T^0}^{T} \frac{c_{p,i}(T)}{T}dT + \int_{p^0}^{p} \frac{R}{pM_i}dp \tag{6.18}$$

$$c_{p,i}(T) = a_1 + a_2T + a_3T^2 + a_4T^3 + a_5T^4 \tag{6.19}$$

with R as the universal gas constant.

The reaction mechanism of the combustion can be presented by a set of elementary reactions of the involved atoms and molecules to describe the participating chemical processes. The mechanisms involved in the program code DIFFLA can be divided into H_2, O_2, CO and CO_2 systems, the C_1 - C_4 hydrocarbon oxidation mechanisms, the CH_3OH mechanism, and the NO mechanism which can all be found in detail in [220] and [221]. If kinetic parameters were not available, reverse reactions are not included, but instead, they are computed by numerical simulation via the reaction equilibrium constant [220, 221].

In general, elementary reactions can be presented as follows [220]:

$$\sum_{i=1}^{N_E} v'_{r_i} A_i \rightarrow \sum_{i=1}^{N_E} v''_{r_i} A_i \; with \; r = 1, ..., E \tag{6.20}$$

with $v'_{r,i}$ and $v''_{r,i}$ as the stoichiometric coefficients of the i^{th} species of the r^{rd} reaction of the mechanism and r_i as the specific rate of formation of the i^{th} species.

The specific rate of formation r_i can be presented as follows [220]:

$$r_i = M_i \sum_{r=1}^{Y} (v'_{r_i} - v''_{r_i}) k_r \prod_{j=1}^{J} {c_j}^{v'_{r_j}} \; with \; r = 1, ..., F \tag{6.21}$$

The reaction rate coefficients k_r can be presented as follows [220]:

$$k_r(T) = A_r T^{b_r} exp\left(\frac{-E^r_a}{RT}\right) \tag{6.22}$$

with A_r as the collision factor, b_r as the temperature exponent, and E^r_a as the activation energy of the r^{rd} reaction. If k^{-1}_r for the reverse reaction is not available

the principle of microscopic reversibility, based on k_r of the initial reaction and the equilibrium constant K^c_r, can be applied as follows [220]:

$$K_r^c(T) = \frac{k_r}{k_r^{-1}} \tag{6.23}$$

K^c_r can be calculated based on the change in free enthalpy $G^0_{r,f}$ as follows [220]:

$$K_r^c(T) = \left(\frac{P}{RT}\right)^{\sum_i v'_{r_i} - v''_{r_i}} exp\left(\frac{-G^0_{r,f}}{RT}\right) \tag{6.24}$$

All further information in regard to the DIFFLA model, such as mechanisms and reactions, can be found here [220].

6.2 CHFIT and RAYFIT

The numerical data treatment programs *CHFIT* and *RAYFIT* are designed to input numerical data from *DIFFLA* to fit experimental CH* and CH_2O fluorescence data and polarized and depolarized Rayleigh data from counter-flow diffusion combustion. These tools were developed in-house for comparison and validation reasons of experimental and numerical data sets. The main purposes are the detection of the difference in flame location between the modelled and experimentally obtained results and, furthermore, the comparability between the sets of data from the applied spectroscopic techniques.

Both programs require the following subroutines:

- *SPLINE and SPLINT*: these routines calculate a SPLINE through six data points around the target point, where the abscissa is then returned by SPLINT for a given ordinate.
- *FIT*: this subroutine determines the scale and offset on the magnitude axis and furthermore returns the difference in value between the modelled and the experimental data.

Before *CHFIT* and *RAYFIT* read in their *INPUT* file, the provided experimental file must be pre-processed. The experimental file results from the DaVis program (as previously described in Chapter 5) in a matrix of 1024 rows by 1280 columns, with each point representing a value of intensity in counts of a pixel for the two-dimensional image of a flame.

The goal of the pre-processing program is to find the centerline between top and bottom burners in the amount of 1024 x 1280 image pixels. To achieve this, the pre-processing file has to be fed with the exact physical locations of the top and bottom burner center points, of the laser sheet edges, and background positions in pixel quantities. The outcome is the centerline of the experimental result, which can now be directly compared to the *DIFFLA* numerical output files. The number of grid points of the numerical data needs to be greater than the number of grid points of the experimental data.

The simplest possibility to discretise a differential equation is via grid points that have constant distances between them. However, areas of large gradients for the temperature and concentrations of species can develop due to the rapid change the counter-flow diffusion flames investigated undergo during the combustion. The spatial resolution of such gradients requires the densest possible sequence of grid points. Otherwise, there are also areas of low or no activity in the flames, especially close to the nozzles, where there is only unburned, fresh gas to be found. The grid points can be much further apart than in the previously mentioned areas due to the extremely small gradients for T and the species concentrations. Therefore, an equidistant grid with sufficiently small grid point spacing to resolve large gradients would require too many grid points over the entire measuring area. Using grids that are not equidistant can lead to much shorter computing times for the model. By reducing the grid point spacing at locations of large gradients of the temperature or species profile, higher resolution is achieved, compared to locations of smaller gradients [220].

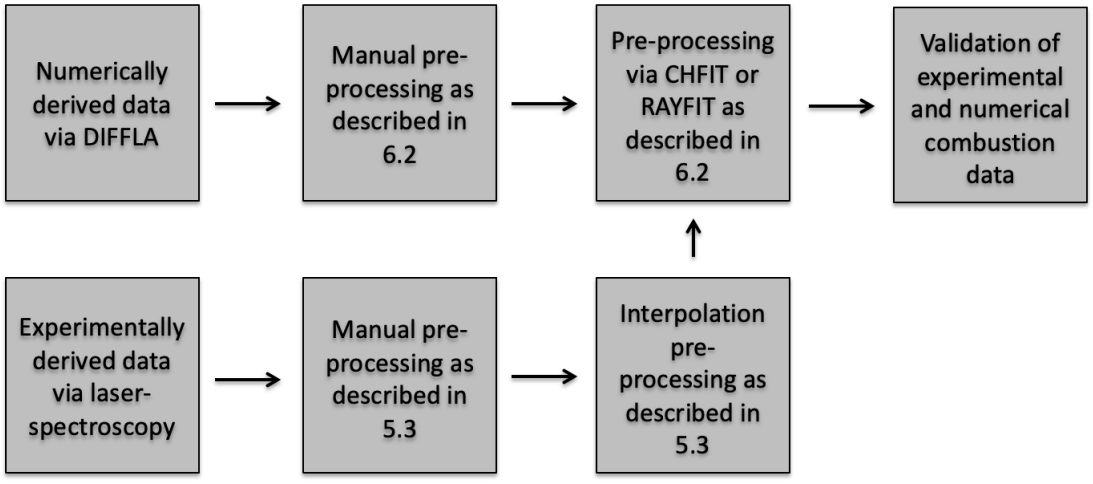

Figure 6.1: *Schematic representation of the numerical and experimental data flows*

Both programs are fed input data of the experimentally derived and the modelled diffusion flame, to finally output the comparison of the two. *RAYFIT* is additionally in need of a file with $\rho_0\lambda$ and $R_L\lambda$ information to calculate the Rayleigh scattering for the involved chemical species. The numerical and experimental data flows are represented schematically in Figure 6.1 for a clearer overview.

Chapter 7

Results, discussion, and conclusions

The experimental investigations of counter-flow laminar diffusion flames with biomass-based gaseous fuels and diluted methane mixtures at various velocities will be discussed in the following chapter. The focus is on the spectroscopic investigations discussed in Chapter 4 of these fuels during combustion. Furthermore, straining out behavior, variation in dilution or fuel composition, oxygen addition, and other critical points of this investigation are considered and examined.
In all the following experimental and numerical curves presented, the fuel is induced from the left and the oxidizer (air) from the right side.

7.1 Diluted methane

Preceding the study of biomass-based gaseous fuels during laminar counter-flow combustion, an investigation of diluted methane mixtures with nitrogen and carbon dioxide as diluents was conducted.

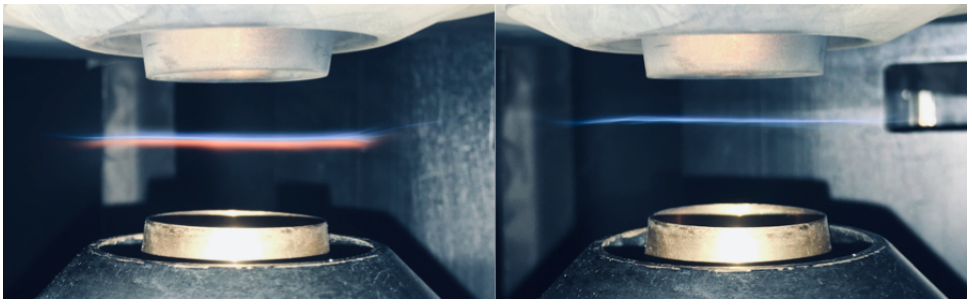

Figure 7.1: *Sooting methane flame (left) and non-sooting diluted methane flame (right) with air as oxidizer input from the top and fuel from the bottom nozzle*

Numerical and experimental solutions could therefore be validated for more fundamental fuel compositions, as opposed to the investigated complex synthetic model

fuel mixtures based on thermochemical conversion processes presented in 5.6. Furthermore, as previously mentioned, the experimental test rig could be internalized and verified. The involvement of diluents during hydrocarbon combustion influences the incandescence of fine soot particles, as presented in Figure 7.1.

7.1.1 Rayleigh measurements of diluted methane fuels

To establish the basis for the forthcoming Rayleigh intensity measurements and developments of complex gaseous mixtures and also to collect physical information in regard to the flames, like flame width and positioning, Rayleigh scattering experiments at 532 nm were executed. The combustion processes are more prone to disturbance and extinction when diluting fuels with non-combusting gases like nitrogen and carbon dioxide, though also possibly leading to reduced emissions and an increased control of the combustion. Dilution of hydrocarbons can be explained by the thermal, dilution, and chemical effects.

The dilution effect reduces the concentration of the reactants and thus influences the reaction rates. Furthermore, leading to the fact that the radical pool decreases. This is reinforced by the thermal effect, as fewer radicals are present in flames combusting at lower temperatures. The dilution effect when introducing carbon dioxide as diluent is greater than when using nitrogen, not due to the triatomic vs. diatomic structure of the gases, but based on the heat capacities. The chemical effect of carbon dioxide in hydrocarbon combustion can shift the chemical equilibrium towards the direction of the reactants. Nitrogen, in comparison, shows no chemical effect on the combustion processes [99, 225, 226].

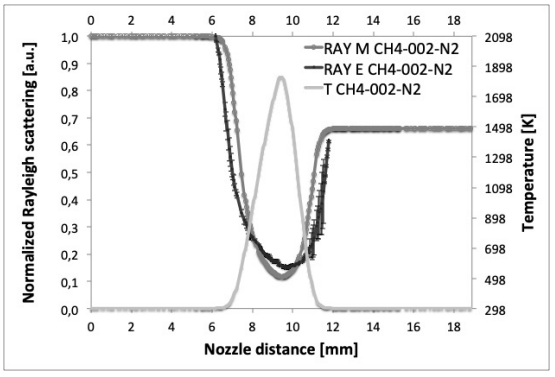

Figure 7.2: *Experimentally derived and modelled Rayleigh scattering and temperature curves with a fuel mixture of CH4-002-N2 at* $60\,cms^{-1}$

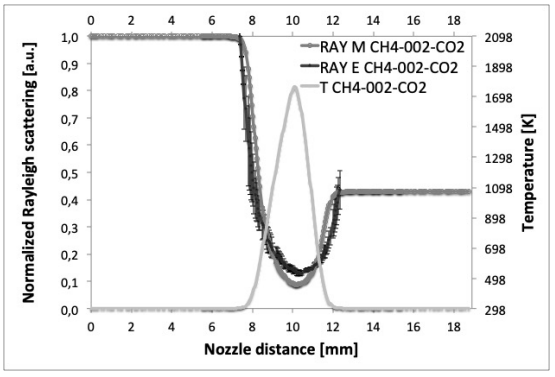

Figure 7.3: *Experimentally derived and modelled Rayleigh scattering and temperature curves with a fuel mixture of CH4-002-CO2 at* $60\,cms^{-1}$.

To investigate the development of the combustion processes, temperature fields, fluorescence, and CH* when increasing the fraction of diluents on the fuel side, multiple fuel compositions as illustrated in Table 5.3 were studied. At a fuel mixture of each 50 vol.-% methane and diluent as in CH4-001-X, there was still a clear sight of soot as seen in Figure 7.1, which led to incandescence and therefore deviations in the experimental investigation of laser-induced fluorescence and CH* chemiluminescence. Therefore, the Rayleigh scattering investigations were focused on fuel mixtures with a diluent content of 60 vol.-% or higher, in which sooting and its chemical effects could be decreased. Figures 7.2 - 7.6 show the studies of experimentally derived and modelled Rayleigh scattering and the numerically deduced temperature distribution in the flames.

The experimentally derived Rayleigh scattering curves are constantly circa 0.5 mm wider than the numerically calculated curves; this is still of good agreement as can be seen in Figure 7.2 for a fuel with nitrogen diluted methane and Figure 7.3 for carbon dioxide diluted methane. This difference in width between modelled and experimental solutions leads to variations in the positions of the minima of < 0.5 mm, as presented in Figure 7.4. Experimental uncertainties are $< 2.47\,\%$.

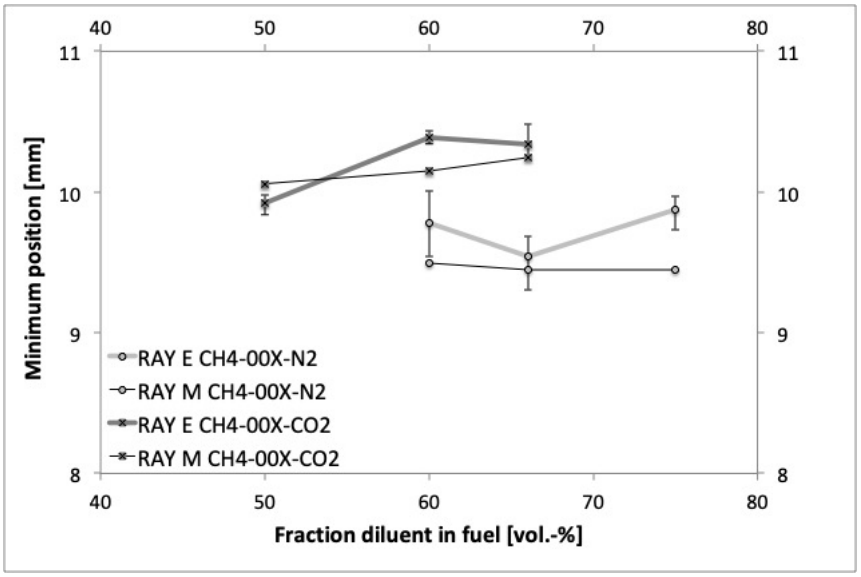

Figure 7.4: *Minima of experimentally and numerically derived Rayleigh scattering curves with fuel mixtures including varying fractions of nitrogen and carbon dioxide as diluents at* $60\,cms^{-1}$

Table 4.1 has already given an insight of the differential scattering cross section of major BDG gases and air. Carbon dioxide exceeds nitrogen by a factor of about 2.5, generally leading to lower temperatures when comparing the basic fuel mixtures with both diluents due to the temperature and scattering being in a negative correlation to each other.

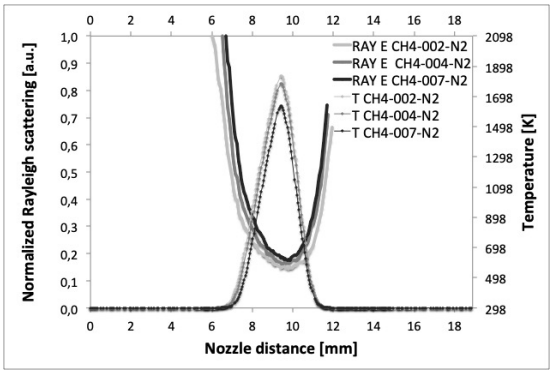

Figure 7.5: *Experimentally derived Rayleigh scattering and temperature curves with fuel mixtures of CH-002-N2 in comparison to CH4-004-N2 and CH4-007-N2 at* $60\,cms^{-1}$

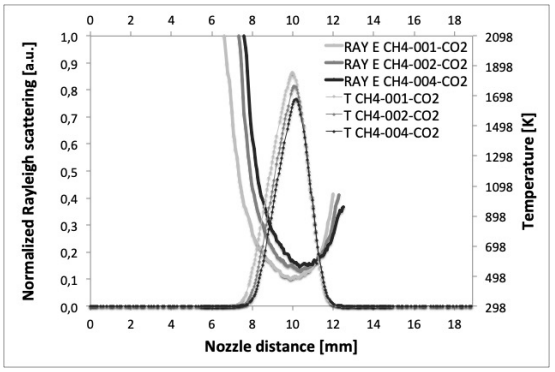

Figure 7.6: *Experimentally derived Rayleigh scattering and temperature curves with fuel mixtures of CH-001-N2 in comparison to CH4-002-CO2 and CH4-004-CO2 at* $60\,cms^{-1}$

Figure 7.5 shows the development of the flame geometry and temperature decrease with an increase of 60 vol.-% (CH4-002-N2) of nitrogen to 75 vol.-% (CH4-007-N2). CH4-007-N2 at 60 cms^{-1} with the available burner set-up was the fuel with the maximum nitrogen dilution that led to a stable combustion. This was the case during experimental and numerical investigation, again putting them in good agreement. The flames width decreases more than 1 mm, accordingly >20 % in size. The temperature declines from a maximum of 1837 K to 1634 K, subsequently about >10 %.

Based on the heat capacity of carbon dioxide, a combustion with a fuel composition of 75 vol.-% (CH4-007-CO2) diluent and 25 vol.-% methane is not feasible due to the cool temperature and previous strain out of the flame at these conditions. As presented in Figure 7.6, the highest fraction of carbon dioxide for a stable combusting flame at 60 cms^{-1} was 66 vol.-% (CH4-004-CO2), just before strain out. Between the flames, CH4-001-CO2 and CH4-004-CO2 16 vol.-% of methane was replaced with diluent. Leading to a temperature drop from a maximum of 1854 K to 1677 K. The flame width decreases likewise as in the nitrogen cases.

When regarding the carbon dioxide cases, with decreasing methane and increasing carbon dioxide in the fuel, the minimum Rayleigh intensity and, therefore, peak temperatures move closer to the air side of the flame. In the cases with increasing nitrogen in the compositions, the flame stays centered in the same position between the nozzles. This is also based on the increasing molar mass on the fuel sides when replacing methane with carbon dioxide, which is heavier by a factor of circa 2.75. The Rayleigh scattering intensity on the air sides should be equal when regarding all the experimental investigations. The finite of the laser sheet on both fuel- and air sides and the divergent normalization factors with differing diluents had an impact on the conclusive presentation of the experimental air side scattering.

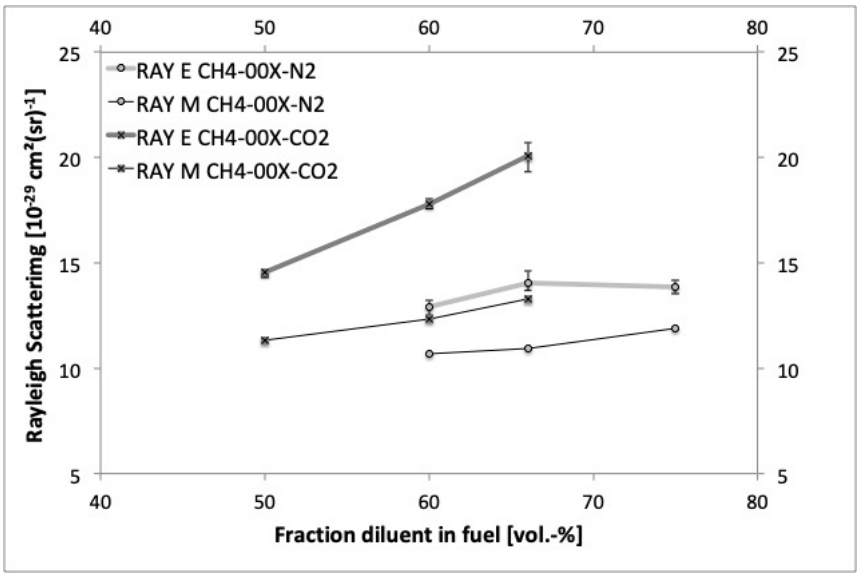

Figure 7.7: *Minimum Rayleigh scattering intensities of experimentally and numerically derived Rayleigh scattering curves with fuel mixtures including varying fractions of nitrogen and carbon dioxide as diluents at* $60\,cms^{-1}$

The scattering intensity minima of the experimentally derived Rayleigh scattering curves were consequently lower than their numerical counterparts, as was presented in Figures 7.2 and 7.3. This was consistently the case, as presented on the overview in Figure 7.7, showing all minimum Rayleigh scattering intensities of experimentally and numerically derived Rayleigh scattering curves for diluted methane fuels. This phenomenon also correlates with the deviating flame widths and can lead to a deviation of up to $5\,cm^2(sr)^{-1}$. Experimental uncertainties are $< 3.99\,\%$.

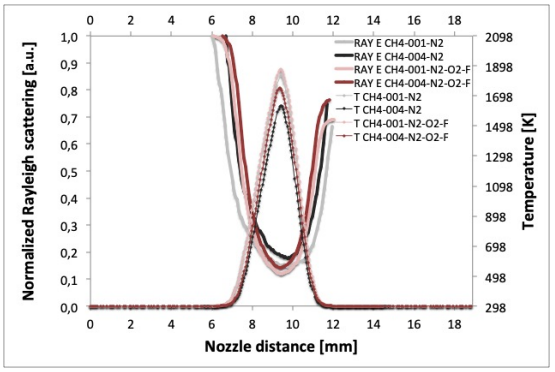

Figure 7.8: *Experimentally derived Rayleigh scattering and corresponding temperature curves with fuel mixtures of CH-001-N2 and CH4-004-N2 in comparison to CH-001-N2-O2-F and CH4-004-N2-O2-F at* $60\,cms^{-1}$

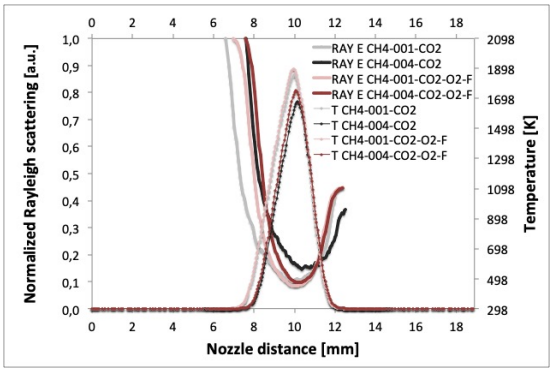

Figure 7.9: *Exp. derived Rayleigh scattering and corresponding temperature curves with fuel mixtures of CH-001-CO2 and CH4-004-CO2 in comparison to CH-001-CO2-O2-F and CH4-004-CO2-O2-F at* $60\,cms^{-1}$

As discussed, the change in composition from CH4-001-CO2 to CH4-004-CO2 led to a reduction in peak temperature from 1854 K to 1677 K. In comparison, the change in composition from CH4-001-N2 to CH4-004-N2 lead to a drop from 1901 K to 1784 K. Subsequently, 5 vol.-% of oxygen were added to both the fuel- and air sides of the previously mentioned compositions, the solutions are presented in Figures 7.8 - 7.11.

In fuel compositions with 50 vol.-% of hydrocarbon, such as methane, and 50 vol.-% diluent, such as nitrogen and carbon dioxide, a displacement with oxygen of 5 vol.-% in the fuel composition has a slight impact on the peak temperatures, such as 39 K and 50 K, respectively. When increasing the share of diluent to 66 vol.-% the impact of oxygen displacement leads to a rise in peak temperatures of 116 K and 73 K, respectively.

This impact in peak temperatures increased when regarding Figures 7.10 and 7.11, where 5 vol.-% of oxygen was added to the air sides during combustion. Here the peak temperatures of fuel mixtures including 16 vol.-% more diluent than the 50 vol.-% hydrocarbon-diluent without oxygen addition mixtures are now quasi-equal. Also, peak temperatures > 2000 K (2009 K for nitrogen and 2020 K for carbon dioxide) can be measured for both the CH4-004-X-O2-A cases.

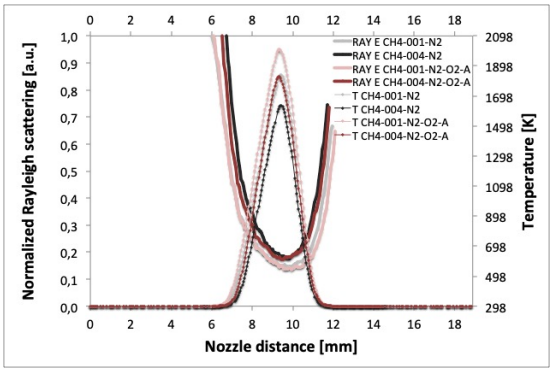

Figure 7.10: *Experimentally derived Rayleigh scattering and corresponding temperature curves with fuel mixtures of CH-001-N2 and CH4-004-N2 in comparison to CH-001-N2-O2-A and CH4-004-N2-O2-A at* $60\,cms^{-1}$

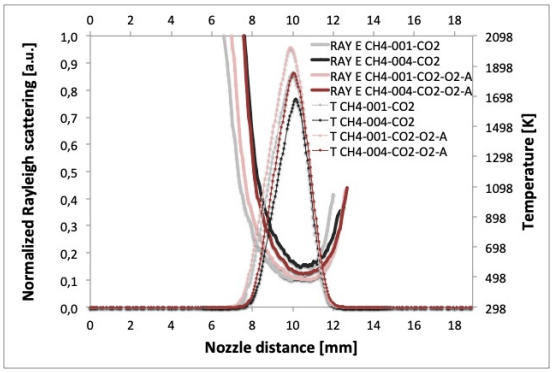

Figure 7.11: *Exp. derived Rayleigh scattering and corresponding temperature curves with fuel mixtures of CH-001-CO2 and CH4-004-CO2 in comparison to CH-001-CO2-O2-A and CH4-004-CO2-O2-A at* $60\,cms^{-1}$

7.1.2 Laser-induced fluorescence of diluted methane fuels

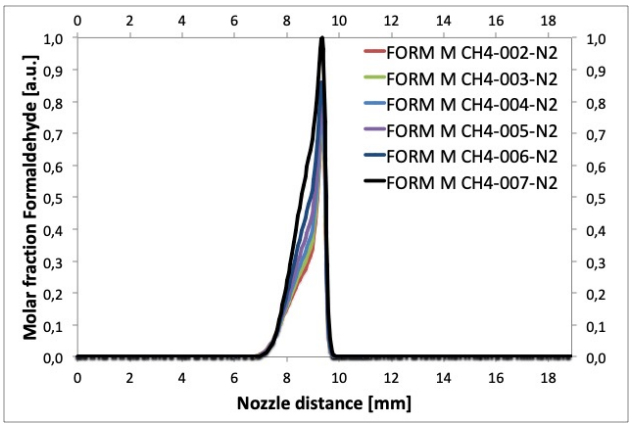

Figure 7.12: *Numerically derived formaldehyde curves with fuel mixtures of CH-002-N2 - CH4-007-N2 at* $60\,cms^{-1}$

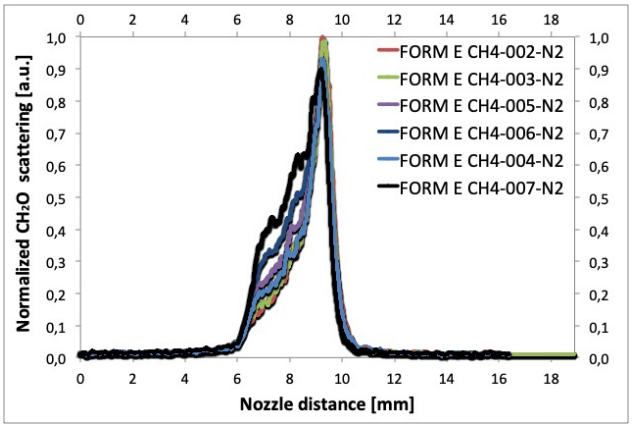

Figure 7.13: *Experimentally derived laser-induced fluorescence curves at* $355\,nm$ *with fuel mixtures of CH-002-N2 - CH4-007-N2 at* $60\,cms^{-1}$

As mentioned in the previous chapters, formaldehyde is formed as an intermediate species during the combustion of hydrocarbons and can be detected via laser-induced fluorescence experiments at 355 nm. Formaldehyde is mainly found when a hydrocarbon and air mixture reaches the explosion limit, which can be associated with a ‚cool flame', this helps in the detection of the iniation and progression of the combustion process [150].

When applying fluorescence at 355 nm during combustion, the difficulty of measuring actual formaldehyde curves when combusting hydrocarbon mixtures as fuels are a substantial challenge. Since the formaldehyde fluorescence spectrum can be found starting at around 350 nm over a length of more than 200 nm, multiple other hydrocarbon compounds, which are also excited at 355 nm, lead to a greater extent of fluorescence intensity.

In this investigation, the fluorescence measurements were focussed 30 nm above and below 417 nm. When additionally following the steps for the data processing described in Section 5.3, the diluted methane fuels using nitrogen represented in Figures 7.12 and 7.13 showed the numerical and experimental results to be in good agreement. The physical position of the formaldehyde evolution between the fuel- and air nozzles is in excellent agreement for both the experimentally derived and the calculated curves.

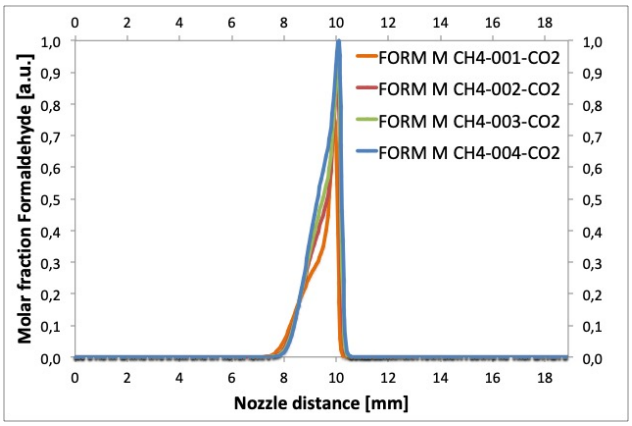

Figure 7.14: *Numerically derived formaldehyde curves with fuel mixtures of CH-001-CO2 - CH4-004-CO2 at* $60\,cms^{-1}$

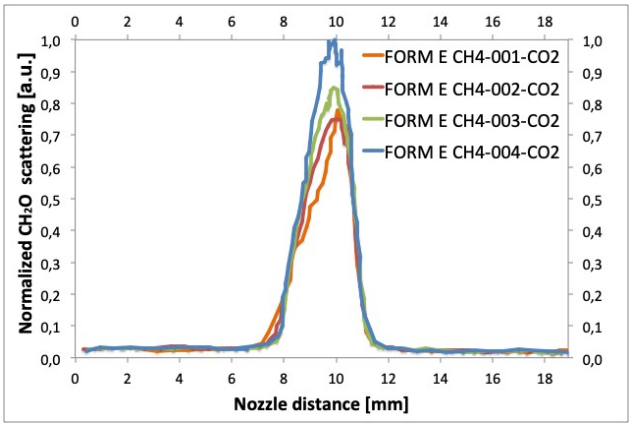

Figure 7.15: *Experimentally derived laser-induced fluorescence curves at* $355\,nm$ *with fuel mixtures of CH-001-CO2 - CH4-004-CO2 at* $60\,cms^{-1}$

The development of the bulgy curvature on the fuel sides evolves identical, when the fuels increase in nitrogen and decrease in methane. The peak intensities are not in ideal agreement for the nitrogen cases, as opposed to the carbon dioxide cases represented in Figures 7.14 and 7.15. The physical positions and the increase in peak intensity when adding diluent to the fuel side are in good accordance in the numerical and experimental cases. In contrast to the nitrogen cases, the experimental carbon dioxide cases seem to be generally curvier than the numerical counterparts. With both diluents, the formaldehyde fluorescence curves are wider in the experimental than the numerical cases, which is accordant to the Rayleigh scattering solutions.

7.1.3 CH* chemiluminescence and CH of diluted methane fuels

Lastly, the experimental CH* chemiluminescence data are compared to numerically calculated CH for diluted methane flames. As previously discussed, due to the main emission of excited CH peaking near 431 nm, a very narrow filter around this wavelength with only 5 nm below and above was used for the experimental investigations. Figures 7.16 and 7.17 represent both solutions for the CH4-002-X fuel cases, at fuel and air side velocities of 60 cms^{-1}. In the numerical cases the CH radical is presented; during the experimental investigations the intensities of the excited CH radical during chemiluminescence is measured. This is based on the limitations of the spectroscopic measuring set-up. The focus of these CH investigations, is the validation of the modelled CH peak positioning, which is still feasible due to the close relations of the positioning of the ground and excited states of the CH radical [136].

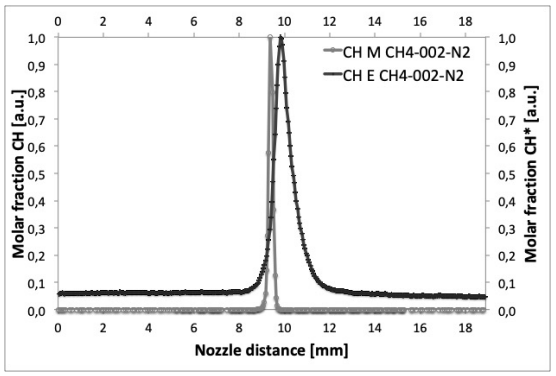

Figure 7.16: *Numerically derived CH and experimentally derived CH* chemiluminescence curves with fuel mixtures of CH-002-N2 at* $60\,cms^{-1}$

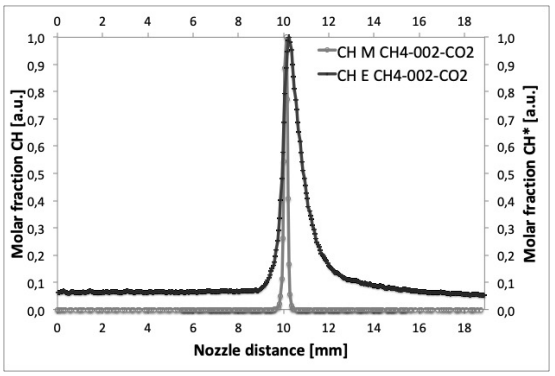

Figure 7.17: *Numerically derived CH and experimentally derived CH* chemiluminescence curves with fuel mixtures of CH-002-CO2 at* $60\,cms^{-1}$

As expected, the experimental cases are broader in size than the modelled ground state CH. This is based on background radiation from soot and/or CO_2* chemiluminescence emissions, as presented in Section 4.3.

The peak position when using nitrogen as the diluent in the fuel mixtures is circa 0.5 mm closer to the fuel sides during the experimental investigations, as presented in Figures 7.18 and 7.19. This can still be referred to as a good agreement when compared to the numerically calculated models. The developments of the peak intensities of CH* and CH decrease when the share of nitrogen increases, which is also in accordance when regarding all the results. The peak development of the carbon dioxide cases can be observed in Figures 7.20 and 7.21. The peak position is about 0.2 mm off for the fuels with $> 50\,\%$ diluent and surprisingly further offsided to the fuel side for the CH4-001-CO2 measurement. All these curves were normalized with the maximum intensity of each figure.

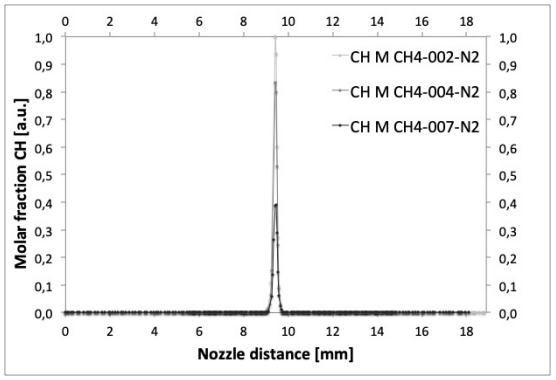

Figure 7.18: *Numerically derived CH curves with fuel mixtures of CH-002-N2, CH-004-N2, and CH-007-N2 at* $60\,cms^{-1}$

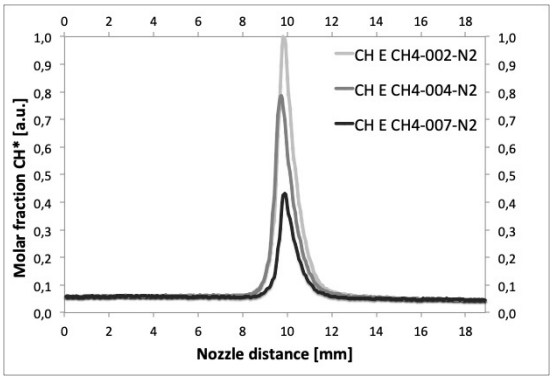

Figure 7.19: *Experimentally derived CH* chemiluminescence curves with CH-002-N2, CH-004-N2, and CH-007-N2 fuels at* $60\,cms^{-1}$

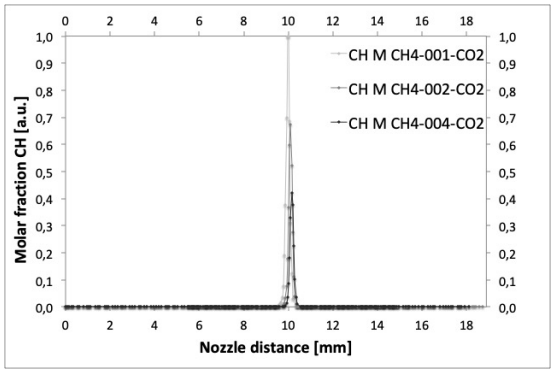

Figure 7.20: *Numerically derived CH curves with fuel mixtures of CH-001-CO2, CH-002-CO2, and CH-004-CO2 at* $60\,cms^{-1}$

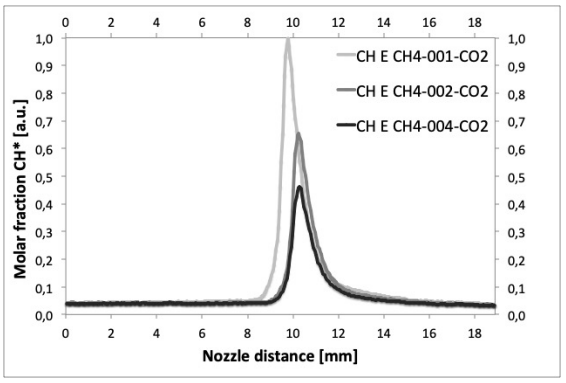

Figure 7.21: *Exp. derived CH* chemiluminescence curves with CH-001-CO2, CH-002-CO2, and CH-004-CO2 fuels at* $60\,cms^{-1}$

In Figure 7.22, the peak positions of all methane fuels in regard to the fraction of diluent in the fuel are presented. As was expected, based on the minima of the Rayleigh scattering solutions presented in Section 7.1.1, the numerical maxima are continuously slightly closer to the fuel side. The off-set in the peak positions are $< 0.5\,\text{mm}$ for the nitrogen cases and $< 0.2\,\text{mm}$ for the carbon dioxide cases, the experimentally and numerically derived CH* chemiluminescence and CH curves are therefore regarded to be in very good agreement for these methane fuels. Experimental uncertainties are $< 1.94\,\%$.

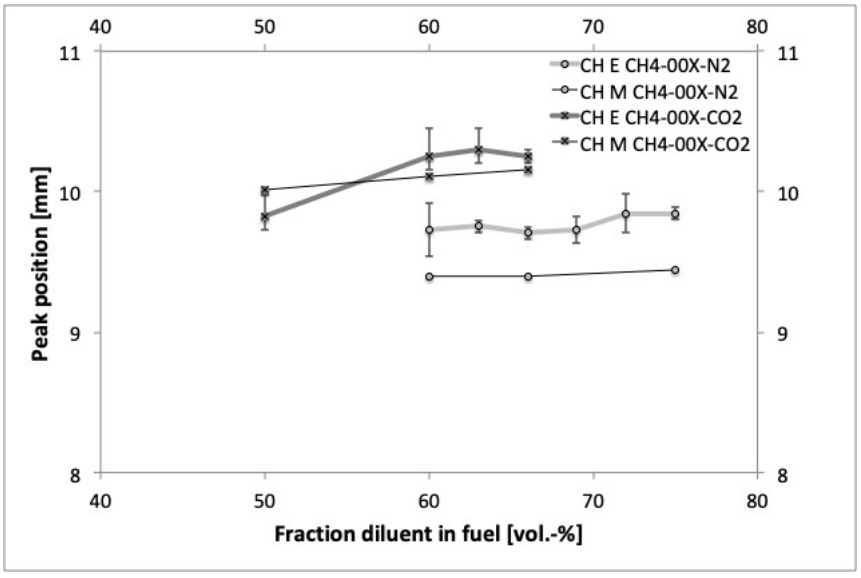

Figure 7.22: *Peak positions of experimentally and numerically derived CH* chemiluminescence and CH curves with methane fuel mixtures including varying fractions of nitrogen and carbon dioxide as diluents at* $60\,cms^{-1}$

7.2 Biomass-based gaseous fuels - GGL2, GGL3, and PG

In the previous section, the verification of the experimental test rig on the basis of spectroscopic measurements and the numerical model DIFFLA resulted in good agreements for numerous basic hydrocarbon fuel compositions. In the following sections, the conclusions will be applied to more complex fuel based on synthetic model product gases from biomass gasification and pyrolysis processes, which are presented in Table 5.6.

7.2.1 Rayleigh measurements of biomass-based gaseous fuels

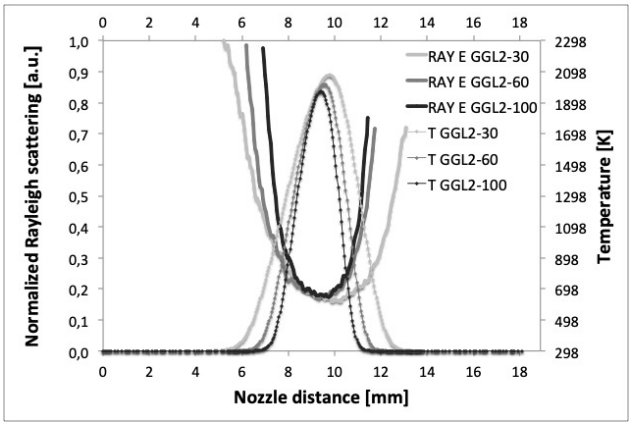

Figure 7.23: *Experimentally derived Rayleigh scattering and temperature curves with fuel mixtures of GGL2 at* $30\,cms^{-1}$, $60\,cms^{-1}$, *and* $100\,cms^{-1}$

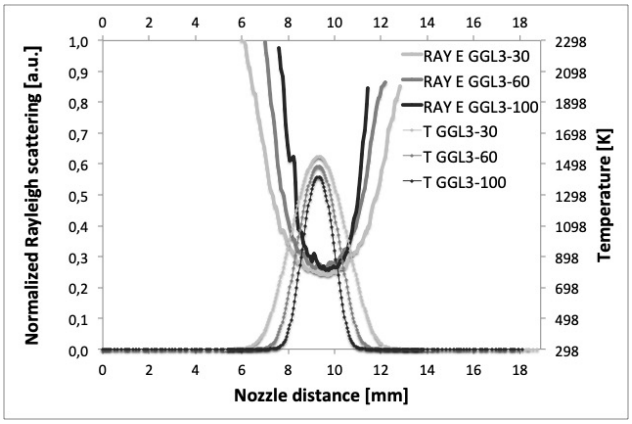

Figure 7.24: *Experimentally derived Rayleigh scattering and temperature curves with fuel mixtures of GGL3 at* $30\,cms^{-1}$, $60\,cms^{-1}$, *and* $100\,cms^{-1}$

In Figures 7.23 and 7.24 the Rayleigh scattering and temperature developments for fuel based on gasification processes GGL2 and GGL3 are presented for fuel and air velocities of 30 cms^{-1}, 60 cms^{-1} and 100 cms^{-1}. For both fuels, the physical positioning between the nozzles are adequate, slight off-sets can be observed for the slower cases, when compared to the models. The flames widths are represented best for the faster case of 100 cms^{-1} velocities, as expected.

As the velocities increase when combusting GGL2, the flames are pushed closer to the fuel side. This might be based on the big fraction of hydrogen, with a very small molar mass, as opposed to the oxidizer air. The temperature evolutions differ immensely due to the great inequality of diluents vs. combustibles in the generated fuel blends. As presented in Table 5.6 30.4 vol.-% vs. 69.6 vol.-% and 68.9 vol.-% vs. 31.1 vol.-% for GGL2 and GGL3, respectively. The maximum temperatures at 30 cms^{-1} for these fuels differ by

an amount of 530 K at 2076 K and 1546 K for GGL2 and GGL3, respectively. When comparing to the fuels from pyrolysis presented in Figure 7.25 also at velocities of 30 cms^{-1}, 60 cms^{-1}, and 100 cms^{-1}, more equalities are established towards fuel GGL2. PG shows a diluent vs. combustibles ratio of 35 vol.-% vs. 65 vol.-%, with no nitrogen included. When fuel and air velocities are increased, the faster flames, therefore peak temperatures, are also pushed towards the fuel side. The peak temperature for 30 cms^{-1} is located at 1887 K, which is comparable to the diluted methane cases with more than 50 vol.-% methane, though having a much lower LHV in total.

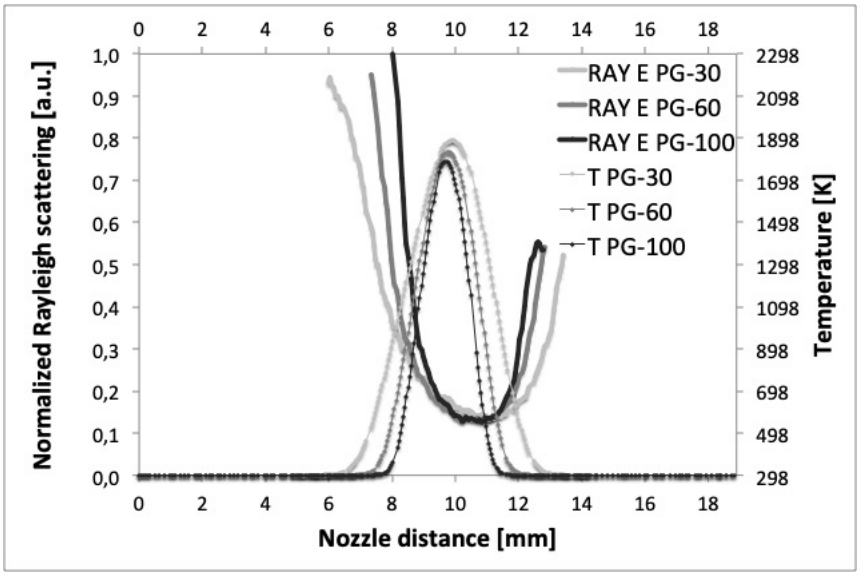

Figure 7.25: *Experimentally derived Rayleigh scattering and temperature curves with fuel mixtures of PG at* 30 cms^{-1}, 60 cms^{-1}, *and* 100 cms^{-1}

7.2.2 Laser-induced fluorescence of biomass-based gaseous fuels

During the preliminary investigations using diluted methane fuels, difficulties arose in developing the relation of experimentally determined formaldehyde via laser-induced fluorescence and the numerical model. These could be thoroughly worked out with corresponding filters and data processing measures. The intensity of the derived LIF formaldehyde scattering when investigating GGL2, GGL3, and PG at multiple air and fuel velocities was very divergent, based on the composition of these fuels and their potentials to produce this intermediate species. As the fuel and oxidizer velocities increase from 30 cms^{-1} to 60 cms^{-1} to 100 cms^{-1} for the formaldehyde measurements using GGL2 as fuel presented in Figure 7.26, the peak intensities also rise. Also, smaller second peaks evolve closer to the fuel sides, where the temperatures are close to 1000 K.

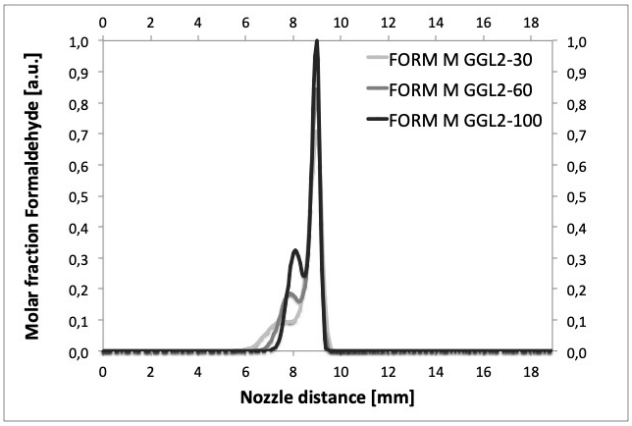

Figure 7.26: *Numerically derived formaldehyde curves with fuel mixtures of GGL2 at* $30\,cms^{-1}$, $60\,cms^{-1}$, *and* $100\,cms^{-1}$

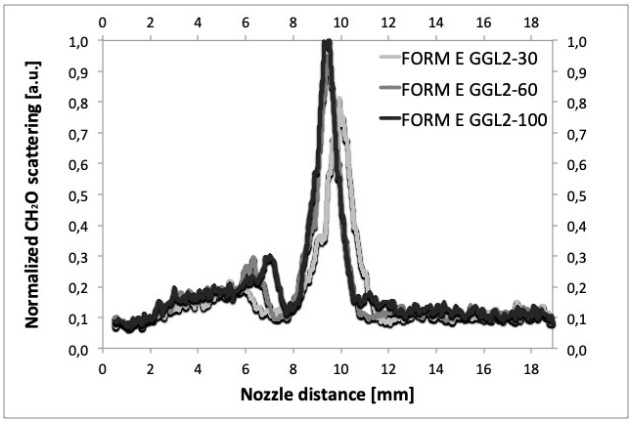

Figure 7.27: *Experimentally derived laser-induced fluorescence curves at* $355\,nm$ *with fuel mixtures of GGL2 at* $30\,cms^{-1}$, $60\,cms^{-1}$, *and* $100\,cms^{-1}$

This is a lower temperature area, where formaldehyde is knowingly prone to be formed. At GGL2-30 the second peak shows a smoother transition to the maximum peak at the fuel side, as opposed to GGL2-100 where a distinct crater forms before rising to the maximum formaldehyde intensity. As presented in Figure 7.27, during the experimental investigations two peaks emerged likewise for all regarded velocities. GGL2-30 is broader than the modelled counterpart, as was shown in Fig. 7.23 during Rayleigh scattering. The rise in main peak intensity is in comparable agreement, while the side peaks differ in their increasing intensity, according to the numerical model. When connecting these results to Figures 7.28 and 7.29, where GGL3 was used as fuel, the development of two peaks can also be observed. For the modelled GGL3-100, the second peak, closer to the fuel side, even exceeds the main peak.

This is based on the temperature distribution, as was presented in the previous section. The temperatures predominating during all of the combustion processes investigated when using GGL3 as fuel are prevailing in the complete flame. These cooler GGL3 flame serve as an ideal environment for an extensive formaldehyde evolution, in spite of the major share of diluent nitrogen in the fuels. The experimental investigations presented a two-peak distribution as well, but a much more limited rise in intensities when comparing these. This could be based on the difference in flame broadness when comparing the modelled and experimental data. The two peaks in Figure 7.28 at each temperature, respectively, are about 1 mm separated, as opposed to Figure 7.29, where the separation distance is partially > 2 mm. An additional 1 mm in flame broadness leads to a big displacement when considering the temperature gradient and therefore different actual temperatures and formaldehyde evolutions, then calculated models.

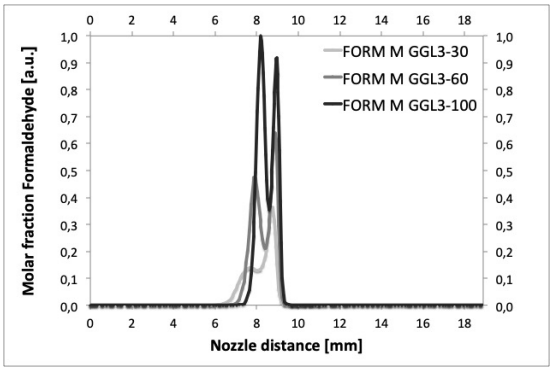

Figure 7.28: *Numerically derived formaldehyde curves with fuel mixtures of GGL3 at* 30, 60, *and* 100 cms^{-1}

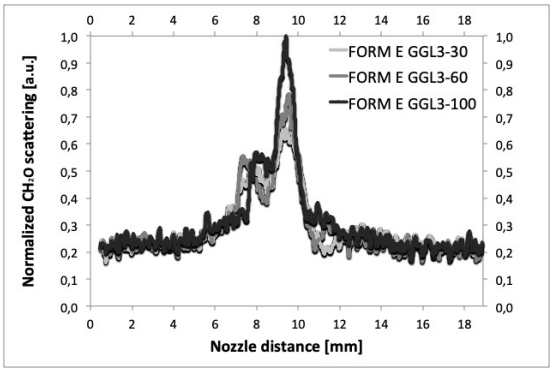

Figure 7.29: *Experimentally derived LIF curves at* 355 nm *with fuel mixtures of GGL3 at* 30, 60, *and* 100 cms^{-1}

The best agreement between models and experiments is illustrated in Figures 7.30 and 7.31 for the evolution of the PG fuels. The major and the minor peaks are in good alignment in all parts of the investigation. The modelled formaldehyde curves correspond to the experimentally derived LIF counterparts in form and trend. The rise of intensities with increasing velocities also correlates well. Finally, the reduction of the flames width at raised fuel and air velocities coincides correctly with the off-sets of the smaller peaks towards the air side. As previously seen in the GGL2 cases, the transitions between the secondary to the main peaks show stronger craters in the experimental cases in comparison to the numerical calculations. The correlation between the GGL2, GGL3, and PG fuel mixtures at 100 cms^{-1} is pictured in Figures 7.32 and 7.33, normalized in regard to the greatest peak at PG-100.

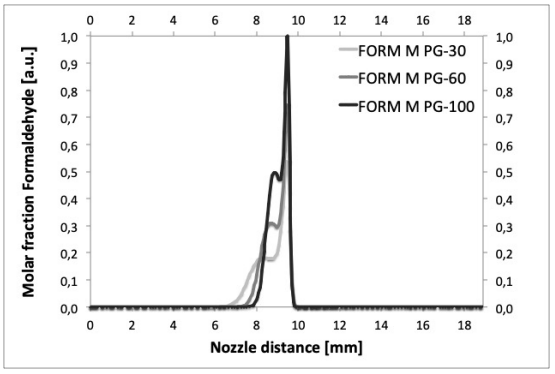

Figure 7.30: *Numerically derived formaldehyde curves with fuel mixtures of PG at* 30, 60, *and* 100 cms^{-1}

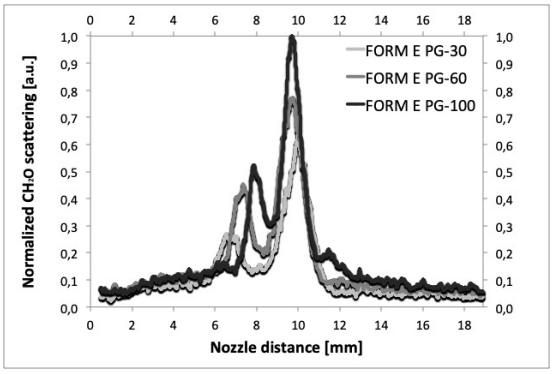

Figure 7.31: *Experimentally derived LIF curves at* 355 nm *with fuel mixtures of PG at* 30, 60, *and* 100 cms^{-1}

The relation between the curves fits very well in both modelled and experimental investigations. As expected, GGL2-100 leads to a smaller formaldehyde intensity, in comparison to the other fuels, due to considerably higher temperatures prevailing throughout the flame [26]. PG fuels include the largest amount of methane in the fuel composition; therefore the greatest overall intensity of formaldehyde throughout the flame was measured, as expected [149, 227].

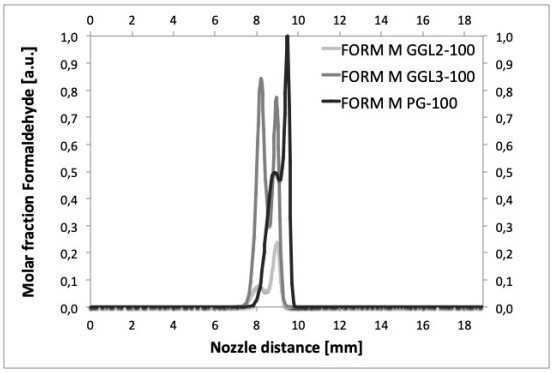

Figure 7.32: *Numerically derived formaldehyde curves with fuel mixtures of GGL2, GGL3, and PG at* $100\,cms^{-1}$

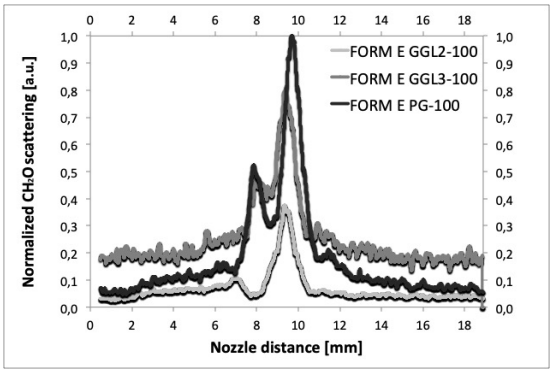

Figure 7.33: *Experimental LIF curves at* $355\,nm$ *with fuel mixtures of GGL2, GGL3, and PG at* $100\,cms^{-1}$

7.2.3 CH* chemiluminescence and CH of biomass-based fuels

Lastly, experimental CH* chemiluminescence measurements were compared to numerically modelled CH curves in regard to intensity evolution, form, and peak positioning.

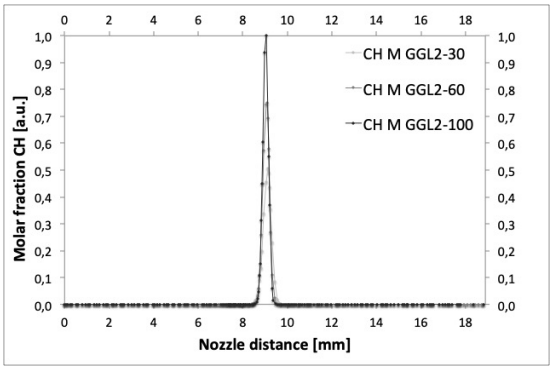

Figure 7.34: *Numerically derived CH curves with fuel mixtures of GGL2 at velocities of* $30\,cms^{-1}$, $60\,cms^{-1}$, *and* $100\,cms^{-1}$

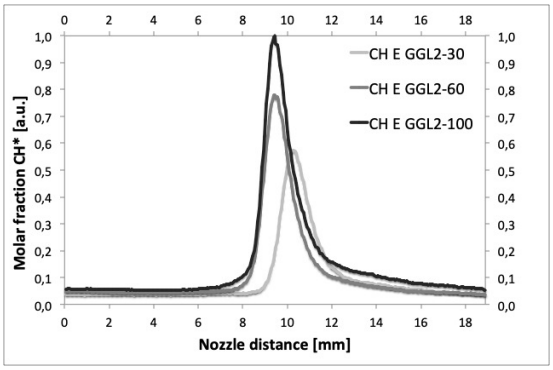

Figure 7.35: *Experimentally derived CH* chemiluminescence curves with fuel mixtures of GGL2 at velocities of* 30, 60, *and* $100\,cms^{-1}$

Flame GGL2-30 is slightly closer to the air side, as was expected from the solutions of the Rayleigh scattering and fluorescence measurements. Furthermore, the peak positioning and intensity development are in excellent agreement for GGL2 fuels, as pictured in Figures 7.34 and 7.35, as is the case for PG fuels plotted in Figures 7.36 and 7.37. For all of these solutions, the experimental curves are broader in size than the numerical counterpart, as was discussed in Section 7.1.3.

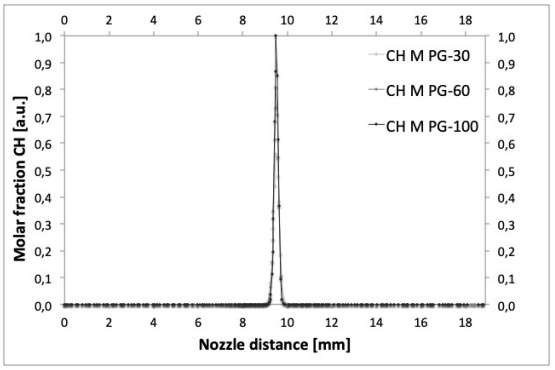

Figure 7.36: *Numerically derived CH curves with fuel mixtures of PG at velocities of* $30\,cms^{-1}$, $60\,cms^{-1}$, *and* $100\,cms^{-1}$

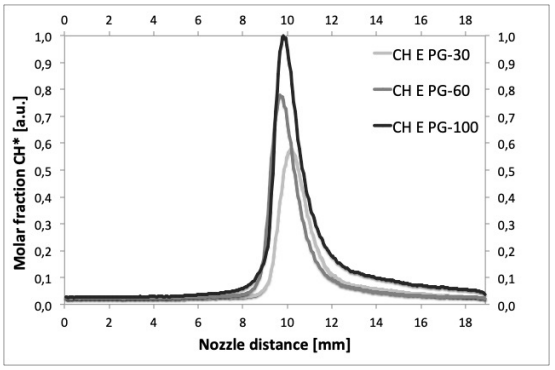

Figure 7.37: *Experimentally derived CH* chemiluminescence curves with fuel mixtures of PG at velocities of* 30, 60, *and* $100\,cms^{-1}$

As witnessed in the previous section during the formaldehyde measurements, the GGL3 fuels do not quite agree with the models, as presented in Figures 7.38 and 7.39. The LIF measurements did not agree with the increase of intensity for the peaks closer to the fuel side at raised velocities; the chemiluminescence investigations do not agree with the decrease of intensity at enlarged velocities.

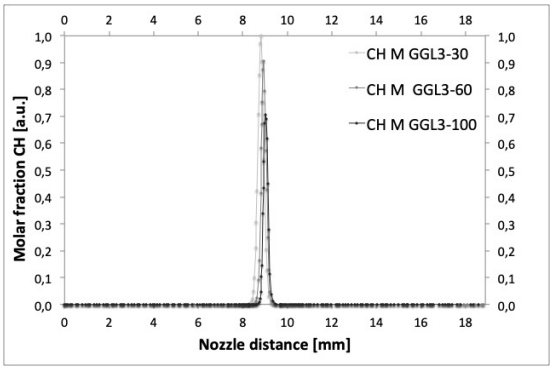

Figure 7.38: *Numerically derived CH curves with fuel mixtures of GGL3 at velocities of* $30\,cms^{-1}$, $60\,cms^{-1}$, *and* $100\,cms^{-1}$

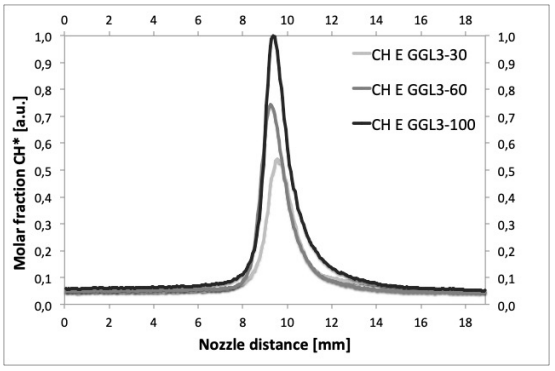

Figure 7.39: *Experimentally derived CH* chemiluminescence curves with fuel mixtures of GGL3 at velocities of* 30, 60, *and* $100\,cms^{-1}$

An assumption could be that the oxygen of the oxidizer does not arrive at the flame front in the quantity that is numerically modelled. Due to 61 vol.-% nitrogen present in the fuel for the GGL3 cases, the formaldehyde evolution in the flames is strongly

in need of the oxygen from the oxidizer. This proposition is also strengthened by the surplus of CH molecules measured during the experiments at raised velocities.

Illustrated in Figure 7.40 are the maximum peak positions of experimentally and numerically derived CH* chemiluminescence and CH curves with fuel mixtures of GGL2, GGL3, and PG at $30\,cms^{-1}$, $60\,cms^{-1}$, and $100\,cms^{-1}$. For all investigated fuels, the peaks show a maximum displacement of $< 0.5\,\text{mm}$. The best agreement can be reached at the fastest velocity, $100\,cms^{-1}$, as expected. The slowest velocity at $30\,cms^{-1}$ presents an edge case for stable combustion for the regarded experimental set-up. Experimental uncertainties are $< 1.82\,\%$.

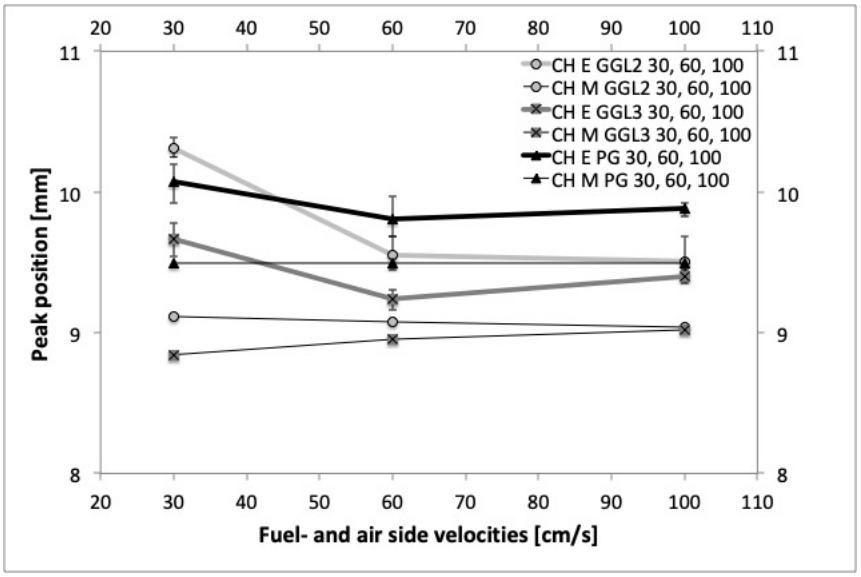

Figure 7.40: *Peak positions of experimentally and numerically derived CH* chemiluminescence and CH curves with fuel mixtures of GGL2, GGL3, and PG at* $30\,cms^{-1}$, $60\,cms^{-1}$, *and* $100\,cms^{-1}$

7.3 Biomass-based gases with additional oxygen on the fuel side

This section investigates the combustion behavior of biomass-based gases with additional oxygen supplied during the combustion process on the fuel sides for the given fuel compositions GGL2, GGL3, and PG, as previously presented in Table 5.7. This should provide further insights into the utilization of these product gases from biomass gasification or pyrolysis in industrial applications.

7.3.1 Temperature evolution with additional fuel side oxygen

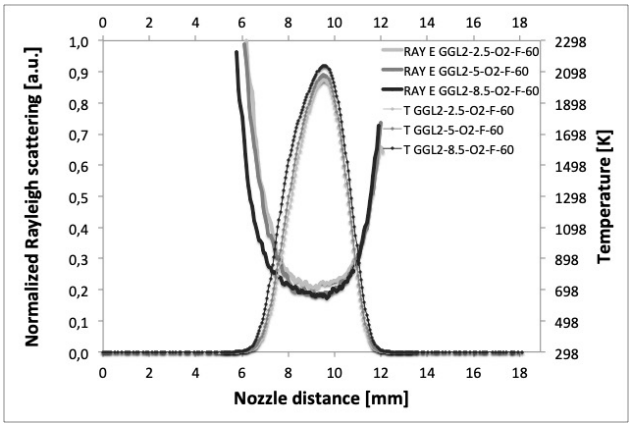

Figure 7.41: *Experimentally derived Rayleigh scattering and temperature curves with fuel mixtures of GGL2 at* $60\,cms^{-1}$ *and additional fuel side oxygen of* $2.5,\ 5,$ *and* $8.5\,vol.-\%$

As plotted in Figure 7.41, the addition of $2.5, 5,$ and 8.5 vol.-% of oxygen to the fuel side when combusting GGL2 fuel lead to an increase of peak temperatures of $27, 60,$ and 118 K respectively in comparison to the case without oxygen addition. Furthermore, the flame width increased markedly for a considerable amount of 8.5 vol.-% added, which can not be observed for the other GGL2 cases. The evolution for the PG cases in Figure 7.43 displayed an analogous behavior.

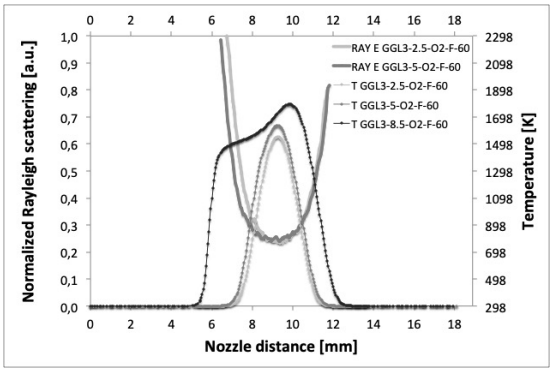

Figure 7.42: *Exp. derived Rayleigh scattering and temperature curves with fuel mixtures of GGL3 at* $60\,cms^{-1}$ *and additional fuel side oxygen of* $2.5\,vol.-\%,\ 5\,vol.-\%,$ *and* $8.5\,vol.-\%$

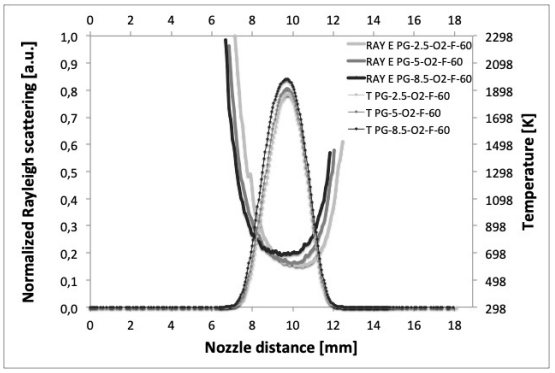

Figure 7.43: *Experimentally derived Rayleigh scattering and temperature curves with fuel mixtures of PG at* $60\,cms^{-1}$ *and additional fuel side oxygen of* $2.5\,vol.-\%,\ 5\,vol.-\%,$ *and* $8.5\,vol.-\%$

Furthermore, especially for the PG cases, the Rayleigh scattering minima and, therefore, peak temperatures were pushed significantly in the direction of the fuel side. The GGL3 experiments and models presented in Figure 7.42 encountered an extremer influence by the addition of oxygen in the fuel composition. At inputs of 2.5 vol.-% and 5 vol.-% an increase of peak temperatures of 67 and 148 K was detected, at 8.5 vol.-% as much as 309 K. This last case presented an increase of > 20 vol.-% in temperature, but can not be regarded as a stable case. The numerical model demonstrates the combustion instability with this amount of fuel side oxygen appropriately, which could not be investigated experimentally due to its fluctuations.

Finally, a comparison of the minima of experimentally and numerically derived Rayleigh scattering curves with with fuel mixtures of GGL2, GGL3, and PG at

$60\,cms^{-1}$ and additional fuel side oxygen of $0\,vol.$-%, $2.5\,vol.$-%, $5\,vol.$-%, and $8.5\,vol.$-% are plotted in Figure 7.44. As previously mentioned, the experimental PG case minima have moved up to 1 mm closer to the fuel side. The GGL3 cases are in excellent agreement; the GGL2 cases are mostly in good agreement when regarding the positioning of the experimentally and numerically derived scattering minima. The evolution of the scattering when adding additional fuel side oxygen to these combustion processes and the temperatures will be further discussed in Section 7.5.2. Experimental uncertainties are $< 3.48\,\%$.

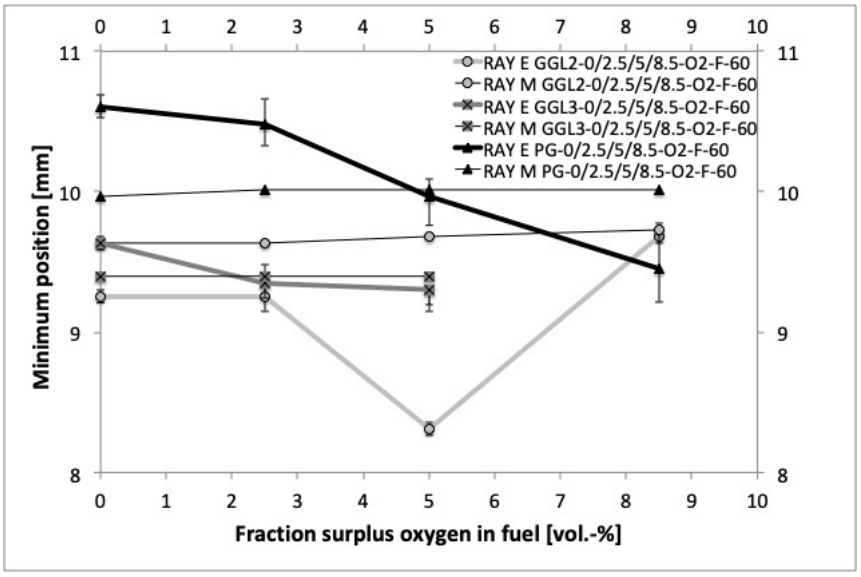

Figure 7.44: *Minima of experimentally and numerically derived Rayleigh scattering curves with fuel mixtures of GGL2, GGL3, and PG at* $60\,cms^{-1}$ *and additional fuel side oxygen of* $0\,vol. - \%$, $2.5\,vol. - \%$, $5\,vol. - \%$, *and* $8.5\,vol. - \%$

7.3.2 LIF of biomass-based gases with additional fuel side oxygen

An addition of oxygen to the combustion via the fuel composition had an overall drastic influence on the formaldehyde formation and will be presented in the following section.

In Figures 7.45 and 7.46, the combustion of GGL2 at $60\,\mathrm{cms}^{-1}$ with and without additional fuel side oxygen of 5 vol.-% is plotted. Showing a two-peak distribution of formaldehyde. As expected, the addition of fuel side oxygen has a considerable impact, especially on the before discussed smaller peak closer to the fuel side. This great formaldehyde intensity peak can be allocated at a temperature distribution of around 1000 K when consulting Figure 7.41 in the previous Section 7.3.1. Considering the continuously identified slightly increased flame widths for the

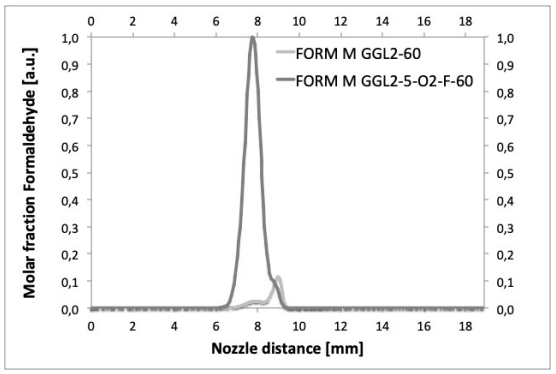

Figure 7.45: *Numerically derived formaldehyde curves with fuel mixtures of GGL2 at* $60\,cms^{-1}$ *with and without additional fuel side oxygen of* $5\,vol.-\%$

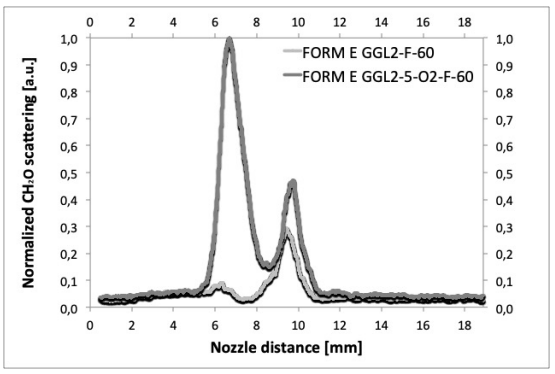

Figure 7.46: *Experimentally derived LIF curves at* $355\,nm$ *with fuel mixtures of GGL2 at* $60\,cms^{-1}$ *with and without additional fuel side oxygen of* $5\,vol.-\%$

experimentally derived results, the distances of the peaks throughout the flames seem to be reasonable. The previously stated „main peaks“ show an enlarged increase in intensity when compared to the numerical model. This could be traced back to other, bigger hydrocarbon bonds also fluorescing at 355 nm, especially in regard to GGL2-5-O2-F-60. The progression in regard to the formaldehyde intensity when increasing fuel- and air side velocities is plotted in Figures 7.47 and 7.48. Striking is once again the deep crater that develops for all fractions of oxygen added to the fuel side compositions. The numerical model does show smaller shoulders developing at the air side, next to the main intensity peaks. The experimental solutions though, present two definite curves. As previously discussed, this could either be based on the additional intensity of other hydrocarbons that are excited at 355 nm and fluoresce between $387-447$ nm. Another cause could be an aberration of the interpolation process described in 5.3. This mechanism was based on methane and oxygen flames, partly diluted with nitrogen.

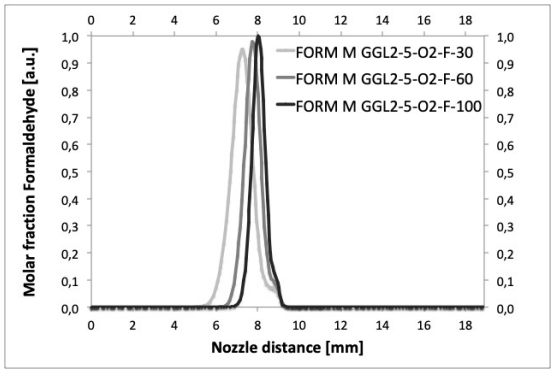

Figure 7.47: *Numerically derived formaldehyde curves with fuel mixtures of GGL2 at* 30, 60, *and* $100\,cms^{-1}$ *with additional fuel side oxygen of* $5\,vol.-\%$

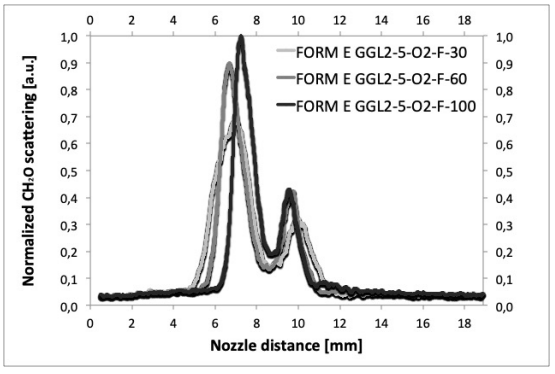

Figure 7.48: *Experimentally derived LIF curves at* $355\,nm$ *with fuel mixtures of GGL2 at* 30, 60, *and* $100\,cms^{-1}$ *with additional fuel side oxygen of* $5\,vol.-\%$

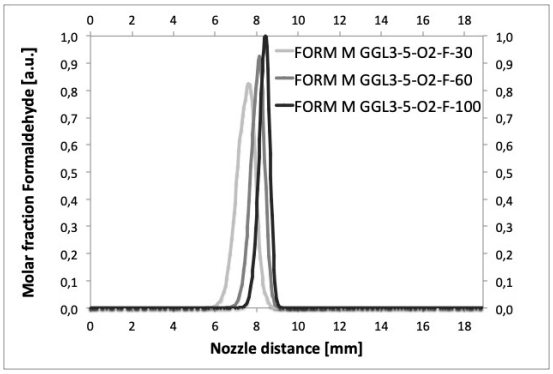

Figure 7.49: *Numerically derived formaldehyde curves with fuel mixtures of GGL3 at* 30, 60, *and* $100\,cms^{-1}$ *with additional fuel side oxygen of* $5\,vol.-\%$

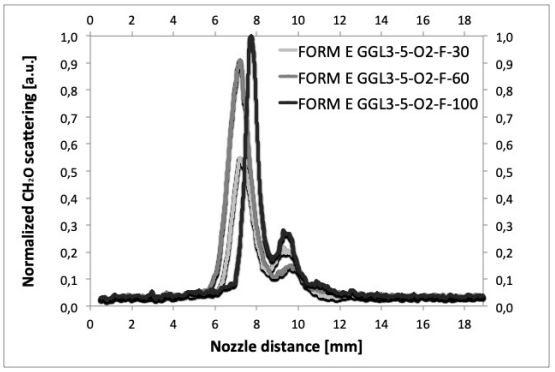

Figure 7.50: *Experimentally derived LIF curves at* $355\,nm$ *with fuel mixtures of GGL3 at* 30, 60, *and* $100\,cms^{-1}$ *with additional fuel side oxygen of* $5\,vol.-\%$

As presented in section 7.1, this procedure showed a very good agreement when basing it on similar diluted methane flame types. Presumably, the temperature curves have not been interpolated amply in regard to the high flame temperatures, which are most prominent at GGL2, which created two peaks as opposed to one. Or reversed: the model did not present the strong temperature gradient of formaldehyde sufficiently. The physical positions of the flames between the nozzles continuously show good agreement when incorporating the increased width of the experimental solutions.

The GGL3 fuels with added oxygen exhibited in Figures 7.49 and 7.50 showed similar results in comparison to the GGL2 fuels. The difference lies in the missing shoulder in the curves at the air side when modelled. This missing shoulder in the numerical solutions is represented by a much smaller second peak in the experimental investigation. Also included in this consideration should be the substantially lower prevailing temperatures during GGL3 combustion.

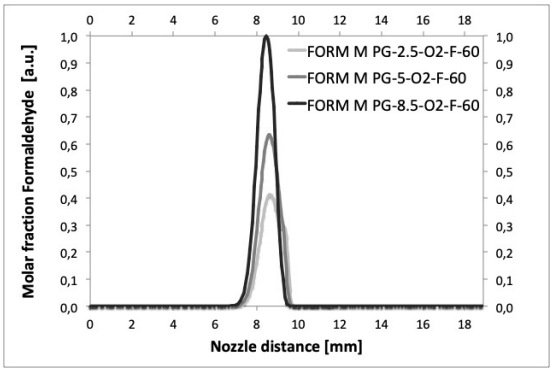

Figure 7.51: *Numerically derived formaldehyde curves with fuel mixtures of PG at* $60\,cms^{-1}$ *with additional fuel side oxygen of* 2.5, 5, *and* $8.5\,vol.-\%$

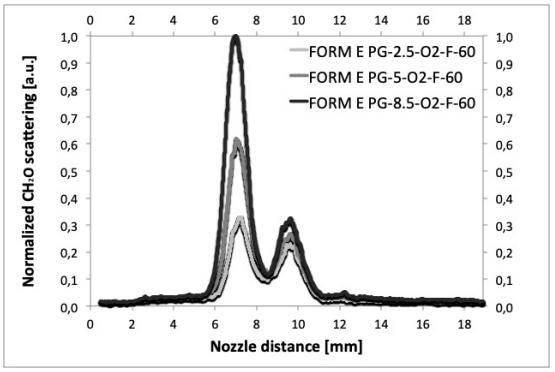

Figure 7.52: *Experimentally derived LIF curves at* $355\,nm$ *with fuel mixtures of PG at* $60\,cms^{-1}$ *with additional fuel side oxygen of* 2.5, 5, *and* $8.5\,vol.-\%$

Decreased flame temperatures lead to reduced second peaks. However, it should lead to an increased formaldehyde evolution due to its preference for cooler parts in the flame. Figures 7.51 and 7.52 represent the PG formaldehyde and LIF curves. As presented in Sections 7.2.1 and 7.3.1, the PG fuels represented mediocre temperatures, in comparison to both gasification fuels. As shown, also the formaldehyde second peaks represent themselves as modest in relation to combusted formaldehyde second peaks of GGL2 and GGL3 oxidated fuels.

7.3.3 Chemiluminescence with additional fuel side oxygen

Finally, a brief investigation regarding the CH* chemiluminescence and CH curves is presented in Figures 7.53 and 7.54. As demonstrated in Section 7.2.2, the PG fuels yielded the greatest peak intensity for a formaldehyde formation, which could imply the biggest generation of CH* / CH in regard to the compared fuels, furthermore based on the largest fraction of hydrocarbon in the fuel. This was also the case after the addition of oxygen; they are in good agreement concerning the peak intensity measurement and physical positioning. GGL3 includes the most diluent of the investigated fuels, but also 24.5 $vol.$-% of CO.

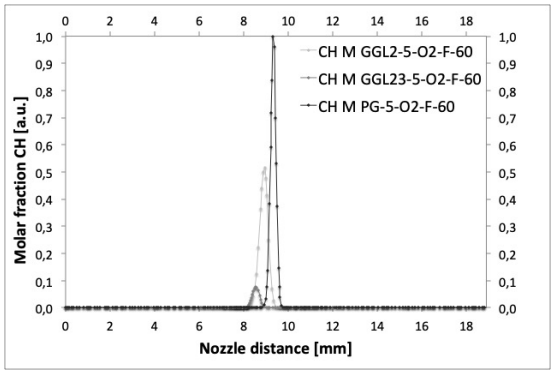

Figure 7.53: *Numerically derived CH curves with fuel mixtures of GGL2, GGL3, and PG at* $60\,cms^{-1}$ *with additional fuel side oxygen of* $5\,vol. - \%$

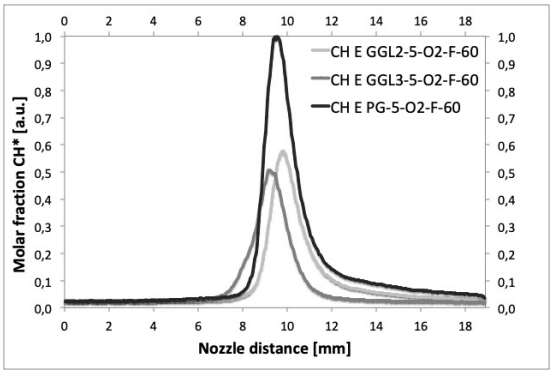

Figure 7.54: *Experimentally derived CH* chemiluminescence with fuel mixtures of GGL2, GGL3, and PG at* $60\,cms^{-1}$ *with additional fuel side oxygen of* $5\,vol. - \%$

A surplus of oxygen could have led to other chemiluminescence activities during the combustion, as discussed in Section 4.3, and therefore to the greater experimental peak. Figure 7.55 shows the peak positioning in excellent agreement for all fuels with no surplus oxygen. With oxygen added, the PG and GGL3 experimental and numerical peaks are furthermore in very good agreement. The GGL2 solutions show an off-set of more than 1 mm; this could have its origin in the significantly greater flame widths for these cases. Experimental uncertainties are $< 4.74\,\%$.

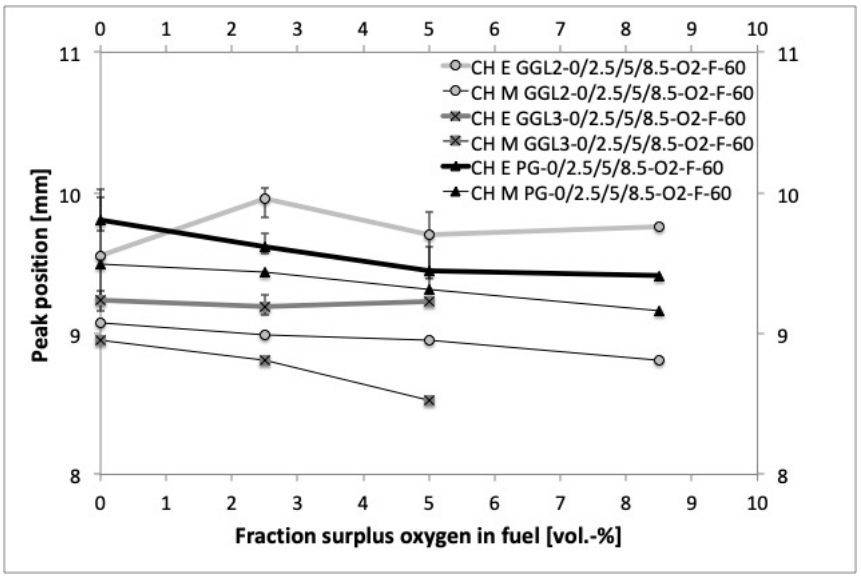

Figure 7.55: *Peak positions of experimentally and numerically derived CH* chemiluminescence and CH curves with fuel mixtures of GGL2, GGL3, and PG at* $60\,cms^{-1}$ *with additional fuel side oxygen of* $0, 2.5,\ 5,$ *and* $8.5\,vol. - \%$

7.4 Biomass-based gases with additional oxygen on the air side

In this last section of the experimental and numerical investigations, the combustion behavior of biomass-based gases with additional oxygen supplied during the combustion process on the air sides for the presented fuel compositions GGL2, GGL3, and PG is looked into, as shown in Table 5.8. Due to the experimental time-limitation in the use of the laser-laboratories of institute EVUR at Technische Universität Berlin before a relocation, some of the following investigations are entirely based on numerically derived results.

7.4.1 Temperature evolution with additional air side oxygen

The enhancement of the combustion processes, and therefore temperature evolutions, with GGL2 fuels using additional oxygen fractions of $2.5, 5,$ and 8.5 vol.-% in the oxidizer is plotted in Figure 7.56. The maximum temperature at $60\,\mathrm{cms^{-1}}$ without oxygen enhancement was $2018\,\mathrm{K}$, with fuel side oxygen enhancement of the mentioned fractions $2046, 2077,$ and $2135\,\mathrm{K}$ respectively and finally, with oxygen enrichment on the air side $2096, 2167,$ and $2253\,\mathrm{K}$ respectively.

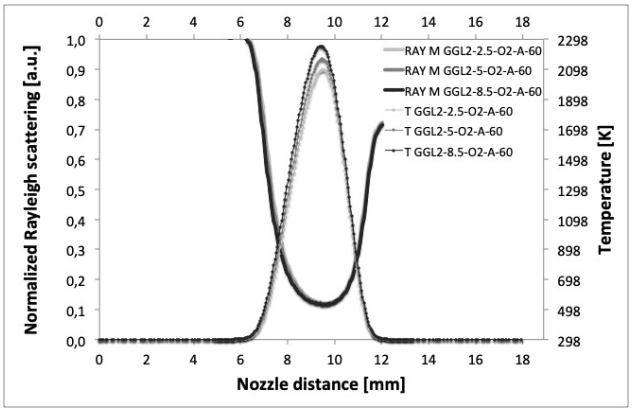

Figure 7.56: *Numerically derived Rayleigh scattering and temperature curves with fuel mixtures of GGL2 at* $60\,cms^{-1}$ *with additional air side oxygen of* 2.5, 5, *and* $8.5\,vol. - \%$

Clearly, the additional oxygen in the oxidizer had a more severe impact in terms of heat production, leading to a maximum increase of T of 11.6 % at 8.5 vol.-%. The large fraction of hydrogen in this fuel makes GGL2 prone to react willingly with any addition of oxidizer. A different reaction tendency was exhibited by the addition of oxygen to the GGL3 fuels, as pictured in Figure 7.57.

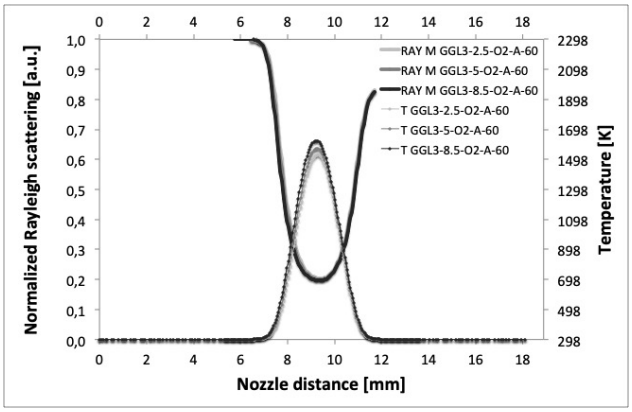

Figure 7.57: *Numerically derived Rayleigh scattering and temperature curves with fuel mixtures of GGL3 at* $60\,cms^{-1}$ *with additional air side oxygen of* 2.5, 5, *and* $8.5\,vol. - \%$

Which was expected due to the much lower peak temperature of 1484 K at 60 cms^{-1}, amongst others due to the 61 vol.-% of nitrogen in the composition. A development of 1552, 1633, and 1793 K at air side enhancement can be compared to 1530, 1571, and 1620 K at the corresponding fuel side counterpart for 2.5, 5 and 8.5 vol.-% added oxygen. GGL3 was the only fuel, where the altered fuel side had a greater impact on the temperature development. Finally, illustrated in Figure 7.58 are the corresponding temperature and Rayleigh scattering curves with additional air side oxygen of 2.5, 5, and 8.5 vol.-% for PG fuels. With an 1867, 1908, and 1977 K vs. an 1898, 1960, and 2041 K temperature evolution, in comparison to a start at 1829 K at 60 cms^{-1} without oxygen enhancement. This shows a maximum increase of T of 11.5-% at 8.5 vol.-%, possibly due to the significant fraction of carbon monoxide in the fuel.

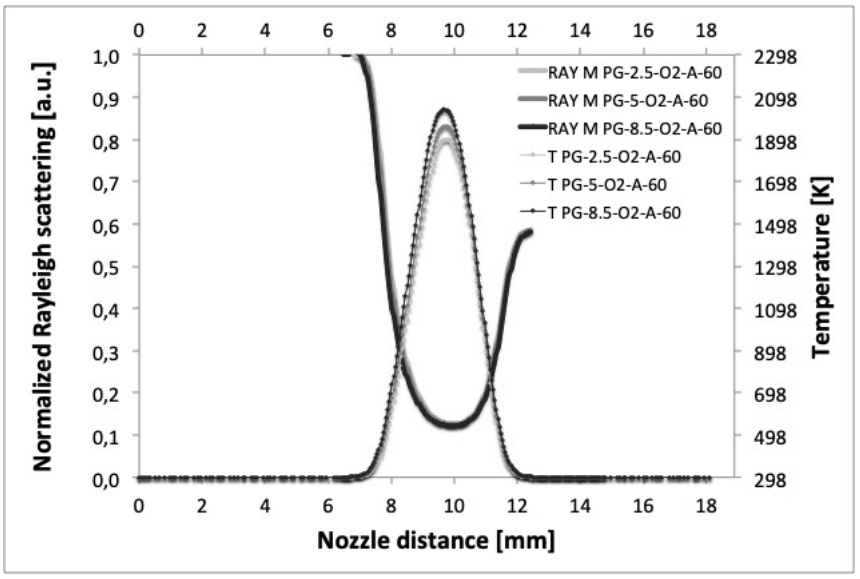

Figure 7.58: *Numerically derived Rayleigh scattering and temperature curves with fuel mixtures of PG at* $60\,cms^{-1}$ *with additional air side oxygen of* 2.5, 5, *and* $8.5\,vol.-\%$

7.4.2 Formaldehyde of biomass gases with additional air side oxygen

As previously mentioned, due to the move of the institute EVUR where these investigations took place, especially the experimental analysis could not be fulfilled as planned. This is not ideal due to the off-sets in the comparisons of the experimental and numerical solutions, as was the case in Section 7.3.2 for additional fuel side oxygen.

Remarkably, as presented in Figures 7.59 and 7.60, did the input of additional air side oxygen not have the outstanding effect on the formaldehyde evolution, as expected. In comparison to all three cases at $60\,\mathrm{cms^{-1}}$ without any fuel- or air side additions, the formaldehyde curves have only increased slightly and developed their peaks mainly on the fuel sides. In regard to the temperature evolution presented in the previous section, a decrease of the formaldehyde peak development was at least predicted for the GGL2 and PG cases due to the rise of peak temperatures for all velocities and oxygen fraction inputs investigated. The GGL3 fuels showed an increase in peak temperatures, though these were all $< 1800\,\mathrm{K}$. Therefore, an increase of the formaldehyde evolution was expected with an oxygen addition to the oxidizer.

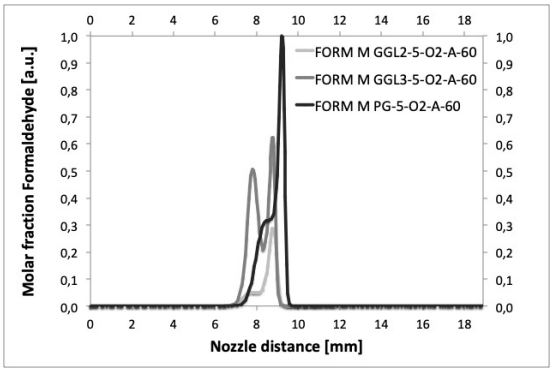

Figure 7.59: *Numerically derived formaldehyde curves with fuel mixtures of GGL2, GGL3, and PG at* $60\,cms^{-1}$ *with additional air side oxygen of* $5\,vol.-\%$

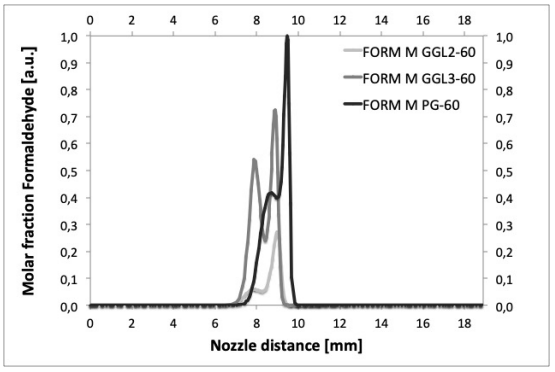

Figure 7.60: *Numerically derived formaldehyde curves with fuel mixtures of GGL2, GGL3, and PG at* $60\,cms^{-1}$ *with no additional air side oxygen*

7.4.3 Chemiluminescence with additional air side oxygen

The strongest quantitative chemiluminescence signal was measured during these additional air side enhancement experiments for the PG cases at 8.5 vol.-% oxygen feed-in. In Figures 7.61 and 7.62, once again, the numerically derived CH curves and the experimentally collected CH* chemiluminescence signals can be well compared.

As expected, the outcome for the GGL2 and PG gas compositions are in good agreement, both for the modelled and the experimental cases. The physical positioning for GGL2 is in excellent agreement; PG appears to be slightly closer to the air side. As previously presented in section 7.3.3, once again, the CH* chemiluminescence signal is multiple factors greater than its modelled counterpart for GGL3 fuels with oxygen enhancement on the air side. The physical positioning is satisfactory.

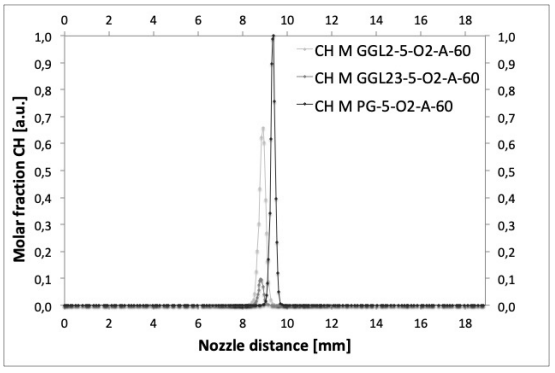

Figure 7.61: *Numerically derived CH curves with fuel mixtures of GGL2, GGL3, and PG at* $60\,cms^{-1}$ *with additional air side oxygen of* $5\,vol.-\%$

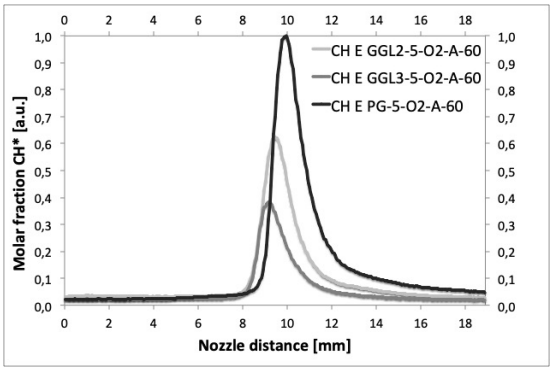

Figure 7.62: *Experimentally derived CH* chemiluminescence with fuel mixtures of GGL2, GGL3, and PG at* $60\,cms^{-1}$ *with additional air side oxygen of* $5\,vol.-\%$

7.5 Combustion behavior

The previously in this chapter presented investigations provided a suitable method to verify the structure of diluted hydrocarbon diffusion flames to furthermore show the overall agreement between numerical and experimental solutions for the newly planned and built counter-flow burner set-up. Moreover, the combustion behavior of more complex, synthetic model fuel combinations, also examining the effectiveness of the flame inhibitor oxygen, was investigated and will be summarized in the following sections.

7.5.1 Combustion behavior of diluted methane flames

By using several spectroscopic techniques, multiple possibilities arose to review the combustion behavior of diluted methane flames. Already visible to the naked eye in the laboratory was the non-stability of the combustion in regard to an adjustment of fuel- and air side velocities or dilution of the hydrocarbon fuels. These phenomena were presented by small wave-like motions of the counter-flow flames between top and bottom nozzle or straining out. Furthermore, soot production and decrease by an increase of carbon dioxide or nitrogen to the fuel composition were clearly evident, as presented in Figure 7.1.

The increase of minimum Rayleigh scattering signals for further induced diluents (up to 15 % of nitrogen or 16 % of carbon dioxide) into the fuels was expected due to the chemical, diluent, and thermal effects previously mentioned. When regarding the numerical solutions presented in Figure 7.7, an increase of scattering signal of $< 17\,\%$ was expected. The experimental investigations led to solutions of up to $< 25\,\%$. This correlates to the divergent widths of the flames and will be discussed further in Section 7.5.2.

Moreover, the evolution of formaldehyde fluorescence was clearly presented in all figures of Section 7.1.2 by a consistent trade-off of small quantities of 3 vol.-% between methane and diluent. This increase of diluent in the fuel has a more significant impact on carbon dioxide, as opposed to nitrogen, due to the fall in temperature based on the heat capacity and small contributions from radiative heat loss, which is consistent with literature.

The investigation of CH* chemiluminescence was foremost used to consider the physical positioning between fuel- and oxidizer nozzles for the experimental solutions in

comparison to their numerical models. Overall, this led to very satisfying solutions for both diluents, as presented in Figure 7.22.

7.5.2 Combustion behavior of biomass-based flames

In the following section, the combustion behavior of the regarded biomass-based flames, induced with synthetic model fuels, and the influence of oxygen enhancement on the overall performance will be the main focus.

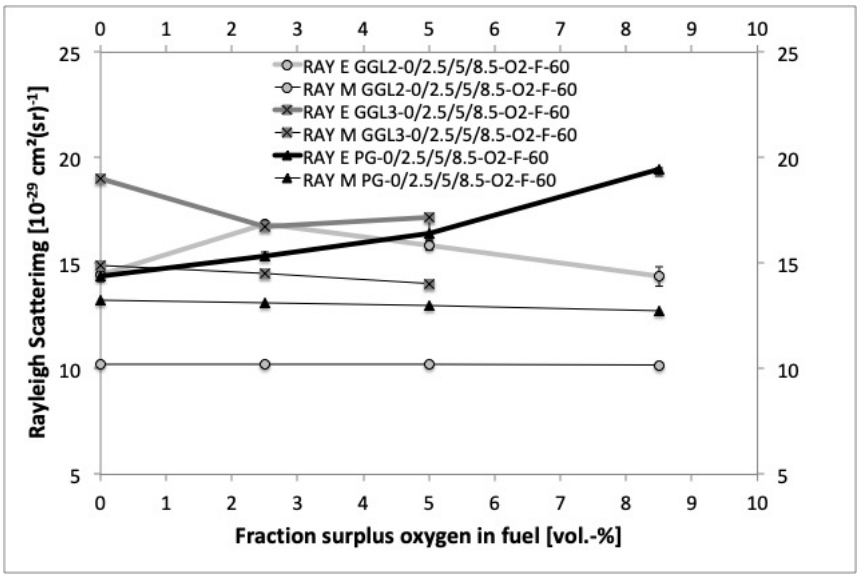

Figure 7.63: *Minimum Rayleigh scattering intensities of experimentally and numerically derived Rayleigh scattering curves with fuel mixtures of GGL2, GGL3, and PG at* $60\,cms^{-1}$ *with additional fuel side oxygen of* $0, 2.5,\ 5,$ *and* $8.5\,vol. - \%$

Figure 7.63 presents the evolution of the minimum Rayleigh scattering intensities of experimentally and numerically derived Rayleigh scattering curves with fuel mixtures of GGL2, GGL3, and PG at $60\,cms^{-1}$ with additional fuel side oxygen of $0, 2.5,\ 5,$ and $8.5\,vol.$-%. For all of the regarded fuels, the minimum peak intensities of the experimental studies were higher than their numerical counterparts, leading to deviations up to 30 %. Furthermore, the experimental uncertainties are $<$ 3.66 %. The potential large errors can have at least three origins: the inconsistencies in the flames widths, the large differences in Rayleigh cross sections for different species, and the spectroscopic set-up. The numerically modelled Rayleigh scattering is based on the expected number of different chemical species in every point of the centerline of the flame. If the numerically calculated and the experimentally measured flame widths show an aberration, the compositions of chemical species at each specific

point will have an off-set and will lead to an error in scattering intensities. Furthermore, the large differences in Rayleigh scattering cross sections for chemical species, as presented in Table 4.1, can then lead to an even larger error for a specific point in the centerline. Lastly, though the experimental uncertainties are on an acceptable level, it is difficult to detect a possible fundamental deviation in the experimental set-up due to the large number of components. The discussion of the temperature evolution during these investigations, especially in regard to the influence of oxygen enhancement on the overall behavior, will regardlessly be based on the numerical Rayleigh scattering solutions and the resulting maximum temperatures during these combustions.

The temperature evolution of the basic (no surplus oxygen) composition of biomass-based fuels was measured and modelled to be GGL2 > PG > GGL3, as presented in Figure 7.64. GGL2 included 27.2 vol.-% of hydrogen in the composition and, on the other hand, included the least amount of diluents (overall 30.4 vol.-%) in the mixture leading to 2018.20 K as peak temperature. The pyrolysis gas PG followed in regard to maximum combustion temperature with 1829.25 K, with a carbon dioxide fraction of 35 vol.-% (and no nitrogen) and 50 vol.-% of carbon monoxide. In comparison, PG has a slightly higher LHV than GGL2, as presented in 5.6. GGL3 consisted of more than double the share in diluents compared to GGL2 with 61 vol.-% of nitrogen, leading to the lowest maximum temperature at 1484.07 K.

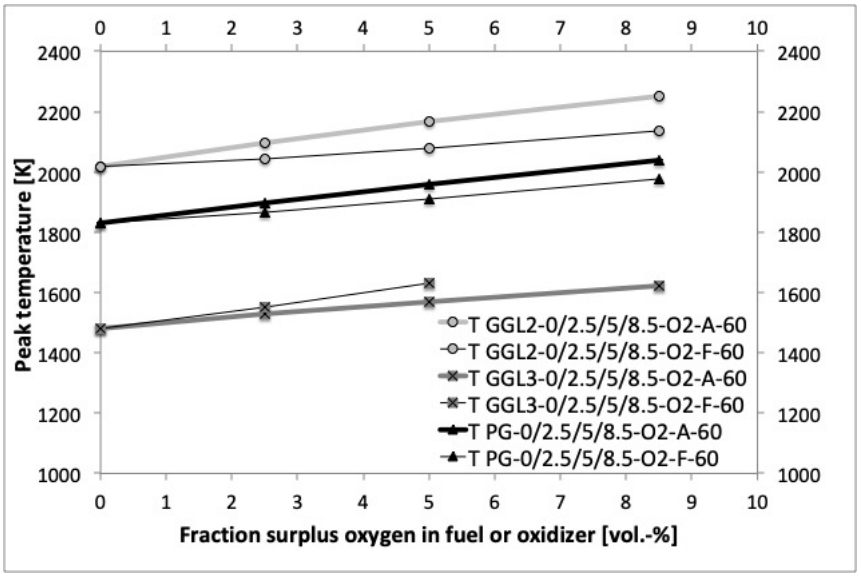

Figure 7.64: *Numerically derived maximum temperatures with fuel mixtures of GGL2, GGL3, and PG at* $60\,cms^{-1}$ *with additional fuel- and air side oxygen of* $0, 2.5, 5,$ *and* $8.5\,vol.-\%$

The oxygen enhancement of the GGL2, GGL3, and PG fuels had a significant effect on the temperature evolutions as expected, though with diverse consequences. An increase in heat development could be observed for all velocities and volume fractions of oxygen added to the fuels. A drawback of fuels from biomass-based processes is the commonly lower combustion temperatures and, therefore, heat release reductions in comparison to other (hydrocarbon) fuels. An alternative to pure oxygen as oxidizer, in terms of upgrading costs, seems to be the inclusion of small quantities of air to either the fuel- or oxidizer-sides.

Table 7.1: *Temperature evolution of GGL2 fuels with additional oxygen on fuel or air side*

GGL2	**Peak T fuel side** $[K]$	**T increase fuel side** [%]	**Peak T air side** $[K]$	**T increase air side** [%]
0% oxygen	2018.20	/	2018.20	/
5% oxygen	2077.82	2.95	2167.04	7.37
8.5% oxygen	2135.62	5.82	2252.95	11.63

Table 7.2: *Temperature evolution of GGL3 fuels with additional oxygen on fuel or air side*

GGL3	**Peak T fuel side** $[K]$	**T increase fuel side** [%]	**Peak T air side** $[K]$	**T increase air side** [%]
0% oxygen	1484.07	/	1484.07	/
5% oxygen	1632.41	9.99	1570.28	5.80
8.5% oxygen	/	/	1619.96	9.16

Table 7.3: *Temperature evolution of PG fuels with additional oxygen on fuel or air side*

PG	**Peak T fuel side** $[K]$	**T increase fuel side** [%]	**Peak T air side** $[K]$	**T increase air side** [%]
0% oxygen	1829.25	/	1829.25	/
5% oxygen	1908.04	4.30	1960.26	7.16
8.5% oxygen	1977.26	8.09	2040.08	11.53

When considering the GGL2 fuels, the oxygen enrichment on both sides led to constantly stable flames, in regard to a strain out, with a maximum temperature increase of 11.63 % at 8.5 vol.-% of oxygen enhancement on the air side. Only the lower volume fraction of oxygen added to the air side induced a slight movement of the flames towards the air side nozzle. Table 7.1 presents the temperature increase for both fuel and air side enhancement. The impact when adding oxygen to the air side was most distinctive for this fuel (T increase air side), as opposed to an

addition to the fuel side (T increase fuel side). The combustion with GGL3 fuels showed different reactions to an oxygen enhancement, as opposed to the two other fuels. First, the 8.5 vol.-% of oxygen enrichment only leads to a stable combustion for GGL3 flames when being added to the air side, as opposed to the fuel side. Second, the temperature increase is notably less when adding oxygen to the air side (7.2). PG fuels combusted very well and smooth at all oxygen enhancements, leading to slight increases in regard to the flames widths. The temperature increase on the air side is comparable to the GGL2 results; on the fuel side, the impact was much higher in comparison to GGL2, though having 4.6 vol.-% less combustible gases in the fuel, presented in Table 7.3.

For all the basic biomass-based fuels investigated, the laser-induced fluorescence measurements led to two peaks of formaldehyde in the flames. A smaller one closer to the fuel side nozzle and a larger one closer to the air side nozzle. This was confirmed in good agreement by the numerical model investigations, leading only to a dissent for the GGL3 fuels. Here the smaller peaks on the fuel side were numerically modelled to be more extensive, especially in regard to the 100 cms^{-1} velocity cases.

The diluted methane flames were thoroughly investigated with the help of a spectrograph, to demonstrate the sole detection of formaldehyde in the physical positions of the flame where it was assumed to be. These examinations hence excluded other chemical compounds at the physical positions in the flames where formaldehyde is suspected and, furthermore, confirmed the agreement between experimental and numerical data.

The oxygen enhancement in fuels and oxidizers led to consistently higher temperatures and heat distributions throughout the flames. This had evident influences on the formaldehyde positioning, as shown in sections 7.3.2 and 7.4.2. For the fuel side addition for GGL2, GGL3, and PG, a very definite region closer to the fuel side nozzle in parts of the flames with T around 1000 K, was preferred. Typically for formaldehyde, once the hotter combustion regions set in, it quickly disappears. To appear again on the other side of the flame, where cooler temperatures prevail, next to the air side nozzle.

Next to an increase of formaldehyde intensity for fuels with enhanced oxygen, the CH* chemiluminescence measurements and the CH modelling led to the rise in CH* and also CH. In comparison to the air side enhancement, which had a severe influence on the temperature in most investigated cases and also on the CH* / CH intensities, but only very moderately on the formaldehyde distribution.

7.6 Critical points

The utilization of biomass-based gases from gasification or pyrolysis for combustion processes is accompanied by multiple critical points. These are mainly based on efficiency or economic issues and are shortly presented in the following sections.

7.6.1 Gas cleaning and composition

For the experimental work done during these investigations, fuels were mixed with the use of bottled gases, a system of mass flow controllers, and a mixing chamber as presented in Section 5.1.4 and constituted as synthetic biomass-based fuels.

The mixing of precisely predefined fractions of compositions was a necessary precondition during the experimental work. When taking multiple images of flames, an experimental cycle has to run stable for at least 120 seconds, preferably longer. In Chapter 2, the different steps for differing gaseous yields during gasification or pyrolysis processes are described as dependent on process conditions. Contaminants and byproducts can primarily be minimized by optimizing the operation procedures of the system and choosing sensible properties in regard to the feedstock. In any case, this will impact the subsequent application, such as consecutive combustion processes. Furthermore, before a practical utilization of the product gases from gasification or pyrolysis of lignocellulosic biomass can be initiated, downstream gas cleaning steps have to be conducted. Particulate or gaseous impurities such as tar, nitrogenic aggregates, sulphuric compounds, particulate matters, or alkali metals need to be physically removed. Possibilities are extensive cold gas cleaning, leading to hot gas cleaning, filtration, the use of scrubbers, thermal cracking, or the utilization of sorbents or catalysts [228, 229].

Critical in these matters are the comprehensive cleaning steps, the extent of cleanliness the product gases can achieve, the attainment of a continuous product gas composition, and economic expenses that can be substantial.

7.6.2 LHV

The lower heating values of the investigated fuel compositions were presented in Chapter 5, with PG > GGL2 > GGL3 being $10.49\,\mathrm{MJ/m^3} > 9.48\,\mathrm{MJ/m^3} > 4.23\,\mathrm{MJ/m^3}$. Representing the maximum amount of heat which can be obtained from combusting these particular fuels. In comparison, the LHV of diesel, petrol, and

kerosene, are at least by factors 3-6 greater. A practical application of biomass-based gases instead of the mentioned fuels is therefore in question, due to the decrease in performance and progress, also power output and thermal efficiency.

7.6.3 Low strain rates

Lastly, the utilization of low strain rate flames in combustion will be presented shortly. Commonly known, a non-premixed flame loses heat to the lean and the rich side, as opposed to only the preheating zone, as is the case for a premixed flame. So in comparison, at the same fuel- and air side compositions and velocities, the diffusion flame extinguishes sooner due to an inflicted strain rate.

GGL2 has the maximum strain rate of the investigated fuel mixtures. For the basic mixture, a maximum for velocities of 2200 $\mathrm{cms^{-1}}$ of 4612.1 $\mathrm{s^{-1}}$ was numerically derived. This is mainly based on the high fraction of hydrogen in the fuel composition. GGL3 only has, due to the significant proportion of nitrogen, a maximum strain rate of 318.1 $\mathrm{s^{-1}}$ at fuel- and air side velocities of 148 $\mathrm{cms^{-1}}$. PG lays, as it has been for all the investigations, moderately between the two gasification gases with a maximum strain rate of 918.1 $\mathrm{s^{-1}}$ at 442 $\mathrm{cms^{-1}}$. These correspondingly low strain rates lead to issues regarding quenching and premature extinction in industrial utilizations.

Chapter 8

Summary and outlook

The aim of this investigation was to validate a model for laminar one-dimensional counter-flow diffusion flames combusting biomass-based synthetic fuels composed of N_2, H_2, CO, CO_2, CH_4, and O_2 and, furthermore, to gain a deeper understanding of the combustion behavior of these fuels with and without oxygen enhancement.

A counter-flow burner system was designed and built to perform combustion experiments. To analyze the flames, several spectroscopic techniques were applied, such as laser-induced fluorescence measurements of formaldehyde and laser-induced Rayleigh scattering. The latter was used to deduce temperature evolutions for different fuels, velocities, and compositions. Finally, CH* chemiluminescence experiments were performed, illuminating the combustion mechanisms of these biomass-based mixtures from multiple perspectives.

Moreover, multiple individual post-processing techniques were established, also within the group, and applied to finally facilitate an opportunity to practically compare the numerically calculated data with raw experimental results accurately.

Laser-induced Rayleigh scattering data were collected experimentally and processed via RAYFIT to fit the numerical data that was calculated. DIFFLA provided the chemical composition at each point of the centerline of the flames. When including the depolarization ratios and scattering cross sections for all involved chemical species, the numerically predicted Rayleigh scattering signals at the centerlines could be calculated. To calculate temperature evolutions from Rayleigh scattering data, the exact chemical composition at a measuring point is necessary. With the available experimental set-up, reproducible and accurate laser-induced Raman measurements of such kind were not feasible; thus the comparability of the numerical and experimental Rayleigh data was used for validation purposes. Finally, the temperature curves derived from the numerical model were considered.

Positioning deviations in minimum intensities were $< 0.5\,\text{mm}$ for the hydrocarbon cases, which presents an excellent agreement between numerical and experimental data. The same was the case for the biomass-based synthetic fuels, with one exception for a PG and GGL2 fuel case. The scattering intensities were consistently higher when comparing the experimental results to the model for all fuels and velocities regarded, leading to deviations of up to 30 %. None of the other experimental results from formaldehyde or chemiluminescence measurements showed such disagreements in just one direction, steadily. The root causes are based on the inconsistencies in the flames widths, the large differences in Rayleigh cross sections for different species, and the spectroscopic set-up. The flames widths were consistently up to $< 1\,\text{mm}$ broader when regarding the experimental results, leading to differences in chemical composition when comparing to numerical solutions at specific measuring points. The previously mentioned large differences in cross sections lead, furthermore, to significant discrepancies in scattering intensities between model and experiment. It is presumed that these deviations are much smaller; this can be based on the experimental results from laser-induced fluorescence measurements.

A possibility to collect the signal intensity for varying fluorescence intensities during laser-induced fluorescence measurements of formaldehyde for various fuel compositions was investigated during this investigation. Challenges occurred due to smaller and larger hydrocarbon bonds emitting fluorescence at similar wavelengths and, in addition, formaldehyde emitting not only at specific wavelengths but creating a band across $> 100\,\text{nm}$. A Boltzmann correction, as presented in Chapter 5, and a fitting of the experimental fluorescence data via CHFIT had to be carried out. DIFFLA provided the numerical solution for the formaldehyde intensity at each measuring point.

The peak developments and intensities for diluted hydrocarbon cases in regard to formaldehyde intensity, presented an excellent agreement between numerical and experimental data. Moreover, the flames widths were consistently up to $< 1\,\text{mm}$ broader, which agrees with the previous observations during the Rayleigh scattering investigations. The biomass-based synthetic fuels showed excellent agreement for the PG and GGL2 cases without an oxygen enhancement, a poorer agreement for the GGL3 cases. GGL3 included the largest fraction of diluents in the fuel, in comparison to the two other fuels, actually with an ideal temperature distribution for a formaldehyde evolution. Deviations could again have their origin in the flame widths: differing Rayleigh scattering results due to deviating widths lead to differences in temperature at a measuring point. This leads to deviations in the

Boltzmann corrections and, therefore, experimental fluorescence solutions. This interpretation could have also led to the LIF solutions for the oxygen-enhanced BDG fuels, with consistently more distinct peak separations between the multiple peaks for the experimental solutions.

In general, the laser-induced fluorescence measurements showed good agreement. Accordingly, one can assume that the experimental and numerical Rayleigh scattering solutions are not deviating up to 30 %. If the temperature evolution throughout the flames during the experiments were so deviant from the modelled solutions, the fluorescence measurements and calculations would not be so well related.

Lastly, the peak positions of the experimental CH* chemiluminescence data were compared to numerically calculated CH curves for all flames at all parameters mentioned. An off-set of physical positioning $< 0.5\,\mathrm{mm}$ again showed a very good agreement for both hydrocarbon and biomass-based synthetic fuels. Peak widths could only be regarded cautiously due to limitations of the spectroscopic measuring set-up and the therefore measured CH* solutions. The focus of the CH investigations was the validation of the modelled CH peak positioning, which is still feasible due to the close relations of the positioning of the ground and excited states of the CH radical.

Furthermore, the presented system comprised a range of flames combusting at strain rates starting at around $60\,\mathrm{s^{-1}}$, leading up to circa $250\,\mathrm{s^{-1}}$. Therefore incorporating the boundary condition at very low fuel- and oxidizer velocities for combustion, though not including the other limiting condition, at a final strain out. Diluted hydrocarbon fuels, as well as biomass-based synthetic fuels composed of multiple components, were examined based on physical positioning between the burner nozzles for all spectroscopic techniques, Rayleigh scattering minima and intensity evolutions, and laser-induced fluorescence peak maxima and intensity evolutions, leading to good agreements between modelled and experimentally derived data and therefore validating the numerical model previously developed. As far as the author is aware, such extensive characterizations between experimental and numerical investigations for these biomass-based synthetic fuels were presented for the first time in the present work.

The combustion behavior of the GGL2, GGL3, and PG fuels in regard to formaldehyde distribution, CH*/CH evolution, and Rayleigh scattering, and therefore temperature development, has been thoroughly discussed in Chapter 7. Moreover, the oxygen enhancement on fuel or oxidizer sides had a significant effect on the Rayleigh scattering intensities and formaldehyde distribution within the flames. Of

special interest were the temperature evolutions. A maximum temperature increase of 11.63 % at 8.5 vol.-% of oxygen enhancement on the air side could be reached for a GGL2 fuel. A GGL3 fuel, with the lowest LHV of all fuels regarded, reached a temperature increase of 9.99 % at 5 vol.-% of oxygen enhancement on the fuel side. An enhancement with pure oxygen or less expensive air, while accepting a higher fraction of nitrogen in the fuel, is strongly suggested for these biomass-based fuels. Leading to further utilization in industrial applications or to refine potentially problematic fuels by reducing corrosive elements.

8.1 Future work

An outlook regarding future developments of this investigation is based on multiple aspects, primarily based on the experimental set-up and the variations of process conditions.

Multiple drawbacks, based on the limitations of the available experimental test rig, can be advanced to further develop the experimental investigations. The diameters of the burner nozzles could be expanded, leading to stabilized flames and further possibilities of fuel- and oxidizer velocity increases. Conjoined with this change in burner dimension, an enlargement of the laser laboratory gas provisioning systems and safety installations would need to be undertaken.

All in all, this would present the possibility of investigating combustion processes closer to strain out circumstances. Furthermore, this could enlarge the variety of biomass-based synthetic fuels that should be investigated, for example, with higher fractions of carbon monoxide or otherwise higher simultaneous portions of oxygen and hydrogen in the fuels. An analysis of an unknown fuel mixture or possibly an online measurement directly after an industrial application seems difficult when applying measurement techniques at the current state.

The experimental spectroscopic system could be extended with further laser systems, including the possible utilization of other wavelengths to excite more chemical compounds in these hydrocarbon flames, such as OH, and therefore explore the combustion more in-depth or improve the current measurements.

The numerical solution could be expanded to include more data in regard to the buoyancy behavior of counter-flow flames and, furthermore, elaborate quenching assumptions.

Appendix A

Appendix

In the following Appendix A, additional information regarding the investigated fuels, including fuel- and oxidizer-velocities and strain rates, gases, images of the set-up, and equipment lists are presented.

A.1 Fuels

In the following section, additional information regarding the investigated fuels is listed.

Table A.1: *Investigated fuels with fuel- and oxidizer-velocities and strain rates for biomass-based mixtures*

Name of fuel	**Velocities** $[cms^{-}1]$	**Strain rates** $[s^{-}1]$
GGL2	30, 60, 100	66.1, 132.1, 220.1
GGL2-2.5-O2-F	30, 60, 100	66.1, 132.1, 220.1
GGL2-5-O2-F	30, 60, 100	66.1, 131.1, 219.1
GGL2-8.5-O2-F	30, 60, 100	65.1, 131.1, 218.1
GGL2-2.5-O2-A	30, 60, 100	66.1, 132.1, 220.1
GGL2-5-O2-A	30, 60, 100	66.1, 132.1, 220.1
GGL2-8.5-O2-A	30, 60, 100	66.1, 132.1, 220.1
GGL3	30, 60, 100	64.1, 128.1, 214.1
GGL3-2.5-O2-F	30, 60, 100	64.1, 128.1, 213.1
GGL3-5-O2-F	30, 60, 100	64.1, 128.1, 213.1
GGL3-8.5-O2-F	30, 60, 100	64.1, 128.1, 213.1
GGL3-2.5-O2-A	30, 60, 100	64.1, 129.1, 214.1
GGL3-5-O2-A	30, 60, 100	64.1, 129.1, 214.1
GGL3-8.5-O2-A	30, 60, 100	64.1, 129.1, 214.1
PG	30, 60, 100	62.1, 125.1, 208.1
PG-2.5-O2-F	30, 60, 100	62.1, 125.1, 208.1
PG-5-O2-F	30, 60, 100	62.1, 125.1, 208.1
PG-8.5-O2-F	30, 60, 100	62.1, 125.1, 208.1
PG-2.5-O2-A	30, 60, 100	62.1, 125.1, 208.1
PG-5-O2-A	30, 60, 100	62.1, 125.1, 208.1
PG-8.5-O2-F	30, 60, 100	62.1, 125.1, 208.1

Table A.2: *Investigated fuels with fuel- and oxidizer-velocities and strain rates for diluted methane mixtures*

Name of fuel	**Velocities** $[cms^{-}1]$	**Strain rates** $[s^{-}1]$
CH4-001-CO2	60	126.1
CH4-002-CO2	60	123.1
CH4-003-CO2	60	122.1
CH4-004-CO2	60	122.1
CH4-001-CO2-O2-F	60	126.1
CH4-002-CO2-O2-F	60	123.1
CH4-003-CO2-O2-F	60	122.1
CH4-004-CO2-O2-F	60	121.1
CH4-001-CO2-O2-A	60	126.1
CH4-002-CO2-O2-A	60	123.1
CH4-003-CO2-O2-A	60	122.1
CH4-004-CO2-O2-A	60	122.1
CH4-002-N2	60	134.1
CH4-003-N2	60	134.1
CH4-004-N2	60	133.1
CH4-005-N2	60	133.1
CH4-006-N2	60	132.1
CH4-007-N2	60	132.1
CH4-002-N2-O2-F	60	134.1
CH4-003-N2-O2-F	60	133.1
CH4-004-N2-O2-F	60	133.1
CH4-005-N2-O2-F	60	132.1
CH4-006-N2-O2-F	60	132.1
CH4-007-N2-O2-F	60	131.1
CH4-002-N2-O2-A	60	135.1
CH4-003-N2-O2-A	60	134.1
CH4-004-N2-O2-A	60	133.1
CH4-005-N2-O2-A	60	133.1
CH4-006-N2-O2-A	60	132.1
CH4-007-N2-O2-A	60	132.1

A.2 Experimental set-up

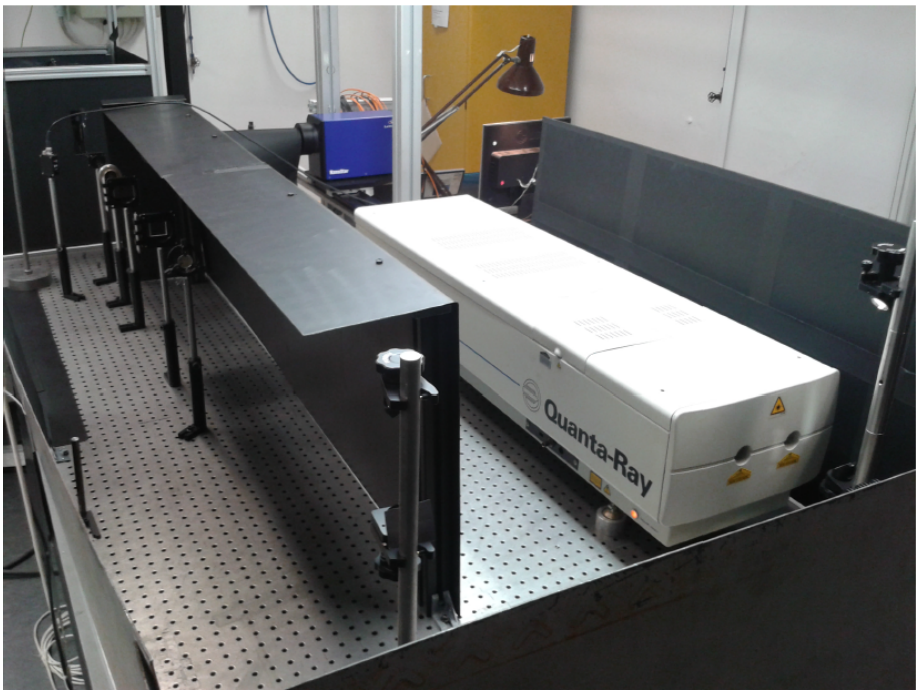

Figure A.1: *Side view of experimental set-up, including laser, periscopes, and lenses [23]*

Figure A.2: *Arrangement of the lenses as schematically represented in Figure 5.6 [23]*

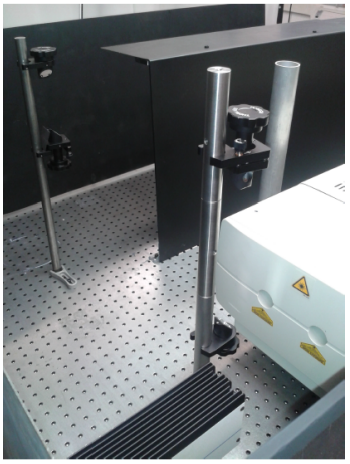

Figure A.3: *Periscopes for spectroscopic measurements [23]*

A.3 Equipment list

In the following section, the main equipment and components of the experimental measurement system, and the gases are listed.

A.3.1 Camera, energy monitor, and electrical equipment

Table A.3: *List of the main components for the spectroscopic electrical system*

Equipment	**Type**	**Manufacturer**
Nanostar ICCD camera	SN 1010630203	LaVision
Telephoto lens	EF 100mm f/2 USM	Canon
Lens	NL-3	B+W
Macro intermediate ring	DG-C	Viltrox
Online energy monitor	1108005	LaVision
System computer	1104009	LaVision
Synchronisation PTU X	1108092	LaVision
Software DaVis 8	1105106	LaVision
Powermeter	P/N 7Z01200	Ophir

A.3.2 Gas mixing

Table A.4: *List of the main components for the gas mixing system*

Equipment	**Type**	**Manufacturer**
Gas mixing chamber	Custom made	EVUR
Red-y MFC Air	GSC-C9TA-BB12	Vögtlin
Red-y MFC Nitrogen	GSC-C9TA-BB12	Vögtlin
Red-y MFC Nitrogen	GSC-C9TA-BB26	Vögtlin
Red-y MFC Methane	GSC-C9TA-BB26	Vögtlin
Red-y MFC Carbon monoxide	GSC-C9TA-BB12	Vögtlin
Red-y MFC Carbon monoxide	GSC-C9KA-BB26	Vögtlin
Red-y MFC Carbon dioxide	GSC-C9TA-BB12	Vögtlin
Red-y MFC Carbon dioxide	GSC-C9TA-BB26	Vögtlin
Red-y MFC Hydrogen	GSC-B9SA-BB23	Vögtlin
Red-y MFC Oxygen	GSC-C9TA-BB12	Vögtlin

A.3.3 Optical lenses, mirrors, filters, and equipment

Table A.5: *List of the main components for the spectroscopic system*

Equipment	**Type**	**Manufacturer**
Broadband dielectric mirror	10Q20BB.1	Newport
Planoconvexe round lens	LA4663-UV	Thorlabs
Planoconvexe round lens	LA4184-UV	Thorlabs
Planoconcave cylindrical lens	LK1743L1-A	Thorlabs
Planoconcave cylindrical lens	LJ4147-UV	Thorlabs
Planoconcave cylindrical lens	LK1419L1	Thorlabs
Heat absorption glass filter	KG-3/R500013 5101-14237	pgo/Schott
Optical glass filter	GG 385/14600171764	pgo/Schott
Neutral density filter	NE2R01A	Thorlabs
Neutral density filter	NE2R05A	Thorlabs
Neutral density filter	NE2R10A	Thorlabs
Neutral density filter	NE2R20A	Thorlabs
Brightline HC Filter	FF01-417/60	Semrock
Brightline HC Filter	FF01-523/3	Semrock
Brightline HC Filter	FF01-430/10	Semrock
Brightline HC Filter	FF01-415/10	Semrock
Periscope	RS99	Thorlabs
Kinematic holder for optics	KM100	Thorlabs
Adjustable holder for round optics	LH160C	Thorlabs
Adjustable holder for cyl. optics	CYLCP	Thorlabs
Rotatable holder for optics	RSP2C	Thorlabs
Photodetector	DET10A	Thorlabs
Polarizer	LPVISE200-A	Thorlabs

A.3.4 Gases

Table A.6: *List of the utilized gases*

Gas	**Type**	**Manufacturer**
Nitrogen	Technical, Alphagaz 2	Air Liquide
Air	Alphagaz 2	Air Liquide
Carbon monoxide	N25	Air Liquide
Hydrogen	N50	Air Liquide
Carbon dioxide	N45	Air Liquide
Methane	N55	Air Liquide
Oxygen	N55	Air Liquide

A.3.5 Counter-flow burner

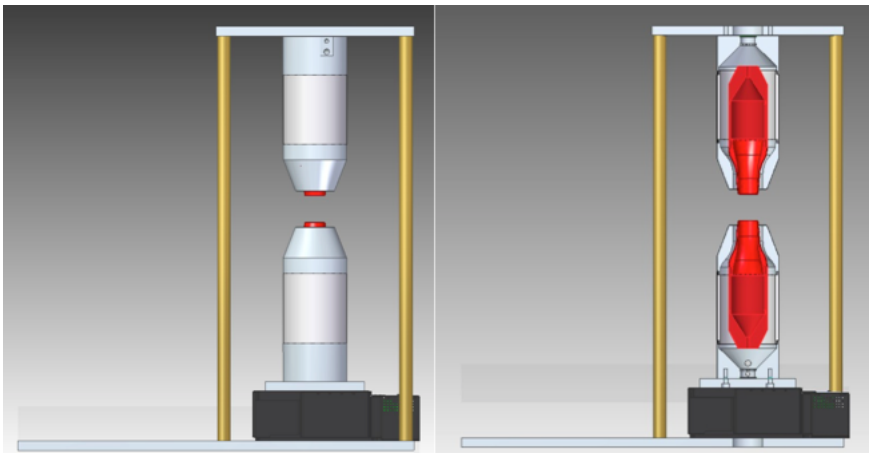

Figure A.4: *Inside and outside view of in-house built counter-flow diffusion burner*

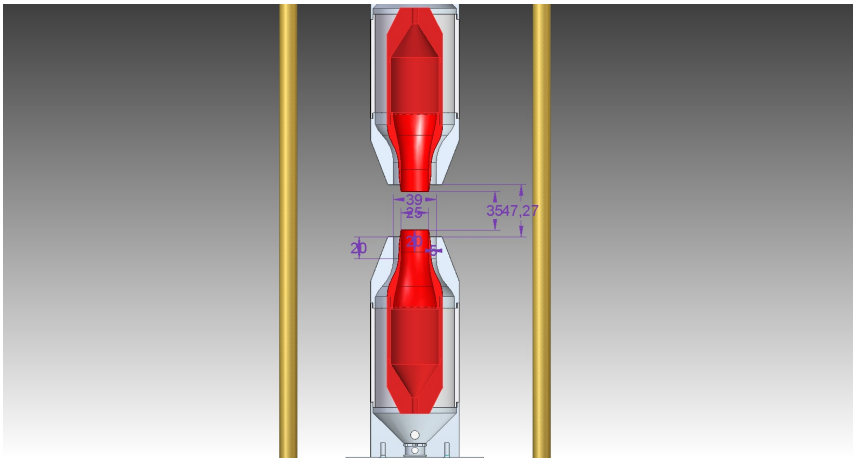

Figure A.5: *Inside view of in-house built counter-flow diffusion burner with dimensions*

Table A.7: *List of the main components for the counter-flow burner system*

Equipment	**Type**	**Manufacturer**
Motorized Translation Stage	MLJ150/M	Thorlabs

A.3.6 Laser

The Spectra Physics pulsed Nd:YAG laser Lab 150-10 was used for these investigations,

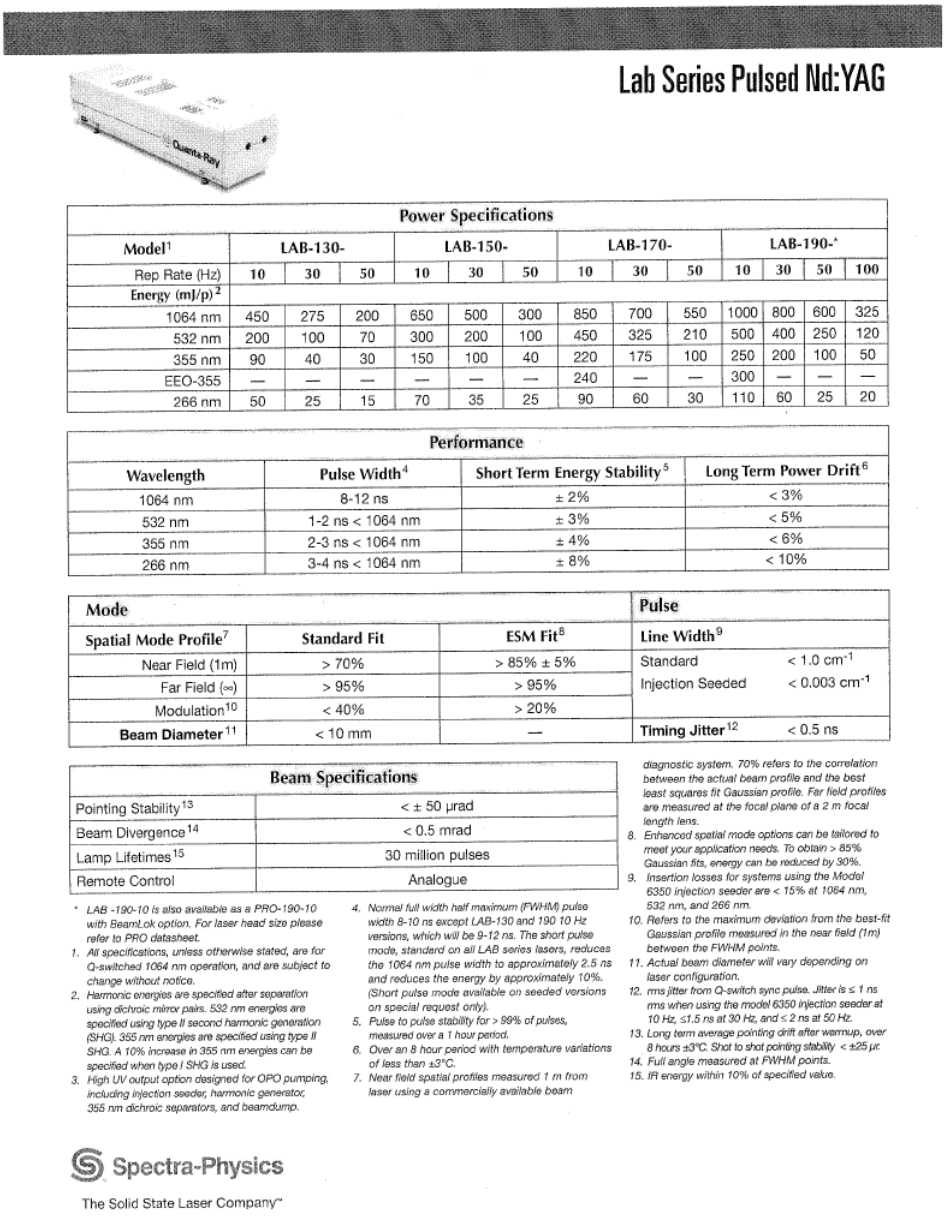

Lab Series Pulsed Nd:YAG

Power Specifications

Model[1]	LAB-130-			LAB-150-			LAB-170-			LAB-190-*			
Rep Rate (Hz)	10	30	50	10	30	50	10	30	50	10	30	50	100
Energy (mJ/p)[2]													
1064 nm	450	275	200	650	500	300	850	700	550	1000	800	600	325
532 nm	200	100	70	300	200	100	450	325	210	500	400	250	120
355 nm	90	40	30	150	100	40	220	175	100	250	200	100	50
EEO-355	—	—	—	—	—	—	240	—	—	300	—	—	—
266 nm	50	25	15	70	35	25	90	60	30	110	60	25	20

Performance

Wavelength	Pulse Width[4]	Short Term Energy Stability[5]	Long Term Power Drift[6]
1064 nm	8-12 ns	± 2%	< 3%
532 nm	1-2 ns < 1064 nm	± 3%	< 5%
355 nm	2-3 ns < 1064 nm	± 4%	< 6%
266 nm	3-4 ns < 1064 nm	± 8%	< 10%

Mode			Pulse	
Spatial Mode Profile[7]	Standard Fit	ESM Fit[8]	Line Width[9]	
Near Field (1m)	> 70%	> 85% ± 5%	Standard	< 1.0 cm^{-1}
Far Field (∞)	> 95%	> 95%	Injection Seeded	< 0.003 cm^{-1}
Modulation[10]	< 40%	> 20%		
Beam Diameter[11]	< 10 mm	—	Timing Jitter[12]	< 0.5 ns

Beam Specifications

Pointing Stability[13]	< ± 50 µrad
Beam Divergence[14]	< 0.5 mrad
Lamp Lifetimes[15]	30 million pulses
Remote Control	Analogue

* LAB -190-10 is also available as a PRO-190-10 with BeamLok option. For laser head size please refer to PRO datasheet.

1. All specifications, unless otherwise stated, are for Q-switched 1064 nm operation, and are subject to change without notice.
2. Harmonic energies are specified after separation using dichroic mirror pairs. 532 nm energies are specified using type II second harmonic generation (SHG). 355 nm energies are specified using type II SHG. A 10% increase in 355 nm energies can be specified when type I SHG is used.
3. High UV output option designed for OPO pumping, including injection seeder, harmonic generator, 355 nm dichroic separators, and beamdump.
4. Normal full width half maximum (FWHM) pulse width 8-10 ns except LAB-130 and 190 10 Hz versions, which will be 9-12 ns. The short pulse mode, standard on all LAB series lasers, reduces the 1064 nm pulse width to approximately 2.5 ns and reduces the energy by approximately 10%. (Short pulse mode available on seeded versions on special request only).
5. Pulse to pulse stability for > 99% of pulses, measured over a 1 hour period.
6. Over an 8 hour period with temperature variations of less than ±3°C.
7. Near field spatial profiles measured 1 m from laser using a commercially available beam diagnostic system. 70% refers to the correlation between the actual beam profile and the best least squares fit Gaussian profile. Far field profiles are measured at the focal plane of a 2 m focal length lens.
8. Enhanced spatial mode options can be tailored to meet your application needs. To obtain > 85% Gaussian fits, energy can be reduced by 30%.
9. Insertion losses for systems using the Model 6350 injection seeder are < 15% at 1064 nm, 532 nm, and 266 nm.
10. Refers to the maximum deviation from the best-fit Gaussian profile measured in the near field (1m) between the FWHM points.
11. Actual beam diameter will vary depending on laser configuration.
12. rms jitter from Q-switch sync pulse. Jitter is ≤ 1 ns rms when using the model 6350 injection seeder at 10 Hz, ≤1.5 ns at 30 Hz, and ≤ 2 ns at 50 Hz.
13. Long term average pointing drift after warmup, over 8 hours ±3°C. Shot to shot pointing stability < ±25 µr.
14. Full angle measured at FWHM points.
15. IR energy within 10% of specified value.

Spectra-Physics

The Solid State Laser Company™

Figure A.6: *Specifications of Spectra Physics pulsed Nd:YAG lasers [23]*

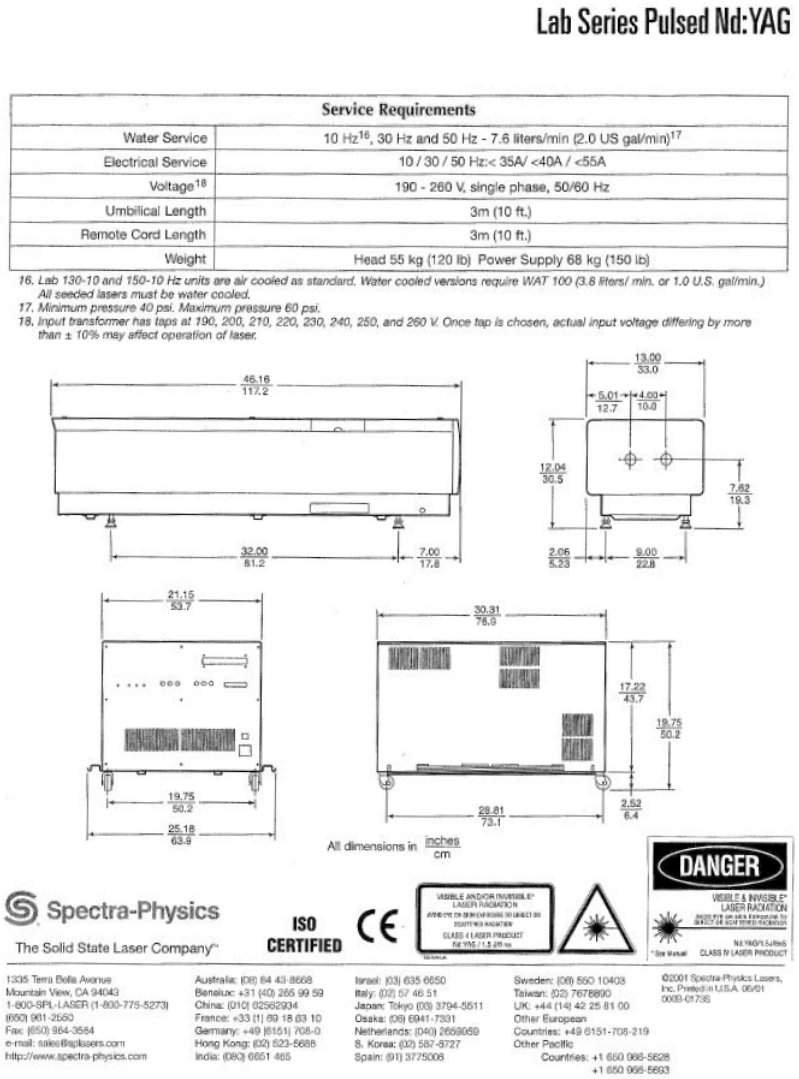

Figure A.7: *Further specifications of Spectra Physics pulsed Nd:YAG lasers [23]*

Appendix B

Publications

In the following Appendix B, publications and presentations in regard to these investigations are listed.

B.1 Peer-reviewed journals

Scharl, M.-T.; Greenhalgh, D.; Dieguez-Alonso, A.; Behrendt, F.; Numerical and Experimental Investigation of Laminar One-Dimensional Counter-Flow Flames Using Product Gas From Pyrolysis and Gasification of Woody Biomass, Eurasian Chemico-Technological Journal 20 (2018).

B.2 Presentations

Scharl, M.-T.; Greenhalgh, D.; Dieguez-Alonso, A.; Behrendt, F.; Numerical and experimental studies of laminar counter-flow diffusion flames using biomass-based gaseous fuels; DGMK-Fachbereichstagung Thermochemische Konversion – Schlüsselbaustein für zukünftige Energie-und Rohstoffsysteme, Dresden (Deutschland), 23-24. Mai 2019 - Awarded as best scientific poster of the conference

Scharl, M.-T.; Greenhalgh, D.; Dieguez-Alonso, A.; Behrendt, F.; Numerical and experimental studies of laminar counter-flow diffusion flames using biomass-based gaseous fuels; 41st Meeting of the Italian Section of the Combustion Institute, Sorrento (Italien), 23.-26. Mai 2018

Scharl, M.-T.; Greenhalgh, D.; Dieguez-Alonso, A.; Behrendt, F.; Numerical and experimental studies of laminar counter-flow diffusion flames using low-entalphy fuels; 17th International Symposium on Transport Phenomena and Dynamics of Rotating Machinery, Maui (USA), 16.-21. Dezember 2017

Bibliography

[1] S. N. Naik, V. V. Goud, P. K. Rout, and A. K. Dalai. Production of first and second generation biofuels: A comprehensive review. *Renewable and Sustainable Energy Reviews*, 14:578–597, 2010.

[2] T. Damartzis and A. Zabaniotou. Thermochemical conversion of biomass to second generation biofuels through integrated process design—A review. *Renewable and Sustainable Energy Reviews*, 15:366–378, 2011.

[3] P. McKendry. Energy production from biomass (part 2): conversion technologies. *Bioresource Technology*, 83:47–54, 2002.

[4] A. Dieguez Alonso. *Fixed-bed biomass pyrolysis: mechanisms and biochar production*. PhD thesis, Technische Universität Berlin, 2015.

[5] M. Balat. Mechanisms of Thermochemical Biomass Conversion Processes. Part 1: Reactions of Pyrolysis. *Energy Sources, Part A: Recovery, Utilization, and Environmental Effects*, 30:620–635, 2008.

[6] C. A. Koufopanos, N. Papayannakos, G. Maschio, and A. Lucchesi. Modelling of the Pyrolysis of Biomass Particles. Studies on Kinetics, Thermal and Heat Transfer Effects. *The Canadian Journal of Chemical Engineering*, 69(4):907–915, 1991.

[7] J. Cheng, editor. *Biomass to Renewable Energy Processes*. CRC Press, 2017.

[8] R. C. Brown, editor. *Thermochemical Processing of Biomass: Conversion into Fuels, Chemicals and Power*, volume 2. John Wiley and Sons, Inc., 2019.

[9] N. Peters. Fifteen Lectures on Laminar and Turbulent Combustion. Ercoftac Summer School; Aachen, Germany, 14.-28. September 1992.

[10] C. K. Law. *Combustion Physics*. Cambridge University Press, 2006.

[11] A. Mukhopadhyay and S. Sen. *Fundamentals of Combustion Engineering*. CRC Press, 2019.

[12] D. Veynante and L. Vervisch. Turbulent combustion modeling. *Progress in Energy and Combustion Science*, 28:193–266, 2002.

[13] A. E. Karatas. *High-Pressure Soot Formation and Diffusion Flame Extinction Characteristics of Gaseous and Liquid Fuels.* PhD thesis, University of Toronto, 2014.

[14] H. Tsuji. Counterflow Diffusion Flames. *Progress in Energy and Combustion Science*, 8:93–119, 1982.

[15] D. A. Skoog, F. J. Holler, and S. R. Crouch, editors. *Principles of Intrumental Analysis.* Cengage Learning, 7 edition, 2007.

[16] A. Jablonski. Efficiency of Anti-Stokes Fluorescence in Dyes. *Nature*, 131:839–840, 1933.

[17] D. C. Harris, editor. *Quantitaive Chemical Analysis.* W. H. Freeman and Company, 8 edition, 2010.

[18] B. Valeur and M. N. Berberan-Santos, editors. *Molecular Fluorescence: Principles and Applications.* Wiley-VCH Verlag, 2 edition, 2012.

[19] D. F. G. Durao, M. V. Heitor, J. H. Whitelaw, and P. O. Witze, editors. *Combusting Flow Diagnostics.* NATO ASI Series. Springer, Dordrecht, 1 edition, 1992.

[20] T. Kathrotia, U. Riedel, A. Seipel, K. Moshammer, and A. Brockhinke. Experimental and numerical study of chemiluminescent species in low-pressure flames. *Applied Physics B*, 107:571–584, 2012.

[21] M. M. Kamal. Two-line (CH^*/CO_2^*) chemiluminescence technique for equivalence ratio mapping in turbulent stratified flames. *Energy*, 192, 2020.

[22] Holthuis and Associates Flat Flame Burners. Website: www.flatflame.com; last accessed: 25.07.2021. 2013.

[23] A. Kobusinski. Aufbau und Einsatz eines Laser-Diagnostik-Systems zur spektroskopischen Untersuchung des Verbrennungsverhaltens gasförmiger Brennstoffe in laminaren Flammen. Master's thesis, Technische Universität Berlin, 2015.

[24] W. Radloff. *Laser in Wissenschaft und Technik.* Spektrum Akademischer Verlag, 2010.

[25] LaVision GmbH. *Nanostar Camera System Operation Manual.* LaVision GmbH, 1999.

[26] D. C. Kyritsis, V. S. Santoro, and A. Gomez. The effect of temperature correction on the measured thickness of formaldehyde zones in diffusion flames for 355 nm excitation. *Experiments in Fluids*, (37):769–772, 2004.

[27] Spectra Physics. *Quanta-Ray Lab-Series - pulsed Nd:YAG Lasers*. Spectra Physics, 1335 Terra Bella Avanue; Mountain View, CA 94043, June 2003.

[28] P. Basu. *Biomass Gasification and Pyrolysis: Practical Design*. Academic Press, 2010.

[29] D. L. Klass. *Biomass for Renewable Energy, Fuels, and Chemicals*. Academic Press, 1 edition, 1998.

[30] M. Brebu and C. Vasile. Thermal Degradation of Lignin — A Review. *Cellulose Chemistry and Technology*, 44(9):353–363, 2010.

[31] P. McKendry. Energy production from biomass (part 3): gasification technologies. *Bioresource Technology*, 83:55–63, 2002.

[32] J. Warnatz, U. Maas, and R.W. Dibble. *Combustion: Physical and Chemical Fundamentals, Modeling and Simulation, Experiments, Pollutant Formation*. Springer, 4 edition, 2006.

[33] K. Seshadri and N. Peters. Asymptotic Structure and Extinction of Methane-Air Diffusion Flames. *Combustion and Flame*, 73:23–44, 1988.

[34] G. Sutton, A. Levick, G. Edwards, and D. Greenhalgh. A combustion temperature and species standard for the calibration of laser diagnostic techniques. *Combustion and Flame*, 147:39–48, 2006.

[35] Energy Union. Website: https://ec.europa.eu/energy/topics/energy-strategy/energy-union; last accessed: 25.07.2021. 06 2020.

[36] M. Ringel. Fostering the use of renewable energies in the European Union: the race between feed-in tariffs and green certificates. *Renewable Energy*, 31:1–17, 2006.

[37] R. F. Sawyer. Science based policy for addressing energy and environmental problems. *Proceedings of the Combustion Institute*, 32:45–56, 2009.

[38] N. Peters. *Turbulent Combustion*. Cambridge University Press, 2000.

[39] N. Peters. Laminar flamelet concepts in turbulent combustion. *Twenty-first Symposium (International) on Combustion / The Combustion Institute*, pages 1231–1250, 1988.

[40] E. N. Kalogirou. *Waste-to-Energy Technologies and Global Applications*. CRC Press by Taylor and Francis Group, 2018.

[41] P. McKendry. Energy production from biomass (part 1): overview of biomass. *Bioresource Technology*, 83:37–46, 2002.

[42] A. Pandey, C. Larroche, S. C. Ricke, C.-G. Dussap, and E. Gnansounou, editors. *Biofuels, Alternative Feedstocks and Conversion Processes*. Academic Press, 1 edition, 2011.

[43] A. Mohr and S. Raman. Lessons from first generation biofuels and implications for the sustainability appraisal of second generation biofuels. *Energy Policy*, 63:114–122, 2013.

[44] M. A. Carriquiry, X. Du, and G. R. Timilsina. Second generation biofuels: Economics and policies. *Energy Policy*, 39:4222–4234, 2011.

[45] V. B. Agbor, N. Cicek, R. Sparling, A. Berlin, and D. B. Levin. Biomass pretreatment: Fundamentals toward application. *Biotechnology Advances*, 29:675–685, 2011.

[46] L. C. R. Sá, L. M. E. F. Loureiro, L. J. R. Nunes, and A. M. M. Mendes. Torrefaction as a Pretreatment Technology for Chlorine Elimination from Biomass: A Case Study Using Eucalyptus globulus Labill. *Resources*, 9(54), 2020.

[47] C. Liu, B. Yan, G. Chen, and X. S. Bai. Structures and burning velocity of biomass derived gas flames. *International Journal of Hydrogen Energy*, 35(542-555), 2010.

[48] M. A. Leon, Md. M. Rahman, and S. C. Bhattacharya. A Study on Improved Biomass Briquetting. *Energy for Sustainable Development*, 6:67–71, 2002.

[49] R. Razuan, K. N. Finney, Q. Chen, V. N. Sharifi, and J. Swithenbank. Pelletised fuel production from palm kernel cake. *Fuel Processing Technology*, 92:609–615, 2011.

[50] A. Faaij. Modern Biomass Conversion Technologies. *Mitigation and Adaptation Strategies for Global Change*, 11:343–375, 2006.

[51] H. B. Goyal, D. Seal, and R. C. Saxena. Bio-fuels from thermochemical conversion of renewable sources: A review. *Renewable and Sustainable Energy Reviews*, 12:504–517, 2008.

[52] M. Crocker, editor. *Thermochemical Conversion of Biomass to Liquid Fuels and Chemicals*. Royal Society of Chemistry, 2010.

[53] H. Chen, editor. *Lignocellulose Biorefinery Engineering: Principles and Applications*. Woodhead Publishing Limited, 2015.

[54] D. Mohan, C. U. Pittman Jr., and P. H. Steele. Pyrolysis of Wood/Biomass for Bio-oil: A Critical Review. *Energy and Fuels*, 20:848–889, 2006.

[55] P. A. Horne and P. T. Williams. Influence of temperature on the products from the flash pyrolysis of biomass. *Fuel*, 75:1051–1059, 1996.

[56] L. Zhang, C. Xu, and P. Champagne. Overview of recent advances in thermochemical conversion of biomass. *Energy Conversion and Management*, 51:969–982, 2010.

[57] A. Demirbas. Current Technologies for the Thermo-Conversion of Biomass into Fuels and Chemicals. *Energy Sources*, 26:715–730, 2004.

[58] M. Balat. Mechanisms of Thermochemical Biomass Conversion Processes. Part 2: Reactions of Gasification. *Energy Sources, Part A: Recovery, Utilization, and Environmental Effects*, 30:636–648, 2008.

[59] H. Juentgen. Reactivities of carbon to steam and hydrogen and applications to technical processes — A review. *Carbon*, 19:167–173, 1981.

[60] J. Mathieu and J. Scott. *An Introduction to Turbulent Flow.* Cambridge University Press, 2000.

[61] P. A. Davidson. *Turbulence, An Introduction for Scientists and Engineers.* Oxford University Press, 2004.

[62] B. Rehm, J. Schubert, A. Haghshenas, A. S. Paknejad, and J. Hughes, editors. *Managed Pressure Drilling.* Gulf Publishing Company, 2008.

[63] S. R. Turns. *An Introduction to Combustion: Concepts and Applications.* Mcgraw-Hill Professional, 2000.

[64] K. K. Kuo. *Principles of Combustion.* John Wiley and Sons, Inc., 2005.

[65] N. Kubota. *Propellants and Explosives: Thermochemical Aspects of Combustion.* Wiley-VCH, 2015.

[66] J. C. Kloppers and D. G. Kroeger. The Lewis factor and its influence on the performance prediction of wet-cooling towers. *International Journal of Thermal Sciences*, pages 879–884, 2005.

[67] B. J. Isaac, A. Parente, C. Galletti, J. N. Thornock, P. J. Smith, and L. Tognotti. A Novel Methodology for Chemical Time Scale Evaluation with Detailed Chemical Reaction Kinetics. *Energy and Fuels*, 27:2255–2265, 2013.

[68] F. Tat Cheong Yuen. *Experimental Investigation of the Dynamics and Structure of Lean-Premixed Turbulent Combustion.* PhD thesis, University of Toronto, 2009.

[69] K. K. Kuo and R. Acharya. *Fundamentals of Turbulent and Multiphase Combustion.* John Wiley and Sons, Inc., 2012.

[70] N. Peters. Four Lectures on Turbulent Combustion. Ercoftac Summer School; Aachen, Germany, 15.-19. September 1997.

[71] C. Noehre, M. Andersson, B. Johansson, and A. Hultqvist. Characterization of Partially Premixed Combustion. Powertrain and Fluid Systems Conference and Exhibition; Toronto, Canada, 16.-19. October 2006.

[72] P. Clavin and G. Searby. *Combustion Waves and Fronts in Flows: Flames, Shocks, Detonations, Ablation Fronts and Explosion of Stars*. Cambridge University Press, 2016.

[73] F. A. Williams and S. C. Li. Some Basic Considerations of Pollutant Emission and Knock in Internal Combustion Engines. SAE 2000 World Congress; Detroit, USA, 6.-9. March 2000.

[74] H. Tsuji and I. Yamaoka. The counterflow diffusion flame in the forward stagnation region of a porous cylinder. *Symposium (International) on Combustion*, 11:979–984, 1967.

[75] M. D. Smooke, I. K. Puri, and K. Seshadri. A comparison between numerical calculations and experimental measurements of the structure of a counterflow diffusion flame burning diluted methane in diluted air. *Symposium (International) on Combustion*, 21:1783–1792, 1988.

[76] M. D. Smooke, R. A. Yetter, T. P. Parr, D. M. Hanson-Parr, M. A. Tanoff, M. B. Colket, and R. J. Hall. Computational and experimental study of ammonium perchlorate/ethylene counterflow diffusion flames. *Proceedings of the Combustion Institute*, 28:2013–2020, 2000.

[77] I. K. Puri, K. Seshadri, M. D. Smooke, and D. Keyes. A Comparison Between Numerical Calculations and Experimental Measurements of the Structure of a Counterflow Methane-Air Diffusion Flame. *Combustion Science and Technology*, 56:1–22, 1987.

[78] K. Seshadri, C. Trevino, and M. D. Smooke. Analysis of the structure and mechanisms of extinction of a counterflow methanol-air diffusion flame. *Combustion and Flame*, 76:111–132, 1989.

[79] G. Amantini, J. H. Frank, M. D. Smooke, and A. Gomez. Computational and experimental study of steady axisymmetric non-premixed methane counterflow flames. *Combustion Theory and Modelling*, 11:47–72, 2007.

[80] L. Figura and A. Gomez. Laminar counterflow steady diffusion flames under high pressure ($P \leq 3$ MPa) conditions. *Combustion and Flame*, 159:142–150, 2012.

[81] T. Poinsot and D. Veynante. *Theoretical and Numerical Combustion*. R.T. Edwards Inc., 2005.

[82] K. Seshadri and F. A.Williams. Laminar flow between parallel plates with injection of a reactant at high reynolds number. *International Journal of Heat and Mass Transfer*, 21:251–253, 1978.

[83] H. Tsuji and I. Yamaoka. Structure analysis of counterflow diffusion flames in the forward stagnation region of a porous cylinder. *Symposium (International) on Combustion*, 13:723–731, 1971.

[84] T. P. Pandya and F. J. Weinberg. The structure of flat, counter-flow diffusion flames. *Proceedings of the Royal Society of London*, 279:544–561, 1964.

[85] A. E. Karatas. Soot Formation in Co-flow and Counterflow Laminar Diffusion Flames of Fuel Mixtures. Master's thesis, University of Toronto, 2009.

[86] R. Borghi and S. N. B. Murthy. *Turbulent Reactive Flows*. Springer-Verlag New York Inc., 1989.

[87] K. Bray. Laminar Flamelets in Turbulent Combustion Modeling. *Combustion Science and Technology*, 188(9):1372–1375, June 2016.

[88] C. Meneveau and T. Poinsot. Stretching and Quenching of Flamelets in Premixed Turbulent Combustion. *Combustion and Flame*, pages 311–332, 1991.

[89] J. A. van Oijen, R. J. M. Bastiaans, G. R. A. Groot, and L. P. H. de Goey. Direct Numerical Simulations of Premixed Turbulent Flames with Reduced Chemistry: Validation and Flamelet Analysis. *Flow, Turbulence and Combustion*, 75:67–84, 2005.

[90] H. Pitsch. A consistent level set formation for large-eddy simulation of premixed turbulent combustion. *Combustion and Flame*, 143:587–598, 2005.

[91] M. Ihme, L. Shunn, and J. Zhang. Regularization of reaction progress variable for application to flamelet-based combustion models. *Journal of Computational Physics*, 231:7715–7721, 2012.

[92] F. Halter, F. Foucher, L. Landry, and C. Mounaim-Rousselle. Effect of Dilution by Nitrogen and/or Carbon Dioxide on Methane and Iso-Octane Air Flames. *Combustion Science and Technology*, 181:813–827, 2009.

[93] M. Elia, M. Ulinski, and M. Metghalchi. Laminar Burning Velocity of Methane-Air-Diluent Mixtures. *Journal of Engineering for Gas Turbines and Power*, pages 190–196, 2001.

[94] R. Glowinski, B. Larrouturou, and R. Temam. *Numerical Simulation of Combustion Phenomena*. Springer, May 1985.

[95] K. Seshadri and N. Peters. The inner structure of methane-air flames. *Combustion and Flame*, 81:96–118, 1990.

[96] W. P. Jones and R. P. Lindstedt. Global reaction schemes for hydrocarbon combustion. *Combustion and Flame*, 73:233–249, 1988.

[97] D. J. Hucknall. *Chemistry of Hydrocarbon Combustion*. Chapman and Hall, 1985.

[98] C.-H. Hwang, C. B. Oh, and C.-E. Lee. Effects of CO_2 dilution on the interactions of a CH_4-air nonpremixed jet flame with a single vortex. *International Journal of Thermal Sciences*, 48:1423–1431, 2009.

[99] A. E. Karatas and Ö. L. Gülder. Effects of carbon dioxide and nitrogen addition on soot processes in laminar diffusion flames of ethylene-air at high pressures. *Fuel*, 200:76–80, 2017.

[100] D. X. Du, R. L. Axelbaum, and C. K. Law. The influence of carbon dioxide and oxygen as additives on soot formation in diffusion flames. *Twenty-Third Symposium (International) on Combustion / The Combustion Institute*, pages 1501–1507, 1990.

[101] C. Serrano, J. J. Hernandez, C. Mandilas, C. G. W. Sheppard, and R. Woolley. Lamniar burning behaviour of biomass gasification-derived producer gas. *International Journal of Hydrogen Energy*, 33:851–862, 2008.

[102] T. Hanaoka, S. Inoue, S. Uno, T. Ogi, and T. Minowa. Effect of woody biomass components on air-steam gasification. *Biomass and Bioenergy*, 28:69–76, 2005.

[103] P. Lv, Z. Yuan, L. Ma, C. Wu, Y. Chen, and J. Zhu. Hydrogen-rich gas production from biomass air and oxygen/steam gasification in a downdraft gasifier. *Renewable Energy*, 32:2173–2185, 2007.

[104] K. Stahl and M. Neergaard. IGCC power plant for biomass utilisation, varnamo, sweden. *Biomass and Bioenergy*, 15:205–211, 1998.

[105] FAO (Food and Agricultural Organization of the United Nations). Wood gas as engine fuel. FAO Forestry Papers 72, 1986.

[106] C. Dupont, J.-M. Commandre, P. Gauthier, G. Boissonnet, S. Salvador, and D. Schweich. Biomass pyrolysis experiments in an analytical entrained flow reactor between 1073 K and 1273 K. *Fuel*, 87:1155–1164, 2008.

[107] J. Lede, F. Broust, F.-T. Ndiaye, and M. Ferrer. Properties of bio-oils produced by biomass fast pyrolysis in a cyclone reactor. *Fuel*, 86:1800–1810, 2007.

[108] H. Luik, I. Johannes, V. Palu, L. Luik, and K. Kruusement. Transformations of biomass internal oxygen at varied pyrolysis conditions. *Journal of Analytical and Applied Pyrolysis*, 79:121–127, 2007.

[109] A. K. Hossain and P. A. Davies. Pyrolysis liquids and gases as alternative fuels in internal combustion engines — A review. *Renewable and Sustainable Energy Reviews*, 21:165–189, 2013.

[110] J. Rezaiyan and N. P. Cheremisinoff, editors. *Gasification Technologies: A Primer for Engineers and Scientists*. CRC Press by Taylor and Francis Group, 2005.

[111] M. Balat. Gasification of Biomass to Produce Gaseous Products. *Energy Sources, Part A: Recovery, Utilization, and Environmental Effects*, 31:516–526, 2009.

[112] H. A. Yepes and A. A. Amell. Laminar burning velocity with oxygen-enriched air of syngas produced from biomass gasification. *International Journal of Hydrogen Energy*, 38:7519–7527, 2013.

[113] H. Bockhorn, F. Fetting, and H. W. Wenz. Investigation of the Formation of High Molecular Hydrocarbons and Soot in Premixed Hydrocarbon-Oxygen Flames. *Berichte der Bunsengesellschaft Für Physikalische Chemie*, 87:1067–1073, 1983.

[114] P. Baskar and A. Senthilkumar. Effects of oxygen enriched combustion on pollution and performance characteristics of a diesel engine. *Engineering Science and Technology, an International Journal*, 2015.

[115] M. Alden, J. Bood, Z. Li, and M. Richter. Visualization and understanding of combustion processes using spatially and temporally resolved laser diagnostic techniques. *Proceedings of the Combustion Institute*, 33:69–97, 2011.

[116] Z. Yang, X. Yu, J. Peng, and J. Zhang. *Laser Technology and its Applications*, chapter 5. IntechOpen, 2019.

[117] M. Baudelet, editor. *Laser spectroscopy for sensing: Fundamentals, Techniques and Applications*. Woodhead Publishing Limited, 2014.

[118] D. Frackowiak. The Jablonski diagram. *Journal of Photochemistry and Photobioligy*, 2:399–408, 1988.

[119] J. Zimmermann, A. Zeug, and B. Röder. A generalization of the Jablonski diagram to account for polarization and anisotropy effects in time-resolved experiments. *Physical Chemistry Chemical Physics*, 5:2964–2969, 2003.

[120] H. H. Telle, A. Gonzalez Urena, and R. J. Donovan, editors. *Laser Chemistry: Spectroscopy, Dynamics and Applications*. John Wiley and Sons, Inc., 2007.

[121] W. W. Parson, editor. *Modern Optical Spectroscopy: With Exercises and Examples from Biophysics and Biochemistry*. Springer, 2 edition, 2015.

[122] P. Atkins and R. Friedman, editors. *Molecular Quantum Mechanics*. Oxford University Press, 4 edition, 2005.

[123] J. R. Lakowicz, editor. *Principles of Fluorescence Spectroscopy*. Springer, 3 edition, 2006.

[124] F.-Q. Zhao and H. Hiroyasu. The applications of laser Rayleigh scattering to combustion diagnostics. *Progress in Energy and Combustion Science*, 19:447–485, 1993.

[125] R. B. Miles, W. R. Lempert, and J. N. Forkey. Laser Rayleigh scattering. *Measurement Science and Technology*, 12:33–51, 2001.

[126] R. Thalman, K. J. Zarzana, M. A. Tolbert, and R. Volkamer. Rayleigh scattering cross-section measurements of nitrogen, argon, oxygen and air. *Journal of Quantitative Spectroscopy and Radiative Transfer*, 2014.

[127] W. C. Gardiner Jr., Y. Hidaka, and T. Tanzawa. Refractivity of Combustion Gases. *Combustion and Flame*, 40:213–219, 1981.

[128] J. Fielding, J. H. Frank, S. A. Kaiser, M. D. Smooke, and M. B. Long. Polarized/depolarized Rayleigh scattering for determining fuel concentrations in flames. *Proceedings of the Combustion Institute*, 29:2703–2709, 2002.

[129] C. H. Kautz, P. R. L. Heron, M. E. Loverude, and L. C. McDermott. Student understanding of the ideal gas law, Part I: A macroscopic perspective. *American Journal of Physics*, 73:1055–1063, 2005.

[130] J. A. Sutton and J. F. Driscoll. Rayleigh scattering cross sections of combustion species at 266, 355, and 532 nm for thermometry applications. *Optics Letters*, 29(22):2620–2622, 2004.

[131] A. M. Garcia-Campana and W. R. G. Baeyens, editors. *Chemiluminescence in Analytical Chemistry*. Marcel Dekker Inc., 2001.

[132] C. Dodeigne, L. Thunus, and R. Lejeune. Chemiluminescence as diagnostic tool. A review. *Talanta*, 51:415–439, 2000.

[133] V. N. Nori and J. M. Seitzman. CH* chemiluminescence modeling for combustion diagnostics. *Proceedings of the Combustion Institute*, 32:895–903, 2009.

[134] V. N. Nori and J. M. Seitzman. Evaluation of Chemiluminescence as a Combustion Diagnostic under Varying Operating Conditions. 46th AIAA Aerospace Sciences Meeting and Exhibit; Reno, USA, 7.-10. January 2008.

[135] K. T. Walsh, M. B. Long, M. A. Tanoff, and M. D. Smooke. Experimental and computational study of CH, CH*, and OH* in an axisymmetric laminar diffusion flame. *Symposium (International) on Combustion*, 27:615–623, 1998.

[136] M. De Leo, A. Saveliev, L. A. Kennedy, and S. A. Zelepouga. OH and CH luminescence in opposed flow methane oxy-flames. *Combustion and Flame*, 149:435–447, 2007.

[137] P. Nau, J. Krüger, A. Lackner, M. Letzgus, and A. Brockhinke. On the quantification of OH*, CH*, and C_2* chemiluminescence in flames. *Applied Physics B*, 107:551–559, 2012.

[138] A. G. Gaydon and H. G. Wolfhard. *Flames: Their Structure, Radiation, and Temperature*. Chapman and Hall, 4 edition, 1979.

[139] G. P. Glass, G. B. Kistiakowsky, J. V. Michael, and H. Niki. The oxidation reactions of acetylene and methane. *Symposium (International) on Combustion*, 10:513–522, 1965.

[140] J. M. Hall, J. de Vries, A. R. Amadio, and E. L. Petersen. Towards a Kinetics Model of CH Chemiluminescence. 43rd AIAA Aerospace Sciences Meeting and Exhibit; Reno, USA, 10.-13. January 2005.

[141] R. M. I. Elsamra, S. Vranckx, and S. A. Carl. CH(A2Delta) Formation in hydrocarbon combustion: the temperature dependence of the rate constant of the reaction $C_2H + O_2 \rightarrow$CH(A2Delta) + CO_2 . *The Journal of Physical Chemistry A*, 109, 2005.

[142] G. P. Smith; J. Luque; C. Park; J. B. Jeffries; D. R. Crosley. Low pressure flame determinations of rate constants for OH(A) and CH(A) chemiluminescence. *Combustion and Flame*, 131:59–69, 2002.

[143] G. P. Smith, C. Park, and J. Luque. A note on chemiluminescence in low-pressure hydrogen and methane–nitrous oxide flames. *Combustion and Flame*, 140:385–389, 2005.

[144] S. Karnani and D. Dunn-Rankin. Visualizing CH* chemiluminescence in sooting flames. *Combustion and Flame*, 160:2275–2278, 2013.

[145] C. S. Panoutsos, Y. Hardalupas, and A. M. K. P. Taylor. Numerical evaluation of equivalence ratio measurement using OH* and CH* chemiluminescence in premixed and non-premixed methane–air flames. *Combustion and Flame*, 156:273–291, 2009.

[146] D. Giassi, S. Cao, B. A. V. Bennett, D. P. Stocker, F. Takahashi, M. D. Smooke, and M. B. Long. Analysis of CH* concentration and flame heat release rate in laminar coflow diffusion flames under microgravity and normal gravity. *Combustion and Flame*, 167:198–206, 2016.

[147] A. Hossain and Y. Nakamura. A numerical study on the ability to predict the heat release rate using CH* chemiluminescence in non-sooting counterflow diffusion flames. *Combustion and Flame*, 161:162–172, 2014.

[148] T. F. Guiberti, D. Durox, and T. Schuller. Flame chemiluminescence from CO_2 - and N_2-diluted laminar CH_4/air premixed flames. *Combustion and Flame*, 181:110–122, 2017.

[149] R. Klein and L. J. Schoen. Role of Formaldehyde in Combustion. *Literature of the Combustion of Petroleum*, pages 58–68, 1958.

[150] C. Brackmann, J. Nygren, X. Bai, Z. Li, H. Bladh, B. Axelsson, I. Denbratt, L. Koopmans, P.-E. Bengtsson, and M. Alden. Laser-induced fluorescence of formaldehyde in combustion using third harmonic Nd:YAG laser excitation. *Spectrochimica Acta Part A*, 59:3347–3356, 2003.

[151] B. Lewis and G. von Elbe, editors. *Combustion, Flames and Explosions of Gases*. Academic Press Inc., 3 edition, 1987.

[152] X. Bai, T. Metz, F. Ossler, and M. Alden. Absorption of formaldehyde (H_2CO) in the $\tilde{A}^1A_2 \leftarrow \tilde{X}^1A_1$ band system at elevated temperatures and pressures. *Spectrochimica Acta Part A*, 60:821–828, 2004.

[153] T. Metz, X. Bai, F. Ossler, and M. Alden. Fluorescence lifetimes of formaldehyde (H_2CO) in the $\tilde{A}^1A_2 \rightarrow \tilde{X}^1A_1$ band system at elevated temperatures and pressures. *Spectrochimica Acta Part A*, 60:1043–1053, 2004.

[154] J. Kiefer, Z. S. Li, T. Seeger, A. Leipertz, and M. Alden. Planar laser-induced fluorescence of HCO for instantaneous flame front imaging in hydrocarbon flames. *Proceedings of the Combustion Institute*, 32:921–928, 2009.

[155] K. Bijjula and D. C. Kyritsis. Experimental evaluation of flame observables for simplified scalar dissipation rate measurements in laminar diffusion flamelets. *Proceedings of the Combustion Institute*, 30:493–500, 2005.

[156] K. R. Gosselin, W. F. Carnell Jr., and M. W. Renfro. Formaldehyde Fluorescence as a Marker for Scalar Dissipation Through Local Extinction. *Combustion Science and Technology*, 187:1742–1758, 2015.

[157] K. N. Gabet and J. A. Sutton. Narrowband versus broadband excitation for CH_2O PLIF imaging in flames using a frequency-tripled Nd:YAG laser. *Experiments in Fluids*, 55, 2014.

[158] A. Ehn, O. Johansson, J. Bood, A. Arvidsson, B. Li, and M. Alden. Fluorescence lifetime imaging in a flame. *Proceedings of the Combustion Institute*, 33:807–813, 2011.

[159] C. Brackmann, J. Bood, and M. Alden. Quantitative measurements of species and temperature in a DME-air counterflow diffusion flame using laser diagnostic methods. *Combustion Science and Technology*, 178:1165–1184, 2006.

[160] M. de Joannon, A. Ciajolo, R. Ragucci, A. Tregrossi, and A. Cavaliere. Spectroscopic behavior of oxygenated combustion by-products. *Chemosphere*, 51:1071–1077, 2003.

[161] P. R. Medwell, P. A. M. Kalt, and B. B. Dally. Simultaneous imaging of OH, formaldehyde, and temperature of turbulent nonpremixed jet flames in a heated and diluted coflow. *Combustion and Flame*, 148:48–61, 2007.

[162] C. B. Reuter, S. H. Won, and Y. Ju. Flame structure and ignition limit of partially premixed cool flames in a counterflow burner. *Proceedings of the Combustion Institute*, 36, 2017.

[163] C. B. Reuter, S. H. Won, and Y. Ju. Experimental study of the dynamics and structure of self-sustaining premixed cool flames using a counterflow burner. *Combustion and Flame*, 166, 2016.

[164] W. Weng, E. Nilsson, A. Ehn, J. Zhu, Y. Zhou, Z. Wang, Z. Li, M. Alden, and K. Cen. Investigation of formaldehyde enhancement by ozone addition in CH_4/air premixed flames. *Combustion and Flame*, 2014.

[165] S. Wang, D. F. Davidson, and R. K. Hanson. High-temperature laser absorption diagnostics for CH_2O and CH_3CHO and their application to shock tube kinetic studies. *Combustion and Flame*, 160:1930–1938, 2013.

[166] G. Friedrichs, D. F. Davidson, and R. K. Hanson. Validation of a Thermal Decomposition Mechanism of Formaldehyde by Detection oh CH_2O and HCO Behind Shock Waves. *International Journal of Chemical Kinetics*, 2004.

[167] H. Bladh, C. Brackmann, P. Dahlander, I. Denbratt, and P.-E Bengtsson. Flame propagation visualization in a spark-ignition engine using laser-induced fluorescence of cool-flame species. *Measurement Science and Technology*, 16:1083–1091, 2005.

[168] C. Brackmann, Z. Li, M. Rupinski, N. Docquier, G. Pengloan, and M. Alden. Strategies for Formaldehyde Detection in Flames and Engines Using a Single-Mode Nd:YAG/OPO Laser System. *Applied Spectroscopy*, 59(6), 2005.

[169] R. Schiessl, P. Pixner, A. Dreizler, and U. Maas. Formaldehyde formation in the endgas of Otto engines: Numerical simulations and quantitative concentration measurements. *Combustion Science and Technology*, 149:339–360, 1999.

[170] M. de Joannon, R. Ragucci, A. Cavaliere, and A. Ciajolo. Identification of oxygenated compounds in combustion systems. *Chemosphere*, 42:843–851, 2001.

[171] G. Bruneaux. Combustion structure of free and wall-impinging diesel jets by simultaneous laser-induced fluorescence of formaldehyde, poly-aromatic hydrocarbons, and hydroxides. *International Journal of Engine Research*, 9, 2008.

[172] R. Collin, J. Nygren, M. Richter, M. Alden, L. Hildingsson, and B. Johansson. Simultaneous OH- and Formaldehyde-LIF Measurements in an HCCI Engine. *SAE Transactions, Journal of Fuels and Lubricants*, 112:2479–2486, 2003.

[173] M. Richter, R. Collin, J. Nygren, M. Alden, L. Hildingsson, and B. Johnasson. Studies of the Combustion Process with Simultaneous Formaldehyde and OH PLIF in a Direct-Injected HCCI Engine. *JSME International Journal*, 48(4), 2005.

[174] G. Särner, M. Richter, M. Alden, L. Hildingsson, A. Hultqvist, and B. Johansson. Simultaneous PLIF Measurements for Visualization of Formaldehyde- and Fuel- Distributions in a DI HCCI Engine. *SAE Technical Papers 2005-01-3869*, 2005.

[175] A. J. Donkerbroek, A. P. van Vliet, L. M. T. Somers, P. J. M. Frijters, R. J. H. Klein-Douwel, N. J. Dam, W. L. Meerts, and J. J. ter Meulen. Time- and space-resolved quantitative LIF measurements of formaldehyde in a heavy-duty diesel engine. *Combustion and Flame*, 157:155–166, 2010.

[176] A. G. Novoselov, C. B. Reuter, O. R. Yehia, S. H. Won, M. K. Fu, K. Kokmanian, M. Hultmark, Y. Ju, and M. E. Mueller. Turbulent nonpremixed cool flames: Experimental measurements, Direct Numerical Simulation, and manifold-based combustion modeling. *Combustion and Flame*, 209:144–154, 2019.

[177] S. A. Skeen, J. Manin, and L. M. Pickett. Simultaneous formaldehyde PLIF and high-speed schlieren imaging for ignition visualization in high-pressure spray flames. *Proceedings of the Combustion Institute*, 35:3167–3174, 2015.

[178] T. Shimizu, H. Nakamura, T. Tezuka, S. Hasegawa, and K. Maruta. OH- and CH_2O-LIF measurements for hydrogen flames and methane, n-butane and dimethyl ether weak flames in a micro flow reactor with a controlled temperature profile. *Energy and Fuels*, 2017.

[179] N. Zobel and A. Anca-Couce. Slow pyrolysis of wood particles: Characterization of volatiles by Laser-Induced Fluorescence. *Proceedings of the Combustion Institute*, 34:2355–2362, 2013.

[180] C. Brackmann, M. Alden, P.-E. Bengtsson, K. O. Davidsson, and J. B. C. Pettersson. Optical and Mass Spectrometric Study of the Pyrolysis Gas of Wood Particles. *Applied Spectroscopy*, 57(2), 2003.

[181] M. J. Prins, Z. S. Li, R. J. M. Bastiaans, J. A. van Oijen, M. Alden, and L. P. H. de Goey. Biomass pyrolysis in a heated-grid reactor: Visualization of carbon monoxide and formaldehyde using Laser-Induced Fluorescence. *Journal of Analytical and Applied Pyrolysis*, 92:280–286, 2011.

[182] A. Fayoux, K. Zähringer, O. Gicquel, and J. C. Rolon. Experimental and numerical determination of heat release in counterflow premixed laminar flames. *Proceedings of the Combustion Institute*, 30:251–257, 2005.

[183] R. Yuan, J. Kariuki, A. Dowlut, R. Balachandran, and E. Mastorakos. Reaction zone visualisation in swirling spray n-heptane flames. *Proceedings of the Combustion Institute*, 35:1649–1656, 2015.

[184] I. A. Mulla, A. Dowlut, T. Hussain, Z. M. Nikolaou, S. R. Chakravarthy, N. Swaminathan, and R. Balachandran. Heat release rate estimation in laminar premixed flames using laser-induced fluorescence of CH_2O and H-atom. *Combustion and Flame*, 165:373–383, 2016.

[185] T.M. Dyer. Rayleigh scattering measurements of time-resolved concentration in a turbulent propane jet. *AIAA*, 17, 1979.

[186] M. C. Escoda and M. B. Long. Rayleigh scattering measurements of the gas concentration field in turbulent jets. *AIAA*, 21, 1983.

[187] R. W. Dibble and R. E. Hollenbach. Laser Rayleigh thermometry in turbulent flames. *18th Symp. (Int.) on Combustion (Combustion Institute)*, 1981.

[188] B. R. Miles and W. R. Lempert. Quantitative flow visualization in unseeded flows. *Annu. Rev. Fluid. Mech.*, 29:285–326, 1997.

[189] H. Shimizu, S. A. Lee, and C. Y. She. High spectral resolution lidar system with atomic blocking filters for measuring atmospheric parameters. *Appl. Opt.*, 22, 1983.

[190] P. Desgroux, L. Gasnot, and L. R. Sochet. Instantaneous temperature measurement in a rapid-compression machine using laser Rayleigh scattering. *Applied Physics B*, 61:69–72, 1995.

[191] F. Fuest, R. S. Barlow, J.-Y. Chen, and A. Dreizler. Raman/Rayleigh scattering and CO-LIF measurements in laminar and turbulent jet flames of dimethyl ether. *Combustion and Flame*, 159:2533–2562, 2012.

[192] R. L. Gordon, A. R. Masri, and E. Mastorakos. Simultaneous Rayleigh temperature, OH- and CH_2O-LIF imaging of methane jets in a vitiated coflow. *Combustion and Flame*, 155:181–195, 2008.

[193] F. T. C. Yuen and Ö. L. Gülder. Premixed turbulent flame front structure investigation by Rayleigh scattering in the thin reaction zone regime. *Proceedings of the Combustion Institute*, 32:1747–1754, 2009.

[194] H. Schwarz, L. Zimmer, D. Durox, and S. Candel. Detailed measurements of equivalence ratio modulations in premixed flames using laser Rayleigh scattering and absorption spectroscopy. *Experiments*, 49:809–821, 2010.

[195] C. Espey, J. E. Dec, T. A. Litzinger, and D. A. Santavicca. Planar Laser Rayleigh Scattering for Quantitative Vapor-Fuel Imaging in a Diesel Jet. *Combustion and Flame*, 109:65–86, 1997.

[196] D. Ityaksov, H. Linnartz, and W. Ubachs. Deep-UV Rayleigh Scattering of N_2, CH_4 and SF_6. *Molecular Physics*, 106:2471–2479, 2008.

[197] S.-H. Jin and G.-S. Kim. Simultaneous measurements of burning velocity and temperature distribution of combustion using UV laser Rayleigh scattering. *Measurement*, 169:177–184, 2021.

[198] W. R. Lempert, P.-F. Wu, and R. B. Miles. Filtered Rayleigh scattering measurements using a MHz rate pulse-burst laser. *35th Aerospace Sciences Meeting and Exhibit*, 1997.

[199] D. Müller, R. Pagel, A. Burkert, V. Wagner, and W. Paa. Two-dimensional temperature measurements in particle loaded technical flames by filtered Rayleigh scattering. *Applied Optics*, 53(9), 2014.

[200] G. S. Elliott, N. Glumac, and C. D. Carter. Molecular filtered Rayleigh scattering applied to combustion. *Measurement Science and Technology*, 12:452–466, 2001.

[201] A. P. Yalin and R. B. Miles. Temperature Measurements by Ultraviolet Filtered Rayleigh Scattering Using a Mercury Filter. *Journal of Thermophysics and Heat Transfer*, 14(2), 2000.

[202] A. P. Yalin, Y. Z. Ionikh, and R. B. Miles. Gas temperature measurements in weakly ionized glow discharges with filtered Rayleigh scattering. *Applied Optics*, 41(18):3753–3762, 2002.

[203] M. Sneep and W. Ubachs. Direct measurement of the Rayleigh scattering cross section in various gases. *Journal of Quantitative Spectroscopy and Radiative Transfer*, 92:293–310, 2005.

[204] U. Hohm and K. Kerl. Temperature dependence of mean molecular polarizability of gas molecules. *Molecular Physics*, 58:541–550, 1986.

[205] R. D. Sharma. Contribution of the polarizability anisotropy to Rayleigh scattering. *Journal of Geophysical Research*, 112, 2007.

[206] M. P. Bogaard, A. D. Buckingham, R. K. Pierens, and A. H. White. Rayleigh Scattering Depolarization Ratio and Molecular Polarizability Anisotropy for Gases. *Journal of the Chemical Society, Faraday Transactions1: Physical Chemistry in Condensed Phases*, 74, 1978.

[207] C. G. Fotache, T. G. Kreutz, D. L. Zhu, and C. K. Law. An Experimental Study of Ignition in Nonpremixed Counterflowing Hydrogen versus Heated Air. *Combustion Science and Technology*, 109:373–393, 1995.

[208] C. B. Oh, A. Hamins, M. Bundy, and J. Park. The two-dimensional structure of low strain rate counterflow nonpremixed-methane flames in normal and microgravity. *Combustion Theory and Modelling*, 12:283–302, 2008.

[209] C. Breck Hitz, J. Ewing, and J. Hecht, editors. *Introduction to Laser Technology*. John Wiley and Sons, Inc., 4 edition, 2012.

[210] D. C. Dumitras, editor. *Nd YAG Laser*. InTech, 2012.

[211] K. Thyagarajan and A. Ghatak, editors. *Lasers: Fundamentals and Applications*. Springer, 2 edition, 2010.

[212] O. Svelto and D. C. Hanna, editors. *Principles of Lasers*. Springer Science and Business Media, LLC, 4 edition, 1998.

[213] F. Durst, A. Melling, and J. H. Whitelaw. *Theorie und Praxis der Laser-Doppler-Anemometrie*. Braun-Verlag, 1987.

[214] D. A. Skoog, F. J. Holler, and S. R. Crouch. *Instrumentelle Analytik: Grundlagen - Geräte - Anwendungen*. Springer Spektrum, 6 edition, 2013.

[215] W. Zinth and U. Zinth. *Optik: Lichstrahlen - Wellen - Photonen*. De Gruyter, 2018.

[216] LaVision GmbH. Website: www.lavision.de; last accessed: 25.07.2021. 2021.

[217] V. Van Nieuwenhove, J. De Beenhouwer, F. De Carlo, L. Mancini, F. Marone, and J. Sijbers. Dynamic intensity normalization using eigen flat fields in X-ray imaging. *Optics Express*, 23:27975–27989, 2015.

[218] S. B. Howell. *Handbook of CCD Astronomy*. Cambridge University Press, 2 edition, 2006.

[219] J. A. M. Withag, J. B. W. Kok, and K. Syed. Transient Combustion Modeling of an Oscilating Lean Premixed Methane/Air Flame. *Proceedings of the ASME Turbo Expo*, 2008.

[220] F. Behrendt. *Simulation laminarer Gegenstromdiffusionsflammen unter Verwendung detaillierter Reaktionsmechanismen*. PhD thesis, Ruprecht-Karls-Universität Heidelberg, 1989.

[221] V. Cuervo Pinera. Numerical Investigation of Laminar One-Dimensional Counter-Flow Flames from Product Gas of Woody Biomass Pyrolisis and Gasification. Master's thesis, Technische Universität Berlin, 2015.

[222] I. Glassman, R. A. Yetter, and N. G. Glumac, editors. *Combustion*. Academic Press, 5 edition, 2015.

[223] R. Byron Bird, W. E. Stewart, and E. N. Lightfoot, editors. *Transport Phenomena*. John Wiley and Sons, Inc., 2 edition, 2002.

[224] V. Sick, A. Arnold, E. Dießel, T. Dreier, W. Ketterle, B. Lange, J. Wolfrum, K. U. Thiele, F. Behrendt, and J. Warnatz. Two-Dimensional Laser Diagnostics and Modeling of Counterflow Diffusion Flames. *Symposium (International) on Combustion*, 23:495–501, 1990.

[225] I. Glassman. Sooting laminar diffusion flames: Effect of dilution, additives, pressure, and microgravity. *Symposium (International) on Combustion*, 27:1589–1596, 1998.

[226] F. Liu, A. E. Karatas, Ö. L. Gülder, and M. Gu. Numerical and experimental study of the influence of CO_2 and N_2 dilution on soot formation in laminar coflow C_2H_4/air diffusion flames at pressures between 5 and 20 atm. *Combustion and Flame*, 162:2231–2247, 2015.

[227] R. G. W. Norrish. A Theory of the Combustion of Hydrocarbons. *Proceedings of the Royal Society of London*, 150:36–57, 1935.

[228] W. Zhang, H. Liu, I. U. Hai, Y. Neubauer, P. Schröder, H. Oldenburg, A. Seilkopf, and A. Kölling. Gas cleaning strategies for biomass gasification product gas. *International Journal of Low-Carbon Technologies*, 7:69–74, 2012.

[229] M. Asadullah. Biomass gasification gas cleaning for downstream applications: A comparative critical review. *Renewable and Sustainable Energy Reviews*, 40:118–132, 2014.